FLORIDA STATE UNIVERSITY

COLLEGE OF ARTS AND SCIENCES

EXPLORING THE NUCLEAR STRUCTURE OF THE A = 39 ISOBARS

By

BRITTANY LYNN ABROMEIT

A Dissertation submitted to the
Department of Physics
in partial fulfillment of the
requirements for the degree of
Doctor of Philosophy

2018

Brittany Lynn Abromeit defended this dissertation on November 13, 2018.
The members of the supervisory committee were:

Samuel Tabor
Professor Directing Dissertation

Munir Humayun
University Representative

Eric Hsiao
Committee Member

Mark Riley
Committee Member

Alexander Volya
Committee Member

The Graduate School has verified and approved the above-named committee members, and certifies that the dissertation has been approved in accordance with university requirements.

To the moon and stars: always guiding me when my compass is pointing the wrong way, always grounding me when my feet begin to float, always reminding me that anything is possible if you just try.

ACKNOWLEDGMENTS

This glorious day, the day in which my career as a student finally ends, is bittersweet. I cannot entirely say that I am ecstatic to be complete without admitting to being a touch sad to see it end. These long years have been some of the worst and best times of my life and I honestly would not be here today if it were not for all the amazing people in my life.

To my Nuclear Family: Thank you for being such amazing teachers and guides, always challenging me to be the best scientist I can be. Sean, thank you for getting me started on the path of nuclear physics, supplying endless tissues when I came into your office with the many nervous breakdowns and, most importantly, for introducing me to Sam. Sam, thank you for all the stories and knowledge of pretty much everything: your wisdom and experiences will be the source of many adventures I will take one day, both traveling the World and in my career as a Nuclear Physicist. Vandana, thank you for being our mom when all of our moms are so far away and for always encouraging us to explore new ways of doing something.

To my friends and loved ones: you all have shown such great kindness and strength when I needed it. We have laughed together, we have cried together. You all watched as I struggled to come into my own, from the changing hobbies to the changing hair color. Thank you for always being there to shine bright regardless of the wild Tallahassee weather.

To Betty: you came into my life and filled a hole. You brought love and comfort when I needed it the most... Plus, you are the best of both worlds (even though you literally chew on everything and are the reason we can't have nice things).

To my big, little sister, Amber: You are literally my reason for being here on this Earth. You inspire me to be the best person I can be so that you have someone to look up to. Without you, I would not have the courage to have crazy hair, makeup, or be me! Thank you for always pushing me to be the best version of me, whether you know it or not.

To my dad, Eric: Without you convincing my mom to let me go to Michigan State for school, I most certainly would not be where I am today. You gave me the World and allowed for me to explore it while keeping my mom from torturing my teddy bear to keep me in Colorado. You called us your own and loved us as such. From the many mental breakdowns while sitting on our "custom" bar stools at BDubs to the very long phone calls once in a blue moon, I cannot say without lying that you were not one of the most contributing factors that helped keep my head above water during this long journey.

To my mom, Lynn: Words cannot possibly describe how much this achievement is as much yours as it is mine. You have always pushed me to keep going, to do better. You reminded me that I would be bored doing an “average Joe” job and convinced me to keep going when I was dead-set on giving up. You allowed me to move 1600 billions of miles away, despite the close casualty of the teddy bear, to go accomplish my dreams. You always listened when I would call blabbering about something so incredibly stupid or when I thought for sure this was going to be the time I died from a simple cold. You have taught me how to be successful, how to face the World and say, “You can’t hurt me!”, and then how to get back up when the World sucker punched me in the face. You are always there for me, even during your own darkest hour, you never left me to fend for myself. Most importantly, you showed me what strength looks like, and that as long as we three stick together, we can beat anything this World throws at us. I would be lying if I said I could do this without you, because, let’s face it, a week does not go by without me calling to ask where a certain item is at the grocery store or how to do some remedial thing.

I love every single one of you from the bottom of my heart and have many many thanks to give!

P.s Yes, I did acknowledge my cat... but if you ever met Betty, you know she is the jelly to my peanut butter! And if you have not met her, I’m truly sorry... You are missing out!

TABLE OF CONTENTS

LIST OF TABLES

LIST OF FIGURES

ABSTRACT

Investigation of nuclei with neutron and proton imbalance is at the forefront of nuclear physics research today, along with how the nuclear structure varies with the movement of the nucleons. Experimental data and theoretical models work hand-in-hand to understand the structure of these nuclei. Two of the A = 39 isobars, residing in limbo between the sd- and fp-shells are the isotopes of interest for this study. With 24 neutrons, eight neutrons more than the stable isotope of phosphorous, ^{39}P is considered a neutron-rich exotic nucleus, one of which has not been extensively studied until now. Since the late 1990s only two experiments have been conducted, producing the three known gamma-rays and one tentative gamma-ray for ^{39}P. Except for half-life measurements and mass measurements, no further studies of ^{39}P have been done prior to a beta-gamma coincidence experiment conducted in this study at the National Superconducting Cyclotron Laboratory (NSCL) using the Beta Counting System. Continuing up the isobaric chain from ^{39}P toward stability, ^{39}Ar is reached. Unlike ^{39}P, ^{39}Ar is nested between two of the stable isotopes of argon. Being closer to stability, it has been studied more extensively using transfer reactions, however, limited information on high-spin states is produced from only two prior experiments. Despite the more extensive study of ^{39}Ar, the observed gamma transitions are only well known for low-spin states except for one band of high-spin states which have been studied heavily using the gamma spectroscopy setup at the John D. Fox Superconducting Linear Accelerator Laboratory at Florida State University. Results for both isotopes, along with comparisons to Shell Model calculations will be presented.

CHAPTER 1

INTRODUCTION

In the late 19th century, scientists started to dig deep into the heart of Matter. From the first discovery of radioactivity to observing the neutron-star mergers, nuclear physics has been a topic of interest for quite some time. With the advancement of technology, more regions of the Chart of Nuclei that were once untouchable can now be studied. The goal now is to understand the structure of atomic nuclei as fully as possible.

New methods of experimentation and calculations are being developed by experimentalist and theorist working together, both striving to provide the much needed information that each other require. The building of new accelerators and supercomputers only further boosts the ability to create and study isotopes of nuclei that were not previously obtainable.

Through an extensive study of both stable and unstable nuclei, the much needed data can be collected, complied, and used to form theoretical models that allow accurate predictions for both isotopes near and far from stability. As it stands, there are a number of theoretical models that are used today: the Shell Model, for example, uses the microscopic configuration of nucleons to predict the structure of nuclei [8]. Within the Shell Model, there are different types of interactions that can be used to model the various regions of the Chart of Nuclei, such as USD[A,B] for sd-shell nuclei and WBP for sp-,sd-, and fp-shell nuclei [9]. Although these interaction models are quite good at representing nuclei close to stability in the appropriate proton and neutron shells, as the balance of protons to neutrons decreases, the ability of the models to predict the characteristics of the isotopes also decreases. For this reason, it is pertinent to thoroughly understand the nuclei that are close to stability as much as those further from stability. It is because of this that the two isobar nuclei, ^{39}Ar and ^{39}P, were chosen to be studied and analyzed for this project.

1.1 The Basics: Shell Model

Before diving deep into the discussion of the A = 39 isobars, a basic understanding of the Shell Model will be useful. As mentioned in the previous section, the Shell Model is only one theoretical model that is used in nuclear physics to characterize and predict properties of nuclei. The fundamental idea of the Shell Model is that each nucleon moves within the nucleus and is governed by a potential that is generated by other nucleons [10]. This gives the idea, similar to atomic physics, that the nucleons reside within shells. Figure 1.1 shows a general schematic of the first four lowest shells groupings in the Shell Model. Protons and neutrons are treated separately, and thus, have their own set of shells to occupy.

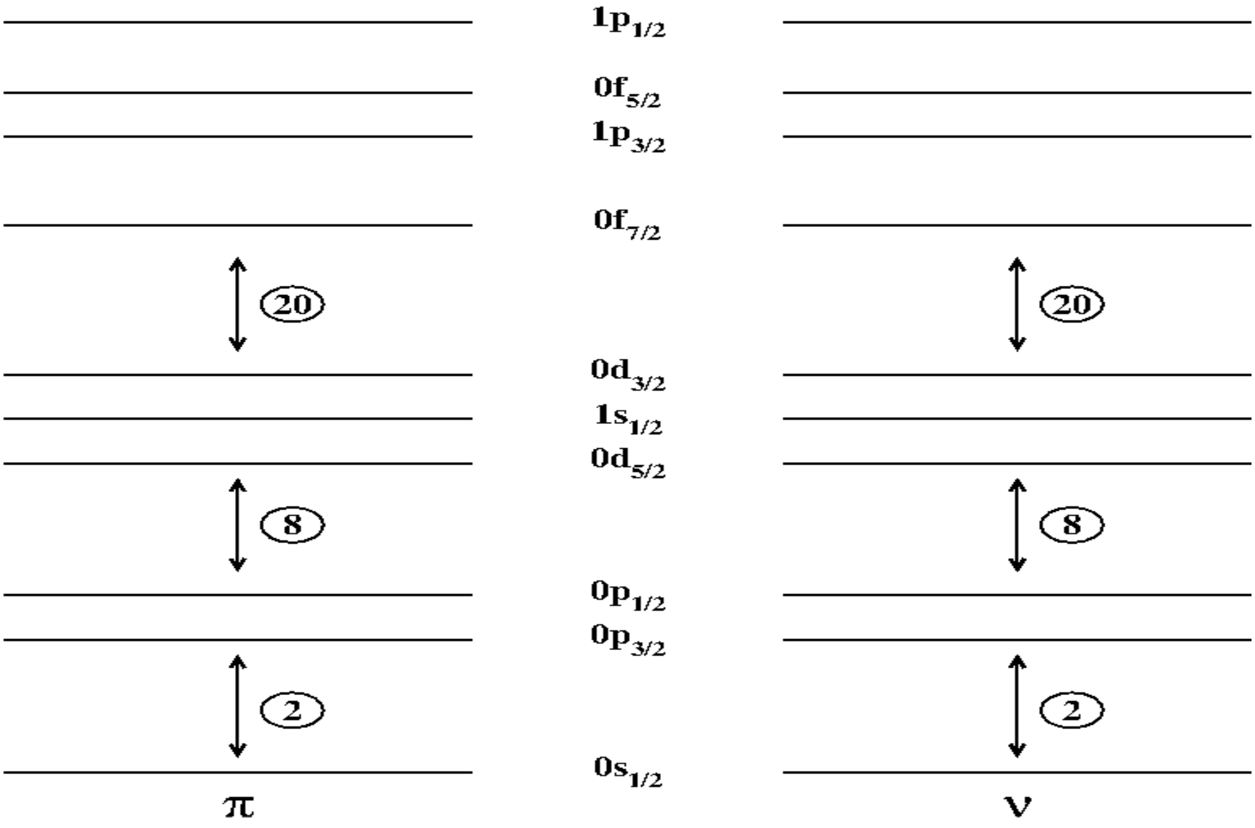

Figure 1.1: Schematic of the first four shell groups in the Shell Model. The proton shells are labeled as π, where as the neutron shells are labeled with ν. Shell gaps, corresponding to magic numbers, are also labeled.

As nucleons are added by increasing protons, Z, and neutrons, N, they fill the appropriate shells. This takes some organization in order to satisfy the Pauli Exclusion principle along with available occupancies for each individual shell. The maximum occupancy of a particular shell is given by $(2j+1)$ where j is the angular momentum of the shell. For example, $0d_{5/2}$: the maximum occupancy for this particular shell is six, since $j = 5/2$. The parity of the shell is also rather easy to determine using $(-1)^l$, with l being 0, 1, 2, 3, ... for s, d, p, f, and so forth. The spin-parity, J^π, of the created excited state can be deduced through nucleon interactions. The J^π of the ground state of an odd A will be determined by the shell that the unpaired nucleon is sitting in. Even-Even nuclei, meaning both Z and N are even, have a ground state with $J^\pi = 0^+$, due to the fact that all the protons and neutrons pair off separately to J = 0. The ground state of ^{39}Ar, in contrast, has $J^\pi = 7/2^-$ due to the unpaired neutron sitting in the $0f_{7/2}$ shell (see Figure 1.2).

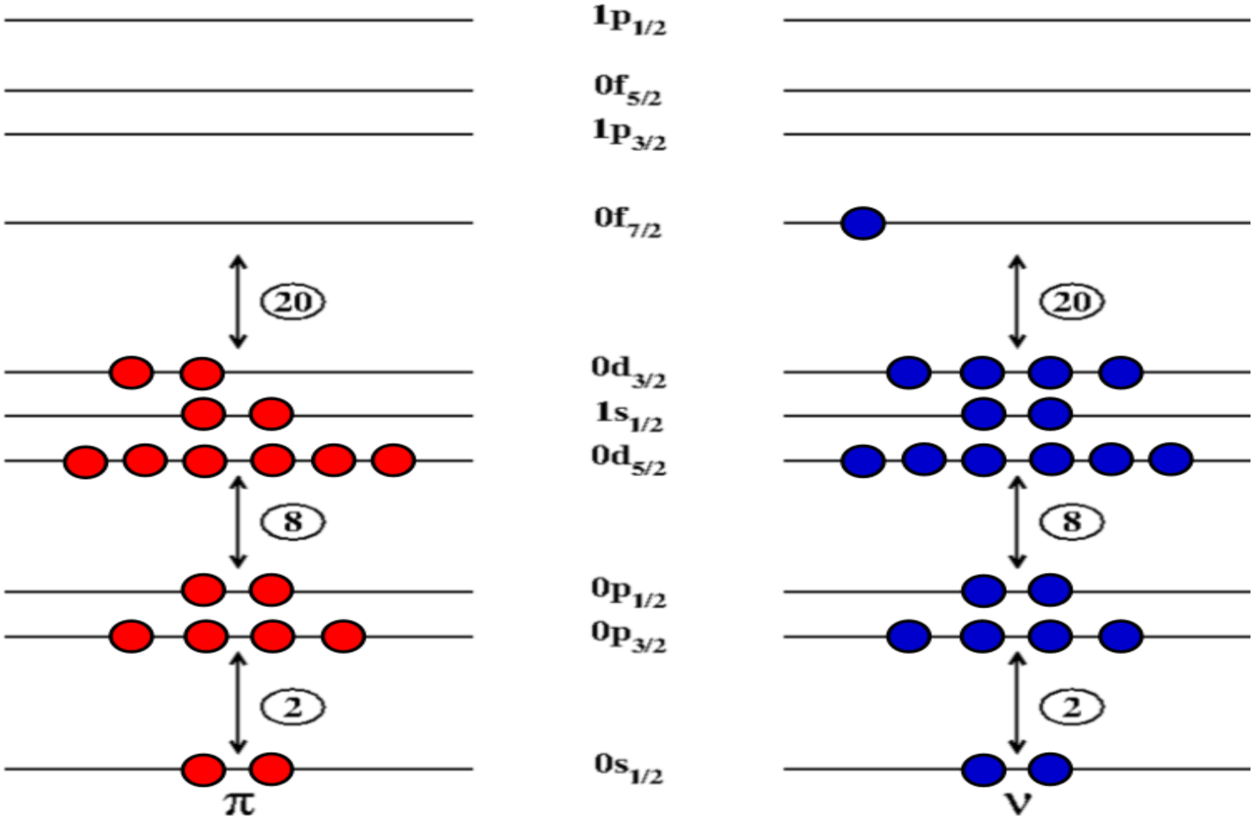

Figure 1.2: Schematic of the shell structure for ^{39}Ar, Z = 18 and N = 21. The proton shells are labeled as π, where as the neutron shells are labeled with ν

This way of determining J^π for the ground state of a nucleus is also the same way the J^π of an excited state can be determined. There are two options of obtaining an excited state with a new J^π: either through the recoupling of already paired nucleons, or the promotion of one or more nucleons to other orbitals. Keeping in mind that both neutrons and protons must follow the Pauli Exclusion principle, each nucleon within an individual orbital must occupy a different magnetic substate. ^{17}O is an excellent isotope to demonstrate how the pairing and moving of nucleons determine the energy and J^{π} of excited states. Figure 1.3a shows ^{17}O in the ground-state configuration. With Z = 8 and N = 9, there is one unpaired neutron in the $0d_{5/2}$ orbital, making the ground state have a $J^{\pi} = 5/2^{+}$. If the $d_{5/2}$ neutron is promoted to the $1s_{1/2}$ orbital then an excited state will be created with a maximum $J^{\pi} = 1/2^{+}$

In addition to the individual shells, shell groupings play a crucial role on the structure of nuclei (as will be shown in Chapter 3). These groups were mentioned briefly above, when discussing the interactions that are used to model the different regions of the nucleus. In Figure 1.1, it is easy to see the clumping of the individual orbitals to build a group of shells. Shown in Figures 1.1, 1.2, 1.3a, and 1.3b are the s-, p-, sd-, and fp-shells. Notice the numbers that are circled between each group of shells: these numbers are called "magic numbers" and indicate the closure of a major shell. The magic numbers are generally when a certain behavior of the nucleons becomes apparent or discontinues [10] and can be rather important when it comes to fitting a particular interaction model to observed data. The observed data can come from the promotion of nucleons across the shell gaps. As an example, again, take ^{17}O: instead of only promoting the solitary neutron in the sd-shell, one of the protons from the $0p_{1/2}$ orbital can be promoted across the Z = 8 shell gap and into the $0d_{5/2}$ orbital, as shown in Figure 1.3b. In this case the maximum spin would be calculated by the two nucleons sitting in the $0d_{5/2}$ orbital, along with the "hole" remaining in the $0p_{1/2}$ orbital. Maximum J is calculated as follows: $0d_{5/2}$ proton = 5/2, $0d_{5/2}$ neutron = 5/2, $0p_{1/2}$ hole = 1/2 → $J = \nu 5/2^{+} \bigotimes \pi 5/2^{+} \bigotimes \pi 1/2^{-} = 11/2^{-}$. The parity, π, is then $(+1) \times (+1) \times (-1)$ or $(-1)^{l=1}$ since the "hole" is in the $0p_{1/2}$ orbital and $l = 1$ for p shells. Although the maximum $J^{\pi} = 11/2^{-}$, the state can have a spin ranging from 11/2 to1/2 because each nucleon in the $0d_{5/2}$ orbital can have a magnetic substate ranging from $\pm 5/2, \pm 3/2, \pm 1/2$ and the "hole" in the $0p_{1/2}$ can have magnetic substates $\pm 1/2$.

Most interactions, as previously mentioned, fit observed data quite well for nuclei with nucleons in certain regions. The interactions begin to fail, however, when it comes to nuclei that have cross-shell interactions. Cross-shell interactions, or intruder states, are created when nucleons are promoted across a shell gap. Studying these intruder states are crucial to developing and improving existing Shell Model interactions and are one of the main reason for studying nuclei and their structure as the number of neutrons is increased.

1.2 Structural Evolution of ^{39}Ar

^{39}Ar is nestled between two stable isotopes of argon and has 18 protons and 21 neutrons, placing it in limbo between the sd- and fp-shells. Studies on ^{39}Ar began as early as 1961 and were continuous until the mid 1980s. Only one other study was conducted in the 21st century. The majority of experiments conducted were particle-transfer reactions, with the exception of five experiments (one being a beta decay, the other four being fusion-evaporation type experiments).

In 1961, Bass *et al.* conducted the first experiment that produced ^{39}Ar and did so using a neutron beam with energies ranging from 3.8-8.7 MeV impinged on a KI(TI) scintillation crystal that acted as both a target and charged-particle detector. The experiment was conducted using the 5.5 MeV electrostatic accelerator from Rice University [11]. Three years later, Bass *et al.* conducted a similar experiment, ^{39}K(n,p), with a KI(TI) crystal for a target, at the Frankfurt 5.5 MeV Van de Graaff accelerator in Germany [12]. 15 energy levels were reported, four of which had accompanying J^{π} assignments. The cross sections for the four excited states with associated J^{π} were also reported [11, 12]. Another two years later, Bass *et al.* proceeded to conduct two more experiments at the Frankfurt Van de Graaff accelerator with a KI(TI) scintillation crystal and neutron beams with energies of 4.8-, 5.4-, and 7.0 MeV. Accompanying the two newer experiments were a five-sided Ge(Li) detector [13] and a Na(TI) crystal scintillator [14], allowing for the first set of gamma-ray (γ) transitions to be observed. Approximately 70 γ transitions were reported [13, 14].

While Ref. [11, 12, 13, 14] were producing ^{39}Ar through the transfer of a neutron, Johnson and Griffiths were busy populating ^{39}Ar by charge exchange via a ^{40}Ar(p,n) reaction. In 1968, Johnson and Griffiths produced a proton beam with an energy of 27.5 MeV at the University of Colorado Nuclear Physics Laboratory 1.3-m FFAG cyclotron. Using a natural argon gas target, cross sections and spectroscopic factors were reported for excited states in ^{39}Ar [15]. Tonn *et al.* later conducted a similar transfer reaction at the Michigan State University cyclotron. Again, cross sections, spectroscopic factors, and l-transfer values were reported [16].

The first extensive report of J^{π} values for more than the first four reported in Ref. [11, 12] came about in 1972 with the completion of a ^{38}Ar(d,p) reaction conducted by Sen *et al.* using a 10.064-MeV energy deuteron beam produced using the tandem accelerator at the University of Texas. A gas cell target of isotopically enriched ^{38}Ar was used, along with Si(Li) detectors to detect the reaction products [17]. The (d,p) reaction was able to see three out of the four states reported in Ref. [11, 12], reproducing the J^{π} values, and was able to deduce seven new J^{π} values from angular distributions using l-transfer values from cross section measurements. The energy level reported at 4255 keV is listed to have a J^{π} of $7/2^{-}$ [17]. This is the first reported definitive J^{π} value, of an excited state, having a spin greater than $J = 3/2$.

While Ref. [11, 12] and Ref. [17] were the first to report J^{π} values, Wiza, Garrett, and Middleton performed a ^{40}Ar(^{3}He,α) experiment using the University of Pennsylvania's tandem accelerator that completed the entirety of previously known excited states in ^{39}Ar. The experiment was conducted using a 16.5 MeV ^{3}He beam and a natural argon gas target [18]. Prior to this experiment, the highest known energy level was 7727 (20) keV reported by Ref. [17]: Wiza *et al.* pushed the envelope and found six new excited states lying above 1 MeV, along with about a dozen other new states above the previously reported highest excited state of 7727 keV.

Following the early 1970's, the known information on ^{39}Ar seemed to be fairly complete except for J^{π} values that accompany the now known excited states. It was not until Warburton *et al.* performed the heavy-ion fusion-evaporation reactions ^{24}Mg(^{18}O, n2pγ), ^{26}Mg(^{18}O,αnγ), and ^{27}Al(^{18}O,np$\alpha\gamma$) that the missing J^{π} values were able to be deduced. The reactions were performed using a 40-MeV ^{18}O beam at the Brookhaven National Laboratory MP tandem Van de Graaff accelerator. With these fusion-evaporation reactions, Warburton *et al.* were able to report the highest J^{π} values known today. $J^{\pi} = (17/2^{+})$ was assigned to the 5535.5 (5) keV excited state and other high-spin states were reported as well [19].

Following Warburton *et al.*, two transfer experiments, ^{37}Cl(α,d), were performed, confirming the findings from Ref. [19]. The experiments were completed by Tonn *et al.* at the Argonne FN Tandem Van de Graaff accelerator [20] and Nann *et al.* at the Michigan State University cyclotron [21]. Ref. [20] used an α beam with an energy of 27 MeV, where Ref. [21] utilized an α beam with an energy of 40 MeV [20, 21]. Both experiments were able to reproduce the high J^{π} values seen in Ref. [19].

A few other transfer reactions were conducted throughout the years, such as ^{40}Ar(d,t) [22], ^{41}K(d,α) [23], ^{40}Ar(pol d,t) [24], and ^{37}Cl(^{3}He,p) [25], confirming the information previously reported. The reactions ^{36}S(α,nγ) and ^{38}Ar(d,pγ) [26] were able to also confirm previously reported information, and more importantly, were able to improve the knowledge of the γ decay scheme in ^{39}Ar. The remaining set of experiments were various other fusion-evaporation reactions and one beta decay. Keinonen *et al.* performed ^{25}Mg(^{16}O,2pγ) and ^{26}Mg(^{18}O,αnγ) using the HVEC tandem accelerator at the University of Koln [27]. Drake *et al.* performed a ^{40}Ca(^{14}C,^{15}O) with a 51-MeV ^{14}C beam at the Los Alamos Van de Graaff accelerator [28]. Shapira *et al.* performed a ^{40}Ar(^{16}O,^{17}O) experiment using a 100-MeV ^{16}O beam at Oak Ridge National Laboratory. Cross sections were measured using a magnetic spectrograph, producing relative yields for five excited states [29]. Wang *et al.* performed the only beta-decay experiment, the beta decay of ^{39}Cl, using a Ge-Na(TI) Compton-suppression spectrometer to detect γ transitions, producing log*ft* values [30].

1.3 Discovering ^{39}P

Moving along the A = 39-isobar chain, ^{39}P has 15 protons and 24 neutrons. Adding eight additional neutrons from the stable isotope of phosphorus, ^{39}P has not been extensively studied until now, due to the large excess of neutrons. Prior to the current work, only three experiments were conducted on the unstable isotope. Ibbotson *et al.* published the first set of data on ^{39}P coming from the coulomb excitation of odd-A neutron-rich isotopes with protons in the sd-shell and neutrons in the fp-shell. The experiment was performed using the K1200 cyclotron at the National Superconducting Cyclotron Laboratory (NSCL) and was able to detect γ transitions using an array of 38 cylindrical NaI(TI) detectors. An excited state at 976 (17) keV was reported [31].

Some time later, an experiment performed at GANIL using a 60.3 MeV/nucleon ^{48}Ca beam impinged on a 2.67 mg/cm^2 ^{9}Be target produced three additional excited states. Conducted by Sorlin *et al.*, the experiment utilized an array of 74 BaF$_2$ scintillators and three segmented Ge clover detectors to detect γ transitions, ultimately establishing new excited states, along with tentative J$^{\pi}$ values [32].

The latest report on ^{39}P comes from Tripathi *et al.* from the beta-decay of ^{38,40}Si [7]. The experiment was conducted at the NSCL and is part of the same data set that will be further explored in this thesis.

1.4 Adding On

Although much is already known about ^{39}Ar, there is much to be explored, specifically building on to Warburton's high-spin states. Further studying ^{39}Ar will only add to the knowledge on the isotope and will significantly improve Shell Model interactions and their ability to reproduce characteristics of other nuclei. Adding knowledge about ^{39}P and surrounding isotopes will also further improve Shell Model interactions in the future and will help fill in the holes that exist prior to the current study.

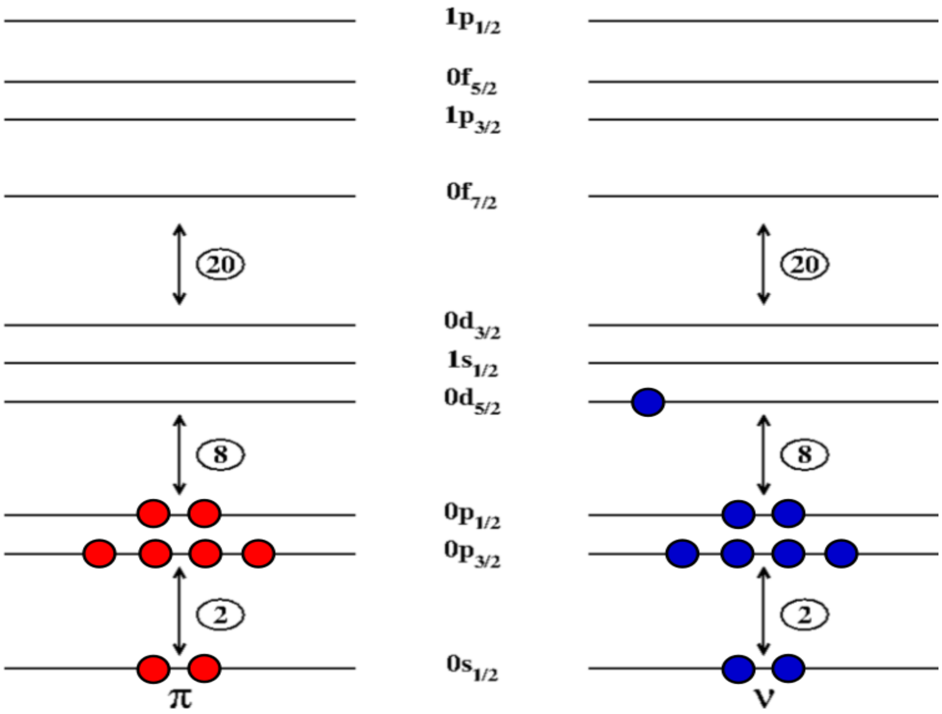

(a) ^{17}O in the ground state configuration.

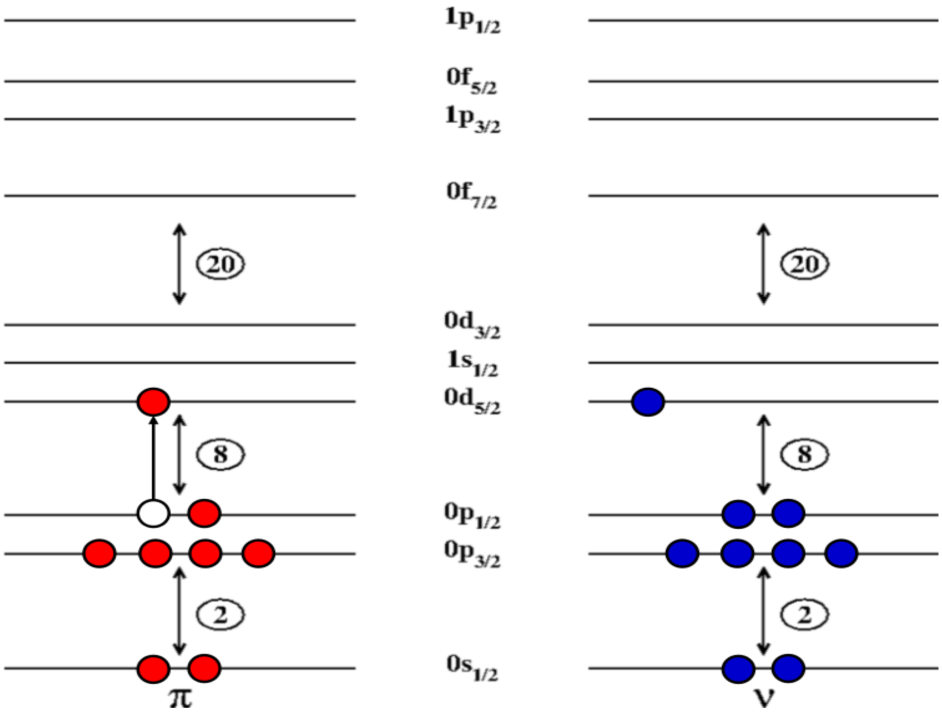

(b) ^{17}O in an intruder state configuration.

Figure 1.3: Schematics of the shell structure for ^{17}O, Z = 8 and N = 9. The proton shells are labeled as π, where as the neutron shells are labeled with ν.

CHAPTER 2

STUDY OF HIGH-SPIN STATES AT JOHN D. FOX SUPERCONDUCTING LINEAR ACCELERATOR LABORATORY

2.1 Fusion-Evaporation Process

In Chapter 1, it was mentioned that one of the main goals of nuclear physics is to understand nuclear structure, particularly in order to improve the interactions used to model nuclei in different regions of the Chart of Nuclei. One such way to study the structure is through the observation of γ transitions. The nuclei must first be created in an excited state in order to emit γ rays, and one way of doing so is through the fusion-evaporation process. Fusion-evaporation is usually done with a heavy projectile impinging on a stationary target, creating a compound nucleus. The excited compound nucleus can then decay through the emission of charged particles or neutrons. Since the reaction has two heavier objects colliding, typically in a non-head-on manner, there is quite a large amount of angular momentum transferred to the compound nucleus. The emission of the charged particles and neutrons will dissipate some of the transferred angular momentum but most of the angular momentum will remain in the nuclei created following particle emission. The excess angular momentum allows for high-spin states to be generated in the nucleus. The high-spin states will then decay primarily through the yrast sequence via the emission of γ rays. The yrast sequence is simply the lowest energy state with a particular J^π value and becomes important in the discussion following the presentation of the experimental results.

Fusion-evaporation reactions are beneficial due to the fact that, with the exception of an (α,d) reaction, they are the only type of reaction that prefers populating high-spin states within a nucleus. The study of high-spin states becomes pertinent when developing and improving Shell Model interactions due to the fact that the high-spin states generally require cross-shell interactions to occur, since it is the highest spin is restricted through the recoupling of nucleons within the same shell. Take, for example, the ground state structure of ^{39}Ar, as can be seen in Figure 1.2. The ground state has a $J^\pi = 7/2^-$ from the unpaired neutron sitting in the $0f_{7/2}$ shell. The highest

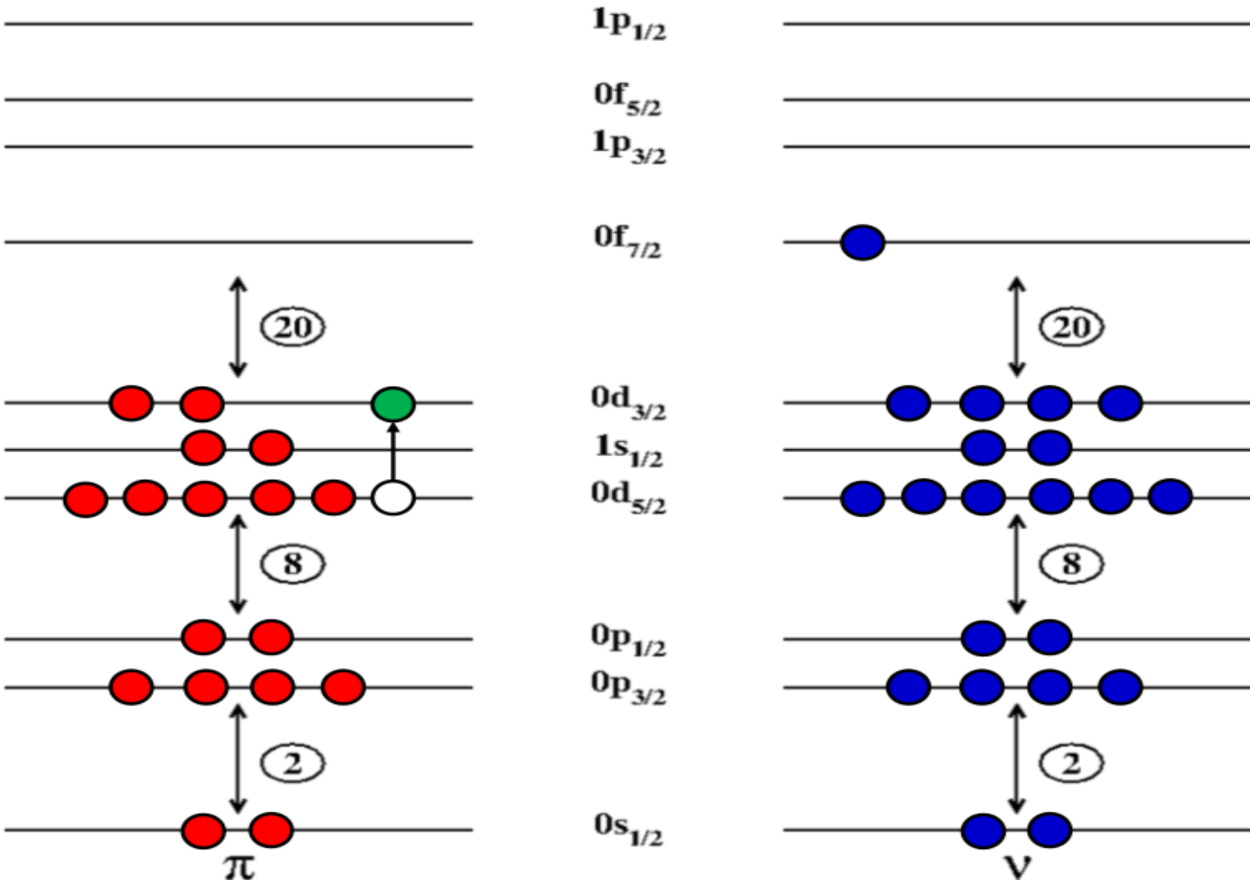

Figure 2.1: Schematic diagram of the $15/2^-$ state in ^{39}Ar. The green dot symbolizes the proton that was moved, leaving a hole in the $0d_{5/2}$ shell. This depicts a 0p-0h state where *zero* nucleons crossed a shell gap relative to the ground-state configuration.

spin possible through the movement of nucleons within their own shell groups is $J^\pi = 15/2^-$. This is done by promoting a proton from the $0d_{5/2}$ orbital to the $0d_{3/2}$ orbital, leaving a "hole" in the $0d_{5/2}$ shell and an unpaired proton in the $0d_{3/2}$ shell. Coupled with the neutron in the $0f_{7/2}$ shell, $J = 7/2 + 5/2 + 3/2 = 15/2$. Since $\pi = (-1)^l$ and $l = 2, 3$ for the d- and f-shell, respectively, the resulting parity is then negative, giving a final $J^\pi = 15/2^-$. If, however, a proton is promoted across the $Z = 20$ gap into the fp-shell, then the J^π can be as high as $23/2^+$, or simply $17/2^+$ if placed in the $0f_{7/2}$ orbital. Figures 2.1 and 2.2 show how the high-spin states are created. Observing these cross-shell interaction adds to the available information that can be used to further develop Shell Model interactions.

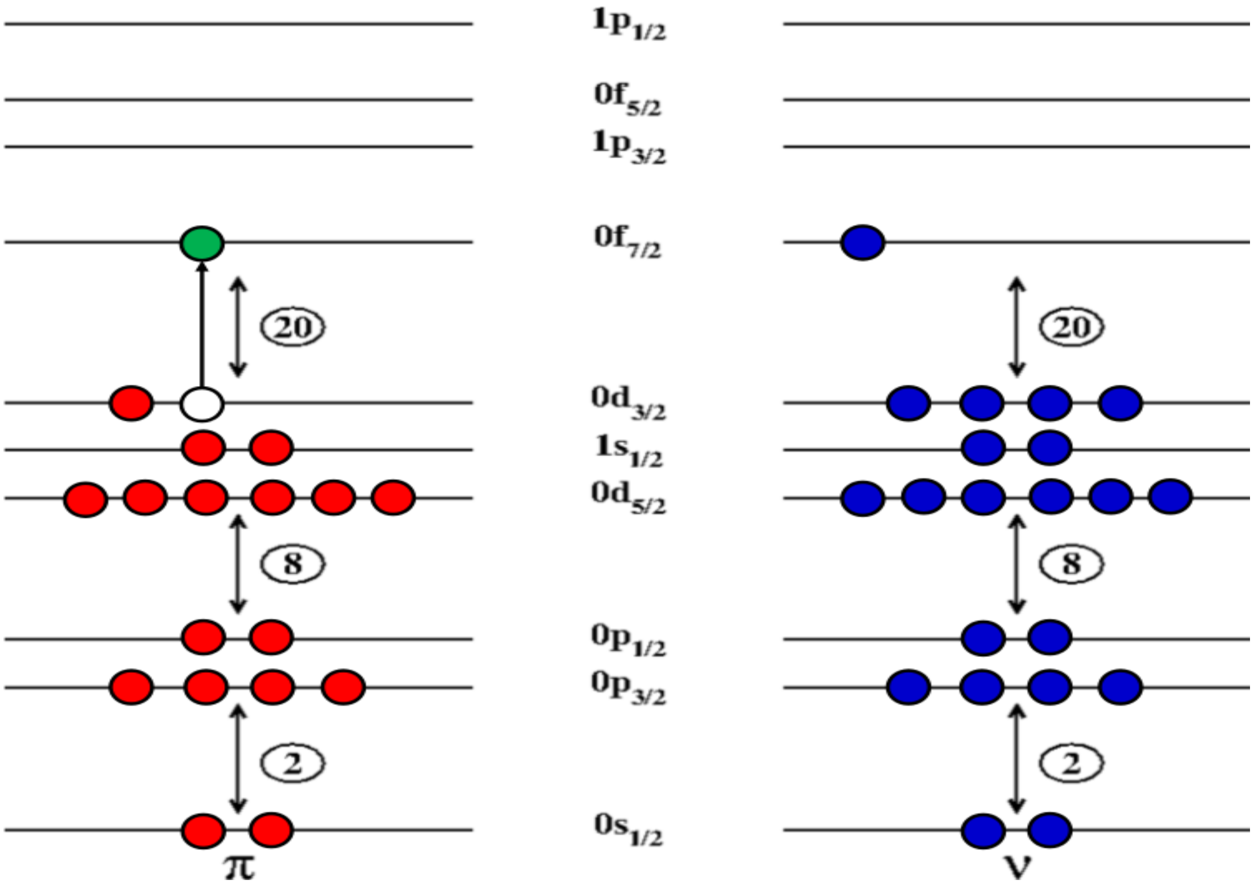

Figure 2.2: Schematic diagram of the $17/2^+$ state in ^{39}Ar. The green dot symbolizes the proton that was moved, leaving a hole in the $0d_{3/2}$ shell. This depicts a 1p-1h state where *one* nucleon crossed a shell gap relative to the ground-state configuration.

2.2 Creating ^{39}Ar: Experimental Details

The number of fusion-evaporation experiments conducted to create ^{39}Ar is significantly smaller than the number of transfer reactions, as mentioned in Chapter 1, providing plenty of room to further explore ^{39}Ar using the fusion-evaporation route. Conducting this type of experiment will also create desired high-spin states that have only been studied in References [19, 20].

To created excited states in ^{39}Ar, a ^{14}C+^{27}Al reaction was performed at the John D. Fox Superconducting Linear Accelerator Laboratory (FOXLAB) at Florida State University (FSU) using the 9-MeV Super-FN tandem Van de Graaff accelerator [4]. The experiment lasted approximately seven days, amounting to approximately 5.9 million proton-γ events, and utilized the FOXLAB

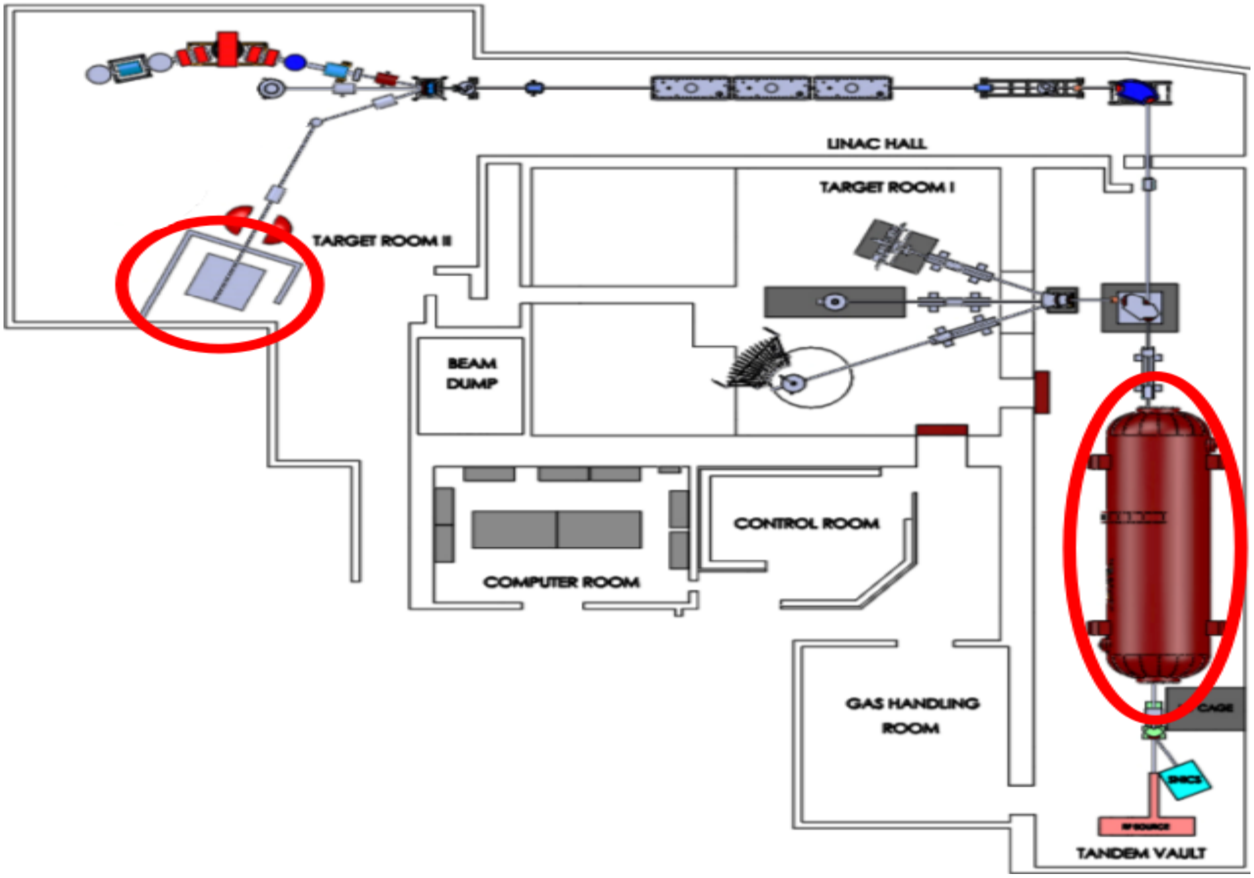

Figure 2.3: Schematic view of the FOXLAB at Florida State University. Highlighted (red circles) are the 9-MeV Super-FN tandem Van de Graaff accelerator and the Gamma Cave, which houses the γ spectroscopy array [4].

ability to create a long-lived radioactive ^{14}C beam with an energy of 25.6 MeV. A beam energy of 25.6 MeV was chosen after thorough examination of predicted cross sections for nuclei that are created via different decay channels from the compound nucleus, ^{41}K. The calculations were conducted using LISE++, a program developed to calculate transmission and yields of fragments produced in reactions [5]. Figure 2.4 show the results. It can be seen that at approximately 26 MeV, the cross section for ^{39}Ar reaches a maximum.

A self-supporting ^{27}Al target of 100 μg/cm^2 thickness was used. A 20 micron thick gold stopping foil was placed after the ^{27}Al target to insure that the beam was completely stopped, while still allowing for light charged particles to pass through. In addition to the thicker ^{27}Al target, a

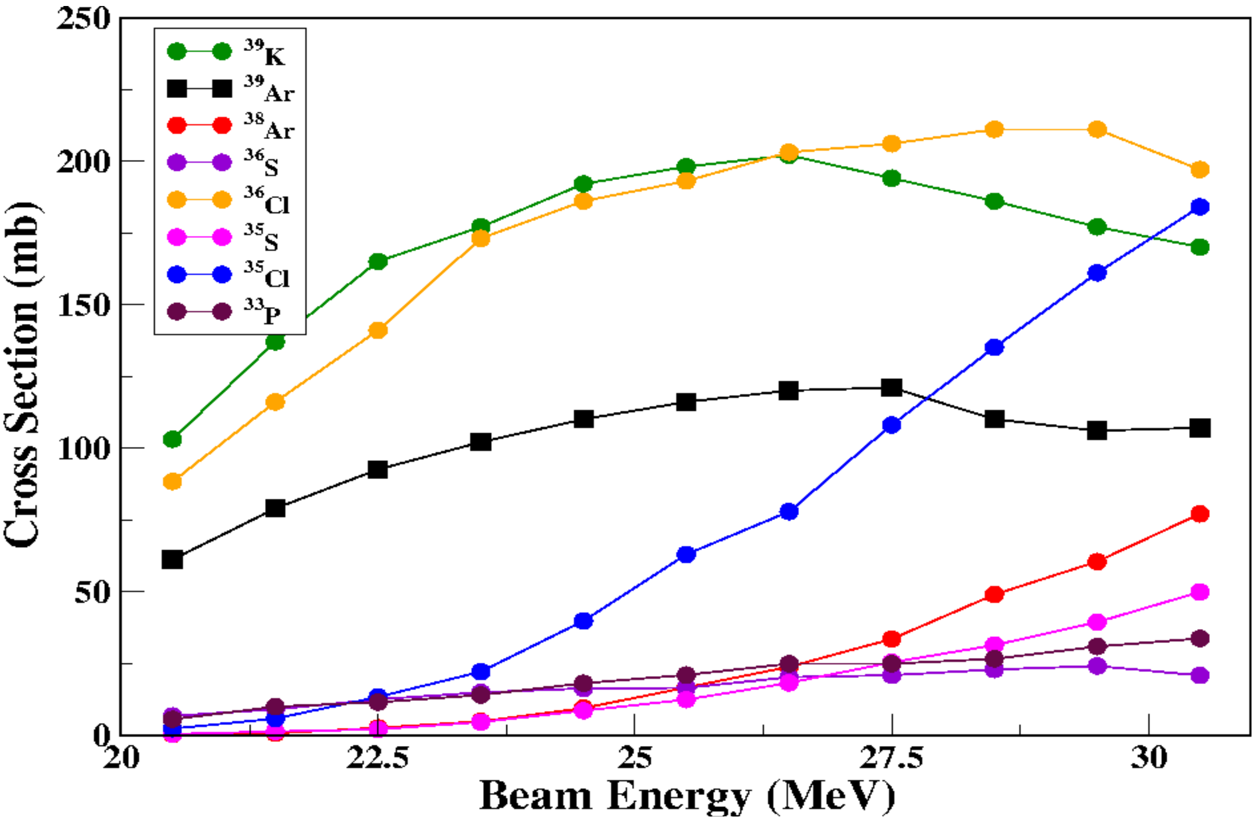

Figure 2.4: The calculated cross section for the major decay channels from the compound nucleus, ^{41}K. The desired cross section, ^{39}Ar, is labeled using a black curve and square data points. All calculations were completed using LISE++ [5].

thinner ^{27}Al target, with a thickness of 6 μg/cm^2, was produced with a tantalum backing using an evaporation process. The thinner target was not utilized in the end, however.

In order to detect charged particles emitted from the compound nucleus, a particle telescope was used (see Figure 2.5). The particle telescope consisted of two silicon detectors (dE and E detectors) of thickness 100 μm and 1000 μm, respectively, [33] and was placed at 0° relative to the beamline. The particle telescope allowed for a particle identification (PID) spectrum to be created. Figure 2.6 shows one such PID. The x-axis is the total energy deposited in the E and dE detectors, while the y-axis is the energy deposited only in the dE detector. Each band corresponds to a particular charged particle. Starting from the bottom: protons, then deuterons, tritons, and lastly, the highest band are alpha particles. The generated PID spectrum allows for the various charged particles to be distinguished from one another and ultimately allows for the selection of

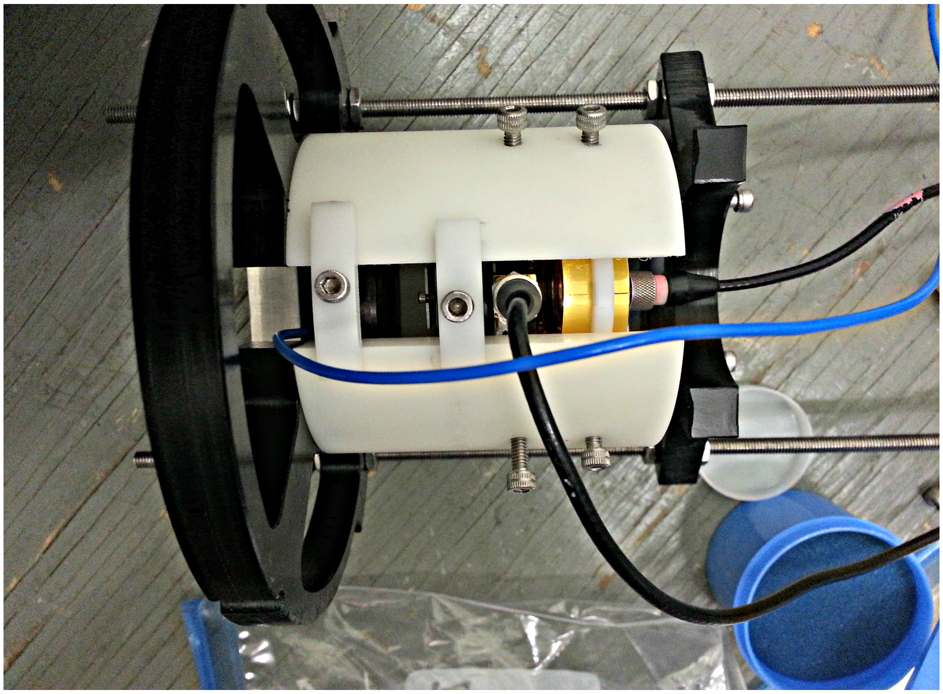

Figure 2.5: The particle telescope is comprised of, from left to right, a dE and E detector, both made of silicon. The telescope allows for charged particles to be detected and for a PID to be formed.

events that occur in coincidence with a particular decay channel. The bending seen in the low energy region of the proton band arises from the fact that the E detector was not thick enough for a complete deposit of energy from the Z = 1 charged particles.

Accompanying the particle telescope are 10 High-Purity Germanium detectors (HPGe), three of which are CLOVER detectors with Bismuth Germanate (BGO) scintillating shields. CLOVER detectors are four Germanium (Ge) single crystals housed in one cryostat. Figure 2.7 shows the entire gamma (γ) array, with the three CLOVERS and two single HPGe sitting at 90°, two single crystal HPGe at 35°, and the remaining three HPGe single crystals at 145° relative to the beam. Figure 2.8 depicts a basic schematic of a CLOVER detector. CLOVER detectors are beneficial for their add-back function and Compton suppression capabilities, due to the BGO shields. Additionally, CLOVER detectors are four times more efficient than single crystals and are capable of determining the full energy of Compton scattered/absorbed photons between two or more crystals [34].

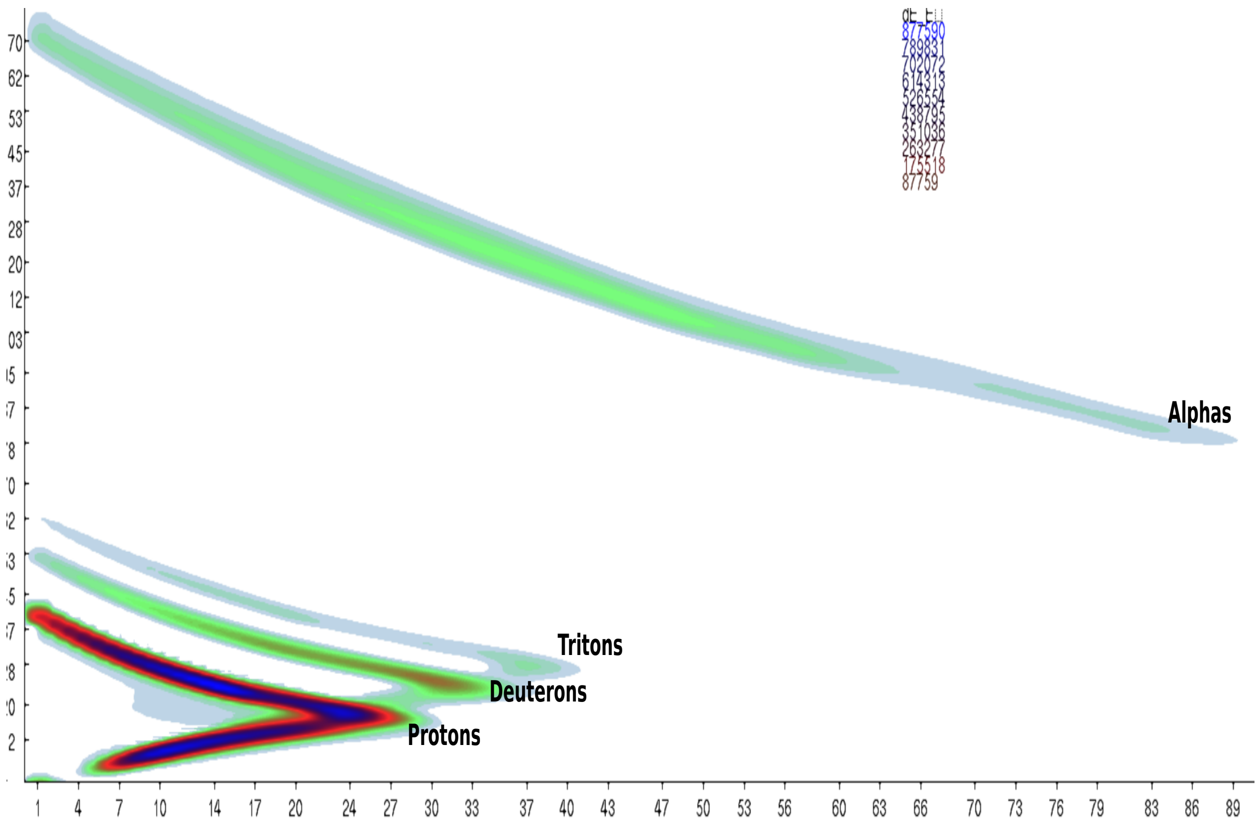

Figure 2.6: Particle identification spectrum with the energy deposited in the E detector on the x-axis and the energy deposited in the dE detector on the y-axis. A banana gate can be made around one of the four bands to make a selection on protons, deuterons, tritons, or alphas respectively.

The use of the HPGe detectors provide γ detection with efficiencies up to 7% for 1-MeV γ. Combining the HPGe detectors with the particle telescope enables particle-γ-γ coincidences to be recorded. These coincidences allow for a specific decay channel to be selected (via the PID spectrum in Figure 2.6) to show all γ transitions that occur in coincidence with the emission of a particular charged particle. The selectivity becomes useful when trying to filter out isotopes created in the reaction that have a much higher cross section than ^{39}Ar, such as the chlorine isotopes, which are created via the α channel.

In order to construct the particle-γ-γ events, a XIA Digital Gamma Finder, Pixie-16, was used. The Pixie-16 samples the waveform of each of the HPGe crystals, the BGO shields, and the two Si detectors at a rate of 100 MHz each [35]. In order to obtain proper timing, a Leading Edge

Discriminator (LED) was used rather than a Constant Fraction Discriminator (CFD). LED and CFD definitions and uses will be explained in Chapter 3.

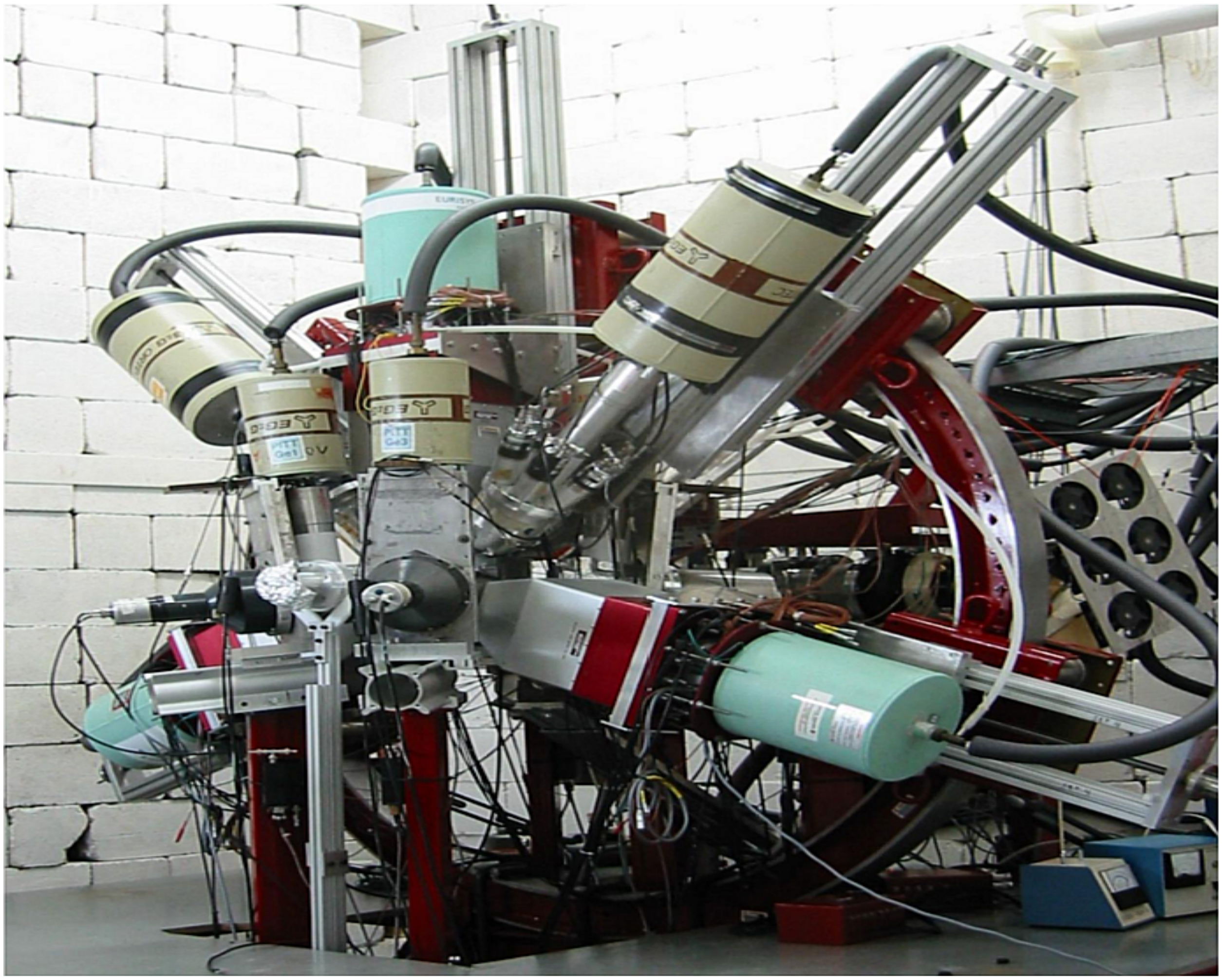

Figure 2.7: The FOXLAB gamma spectroscopy system is comprised of 10 HPGe detectors (three CLOVER detectors and seven single crystals), positioned at 35°, 90°, and 145° relative to the beam. The particle telescope is placed at the center, positioned at 0° relative to the beam.

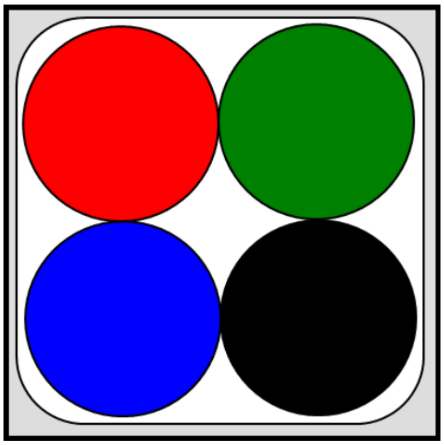

Figure 2.8: A schematic drawing of a CLOVER detector, showing the four distinctive single crystals (red, green, blue, and black) all housed in one cryostat, with a BGO shield (in gray) surrounding the HPGe cluster.

CHAPTER 3

EXPERIMENTAL RESULTS: ^{39}Ar

A fusion-evaporation reaction, as described in Chapter 2, is capable of producing many different reaction products. The abundance of reaction products can flood the digital acquisition system with several events occurring at one time. That means that γ rays come flooding in from the various reaction products. Adding a particle telescope and requiring that a charged particle must be detected, however, reduces the number of events that are collected, allowing for a much cleaner spectrum. In addition to requiring at least one charged particle to be detected, another technique

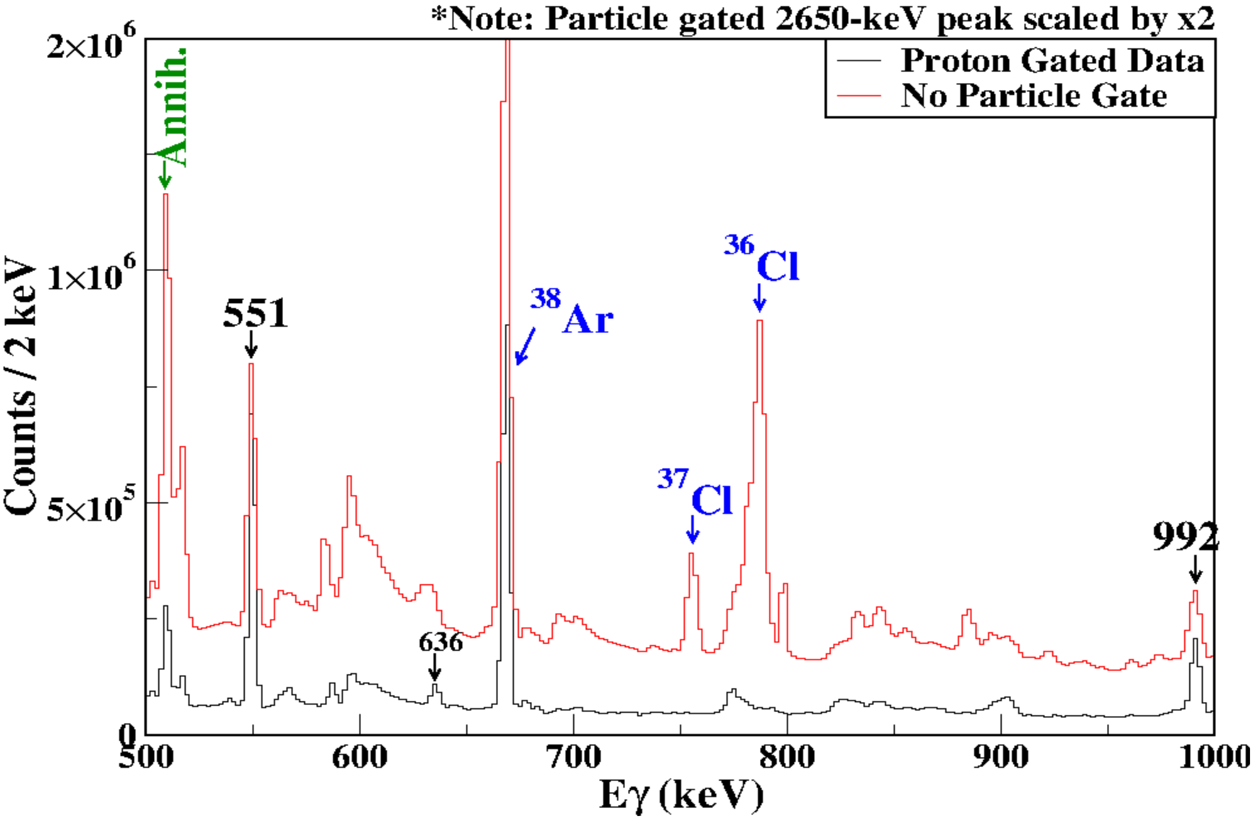

Figure 3.1: Spectra showing the comparison of data when requiring a proton (black) verses requiring any charged particle to be detected in coincidence with a γ ray. The black curve is scaled such that the 2650-keV γ ray peak is scaled by 2x.

to increase the cleanliness of the spectra is to select data that is in coincidence with a particular charged particle. The particle-gated spectra can be generated by making a gate on the various charged particle bands from the PID, as shown in Figure 2.6.

From Figure 2.4, it is obvious that the α decay mode is predicted to dominate over the proton decay mode: ^{36}Cl has the second highest cross section for this reaction at this particular beam energy. The γ ray transition from the lowest-lying excited state to the ground state in ^{36}Cl is 788.4 keV [1]. Figure 3.1 clearly demonstrates the elimination of the strong 788-keV γ through the application of a proton gate. In the figure, the black curve is the proton required data, whereas the red curve is the data that does not have any particle selectivity applied while still requiring *any* charged particle to be detected. Note that the proton selected 2650-keV γ ray peak was scaled by x2 in order for visual comparison with the non-particle selected data. The labeled peak at 788 keV, belonging to ^{36}Cl, has all but disappeared, including another α channel peak from ^{37}Cl. More so, weaker γ transitions that are overwhelmed by background, such as the 636-keV ^{39}Ar γ transition, become more apparent once the proton selectivity is applied and the overabundance of events are reduced to only events in which a proton was detected in the particle telescope.

3.1 Time Walk

In addition to using a particle gate to increase the selectivity and ultimately increase the cleanliness of the spectra, cuts on the timing spectra can be made allowing for random coincidences to be subtracted out, ultimately improving the peak-to-background ratio. Before a time cut is made, it is important to explain the two typical methods of timing provided by the XIA Pixie-16 model: CFD and LED. A CFD is a signal processing mode in which the timing pulse is referenced to the time when the pulse reaches some fraction of its ultimate height. Conversely, the LED has a timing pulse that is referenced to when the pulse crosses a set threshold. The point in which the pulse crosses the threshold is sensitive to the amplitude of the pulse, which is directly proportional to the energy of the γ ray responsible for the signal: the greater the energy of the γ ray, the larger the amplitude of the pulse. Figure 3.2 [36] shows how a pulse with a larger amplitude will cross the threshold earlier than a pulse with a smaller amplitude. The crossing of the threshold at various points in time depending on the energy of the γ ray is known as *time walk*. The time walk

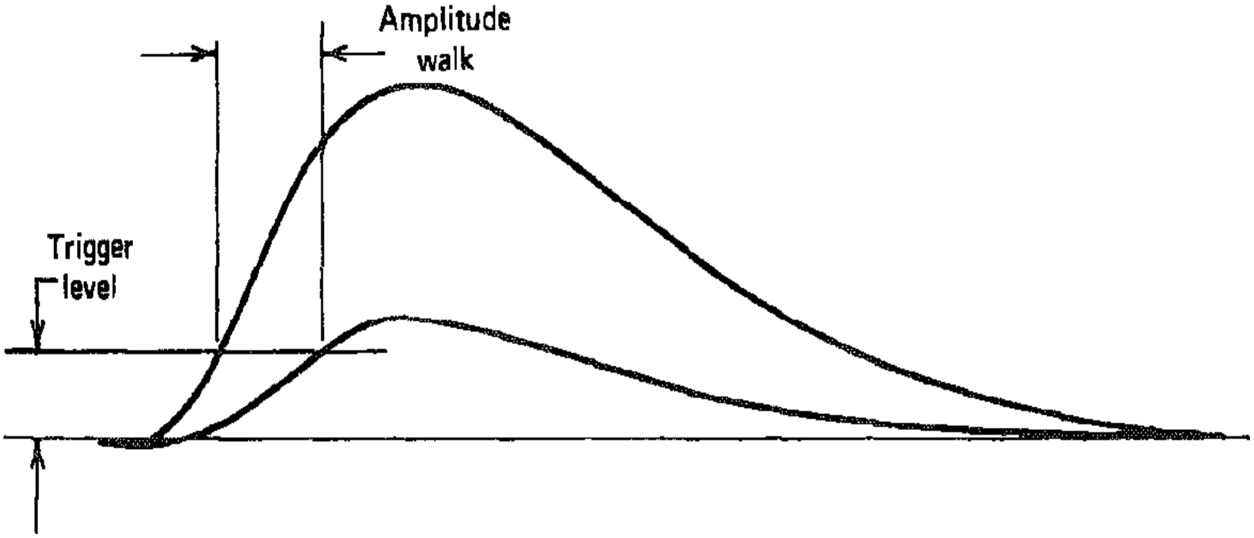

Figure 3.2: Schematic drawing of Leading Edge Discriminator. The Leading Edge Discriminator uses a set threshold as the starting point for when the logic pulse is emitted. The amplitude of the signal, and thus the causation of time walk, crosses the threshold at different times depending on the energy of the particle responsible for the signal: high-energy particles will have a larger amplitude and will cross the threshold sooner than a particle with a lower energy and smaller amplitude.

causes the timing signal to be broad and selecting a timing mode that does not exhibit time walk is preferred. The CFD does not exhibit time walk, whereas the LED does.

The XIA Pixie-16 firmware does provide a CFD mode in which the timing signal does not "walk" with pulse height, but there is some problem with the proprietary firmware and the time resolution is too broad. To work around this firmware problem, the LED was used and requires a time walk correction to make tight time cuts, ultimately improving the peak-to-background ratio. The correction was done with the analysis software.

Figure 3.3 is a timing spectrum constructed using the Leading Edge Discriminator and demonstrates how the time stamp of the timing spectrum changes depending on the energy of the γ ray. The green curve, as seen to the left, comes from the high-energy γ rays, whereas the red curve, as seen on the right, results from the low-energy γ rays. The black curve is the sum of all energy γ rays. For visual comparison, the low-energy and high-energy curves were scaled by x5. Figure 3.3 is the timing spectrum taken from only one single crystal. Each of the 19 crystals in the array

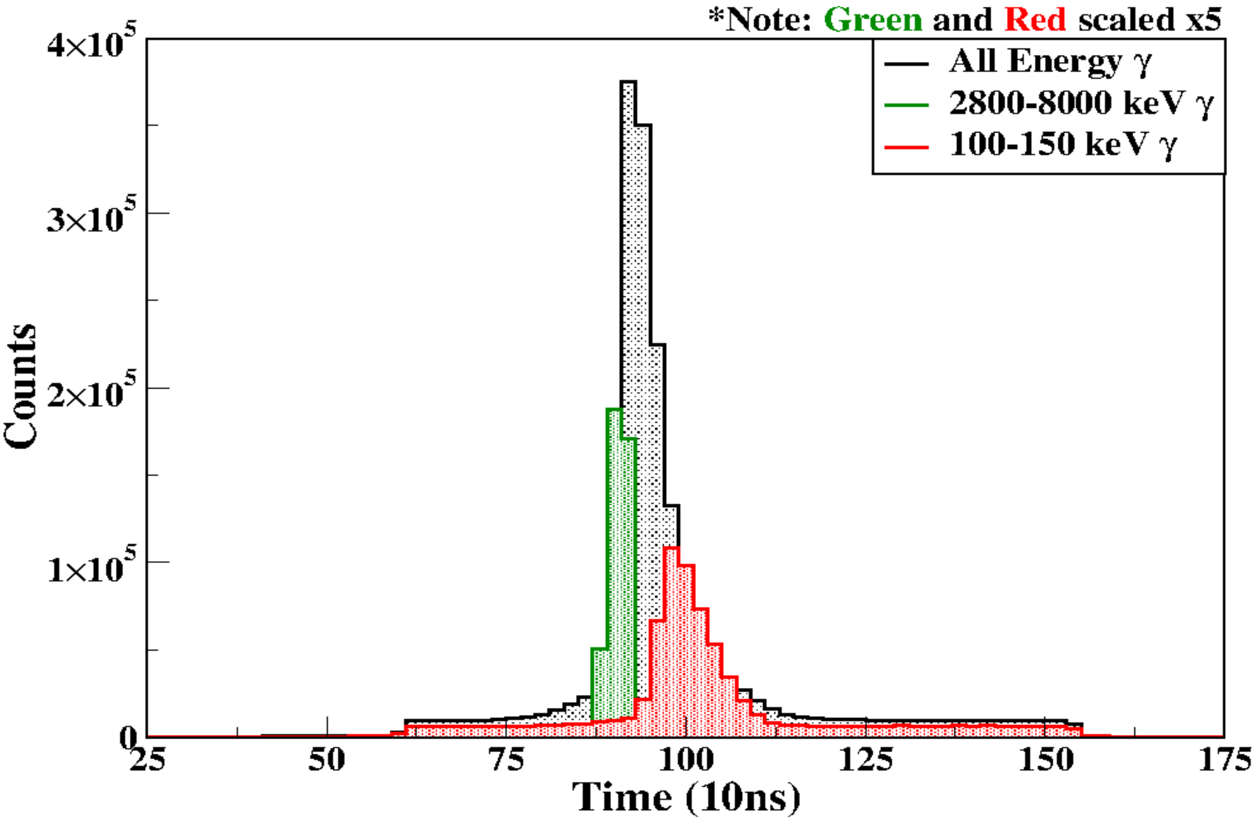

Figure 3.3: Timing spectrum showing the time walk that is created using the Leading Edge Discriminator. The spectrum is taken from a single crystal HPGe detector placed at 90°. The black curve is all-energy γ rays summed, the green curve is high-energy γ rays, and the red curve is low-energy γ rays. Clear displacement of the time stamp between the high- and low-energy γ rays is intrinsic of time walk.

exhibit similar time-walk behavior as such.

In order to correct for the time walk, each of the 19 crystals need to be individually corrected. To correct the crystals, the time stamp for various energy ranges is histogramed. A “smoothing” process then creates a smooth curve that contains the time stamp for all energy ranges for each single crystal. Figure 3.4 shows the smoothed curve for one of the single crystals. Once this information is collected for all 19 crystals, a time-walk correction program is applied. The program takes the time of each pulse and adds or subtracts a constant in order to align all time stamps to be equal to 100 ns, regardless of the energy of the γ ray. Once the correction has been applied to the data, it becomes apparent that the time walk has been corrected for. Figure 3.5 shows the

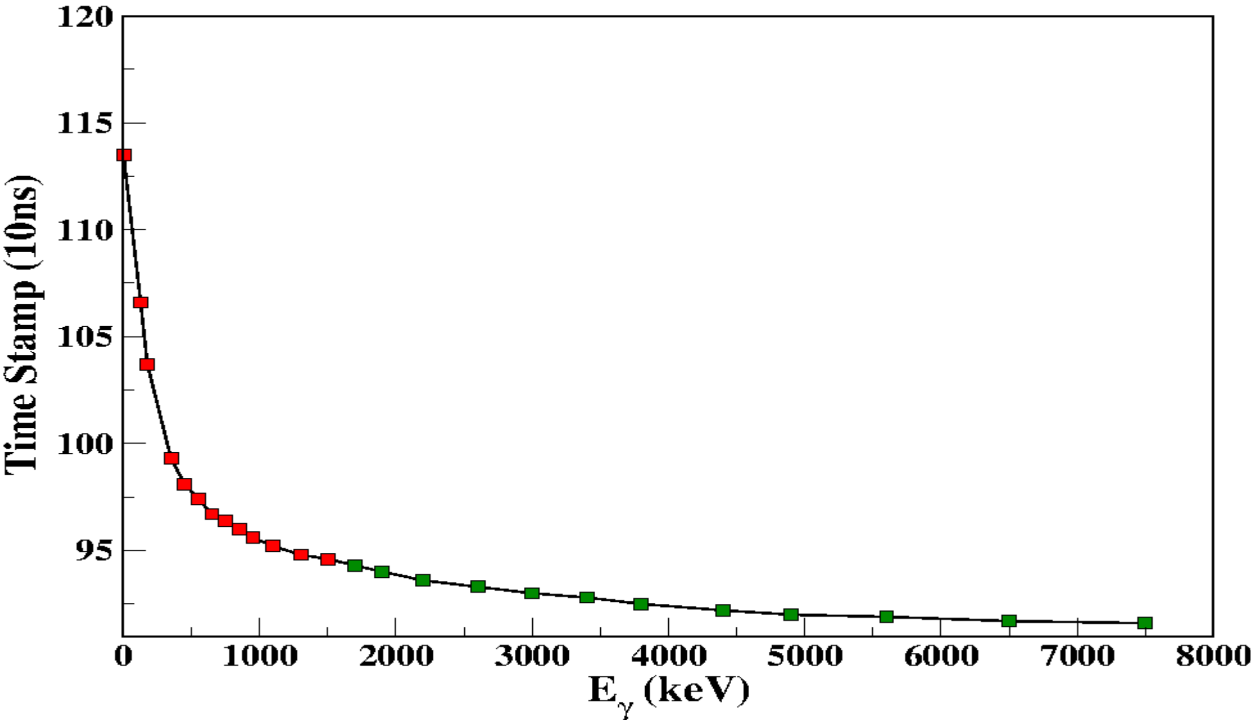

Figure 3.4: Using time spectra, as shown in Figure 3.3, the above graph can be produced for each individual crystal (each crystal inside a CLOVER detector must be treated separately). The graph shows the various time stamps recorded at different γ ray energy ranges. The curve is then smoothed to include time points between each data point and then a time walk correction is further applied. The time walk correction takes each point and adds or subtracts a constant to make each energy range have a time stamp of 100 ns.

same timing spectrum as shown in Figure 3.3 with the time-walk correction applied. Note that the low- and high-energy curves are scaled by x10 for visual comparison. Notice that both the high-energy and low-energy curves have the same centroid, and ultimately the same time stamp, clearly showing that the time walk has been corrected. There is a significant improvement to the FWHM which allows for a narrow time gate to be made along with much larger random subtraction gates on either side of the timing peak.

Figure 3.6 shows the improvement that comes from the application of a timing gate in addition to a proton gate. The red curve is the data that only has a proton selection applied and the black curve has both proton selectivity and narrow timing gate. As mentioned prior, having the time

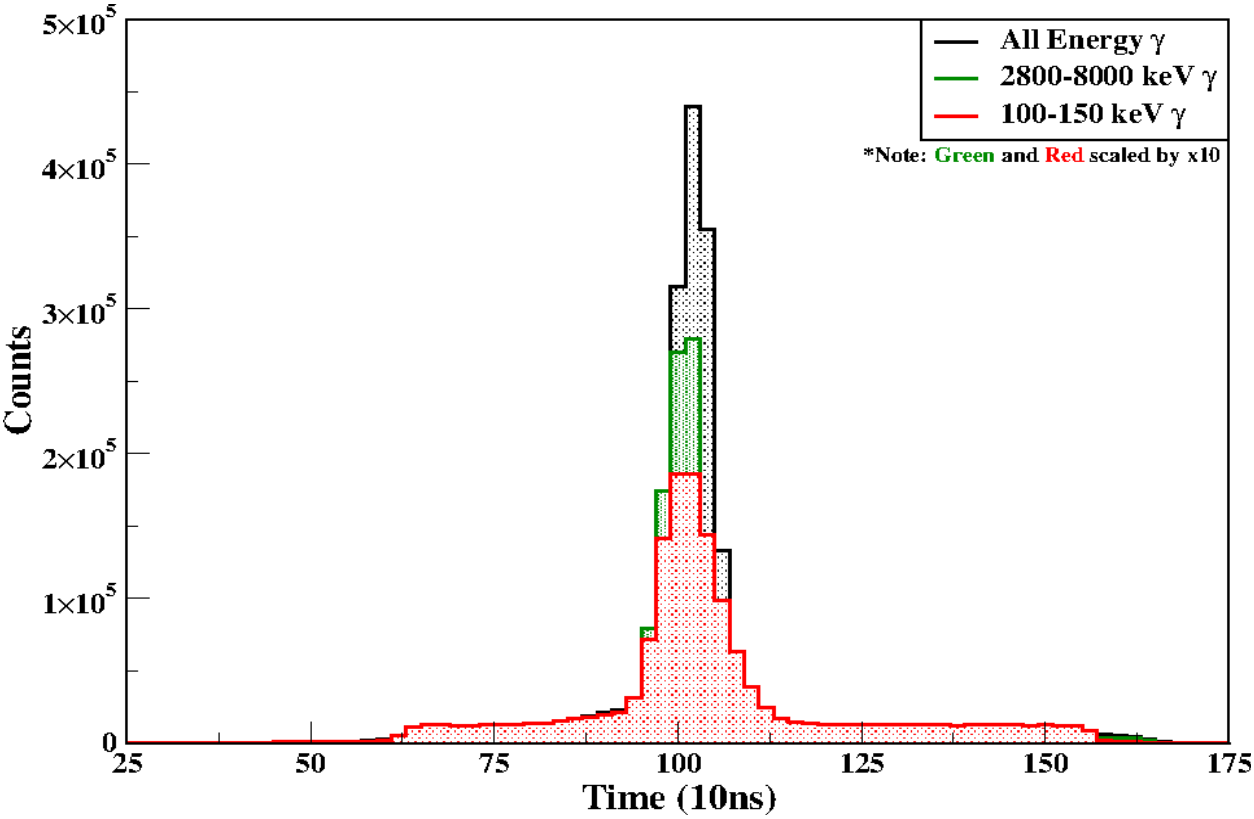

Figure 3.5: Above is the same time spectrum as shown in Figure 3.3 with the time-walk correction applied. Notice now that both the low- and high-energy γ ray peak now have the same centroid, showing that the time walk has indeed been corrected and all energy γ rays have the same time stamp.

gate allows for the random coincidences to be subtracted and increase the peak-to-background ratio. One origin of a random coincidence could come from the neutron decay channel. Because the neutrons are not detected through the particle telescope, events could be recorded where γ rays are detected that come from two different events which were close in time and appear as if they were the same event. One might come from neutron evaporation, giving a γ ray in ^{39}K while a proton evaporating from a different event is detected in the particle telescope. The time gates, allows for these random coincidences to be eliminated to a large extent and can be seen through the significant reduction in the 783-keV γ transition from ^{39}K or the complete reduction of the 351-keV peak from ^{21}Ne [1] (see Figure 3.6). The ^{21}Ne perfectly demonstrates how contamination that is not eliminated entirely through the particle gate can be further reduced using the tighter

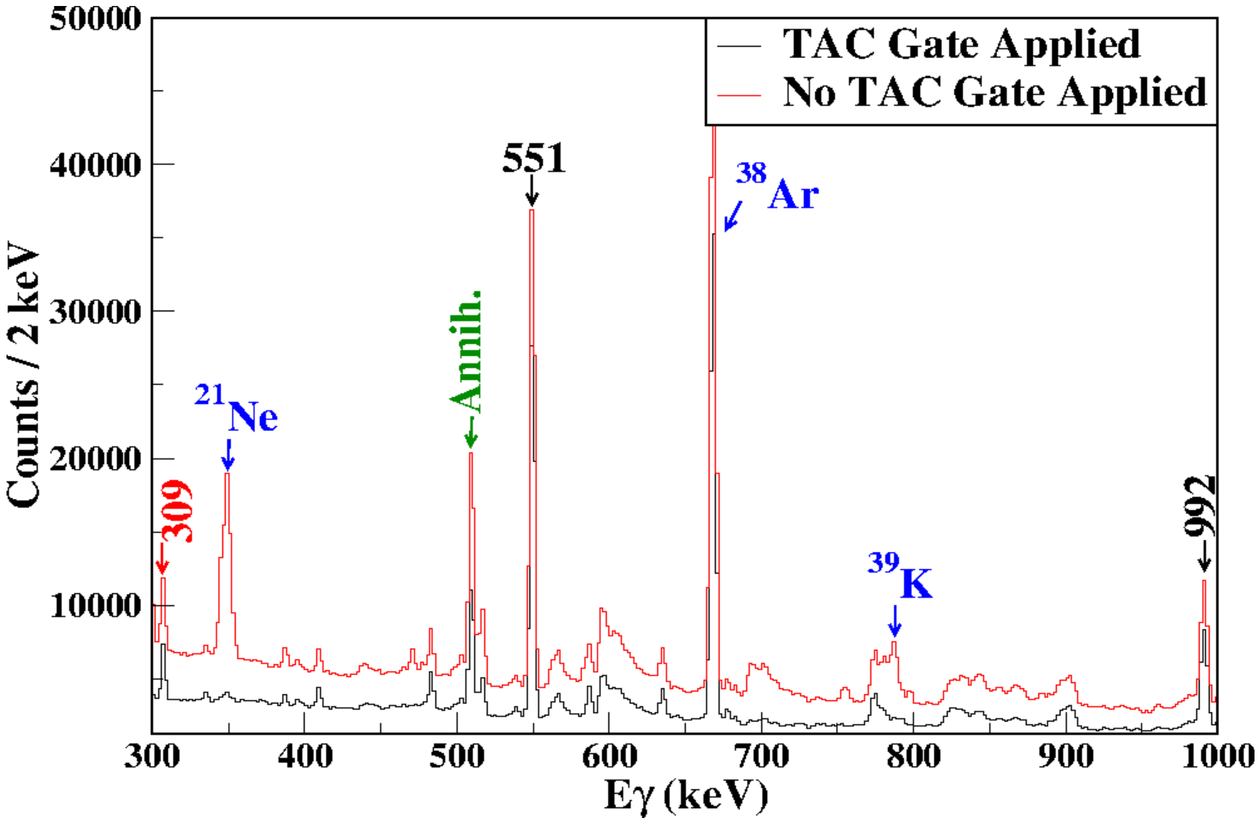

Figure 3.6: Spectra showing the comparison between data with a proton gate and NO time-walk correction applied vs data with a proton gate and time-walk correction. It is evident that correcting for the time walk allows for narrow time gates to be made, which in turn, reduces the contamination from the neutron decay channels. Notice that the peaks labeled in blue are significantly reduced, as well as the 511 keV that comes from positron annihilation. The known peaks from ^{39}Ar, however, are only slightly reduced.

timing gate: ^{21}Ne is created via the α-n channel from the ^{14}C+^{12}C reaction, where the ^{12}C is simply carbon build-up on the target. Even the large 670-keV γ transition from ^{38}Ar [1] is reduced significantly. The desired peaks, such as the 551-keV or the 992-keV γ transitions are only reduced slightly, leaving a spectrum with very high selectivity.

3.2 Uncovering High-Spin

The high selectivity that is achieved through the use of a proton gate and tight timing gates significantly reduces the chances of observing contaminant γ-ray transitions in the γ-γ matrices,

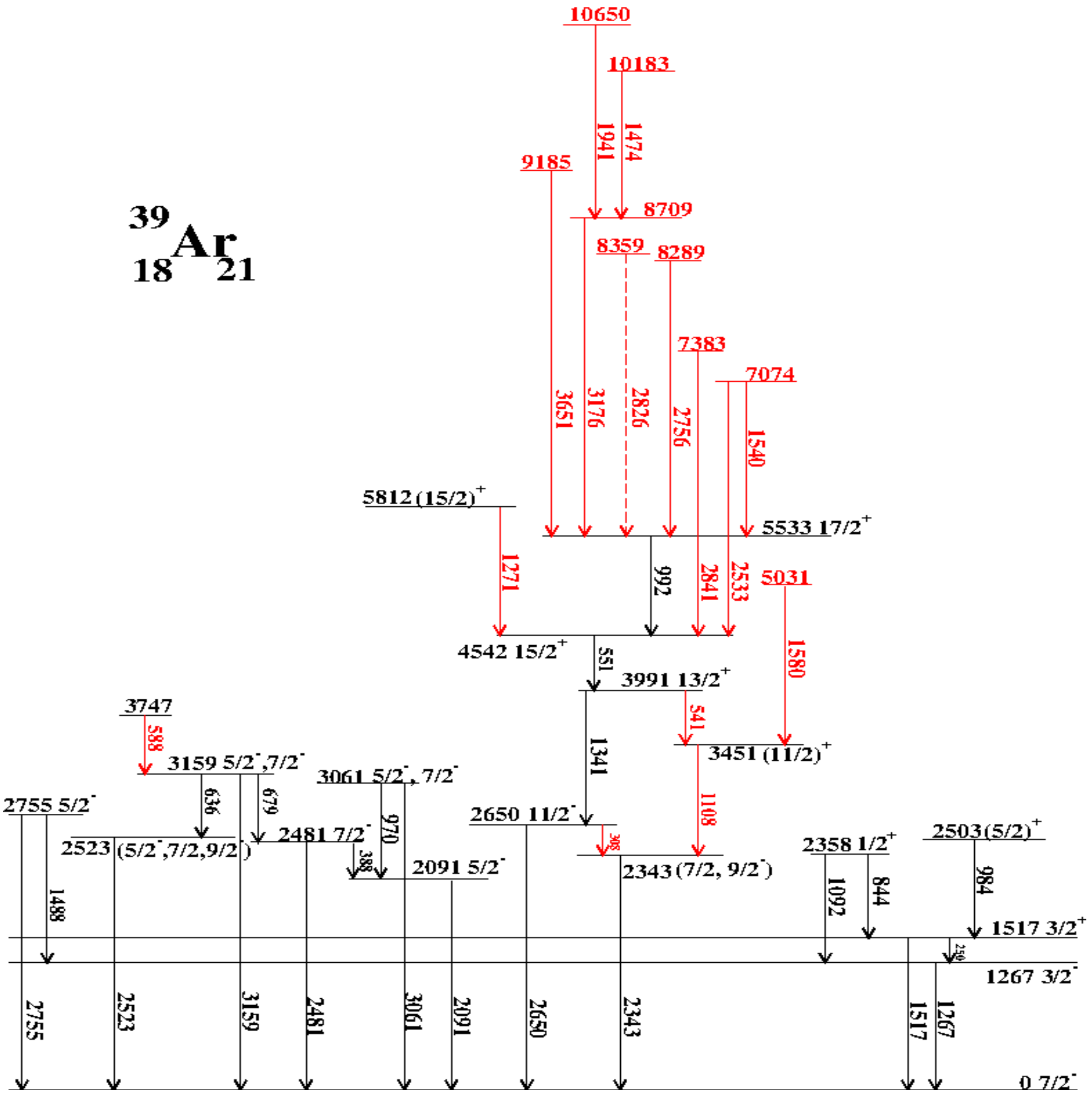

Figure 3.7: Level and decay scheme showing all the states and γ transitions in ^{39}Ar as observed in the present experiment. All black lines are previously observed states or γ transitions, where as red lines denote newly observed states and transitions.

which are constructed using the in-house GNUSCOPE software. With the reduction of contaminant transitions, the matrices consist more purely of ^{39}Ar γ transitions that are in true coincidence with each other, facilitating the building of the level scheme, as seen in Figure 3.7.

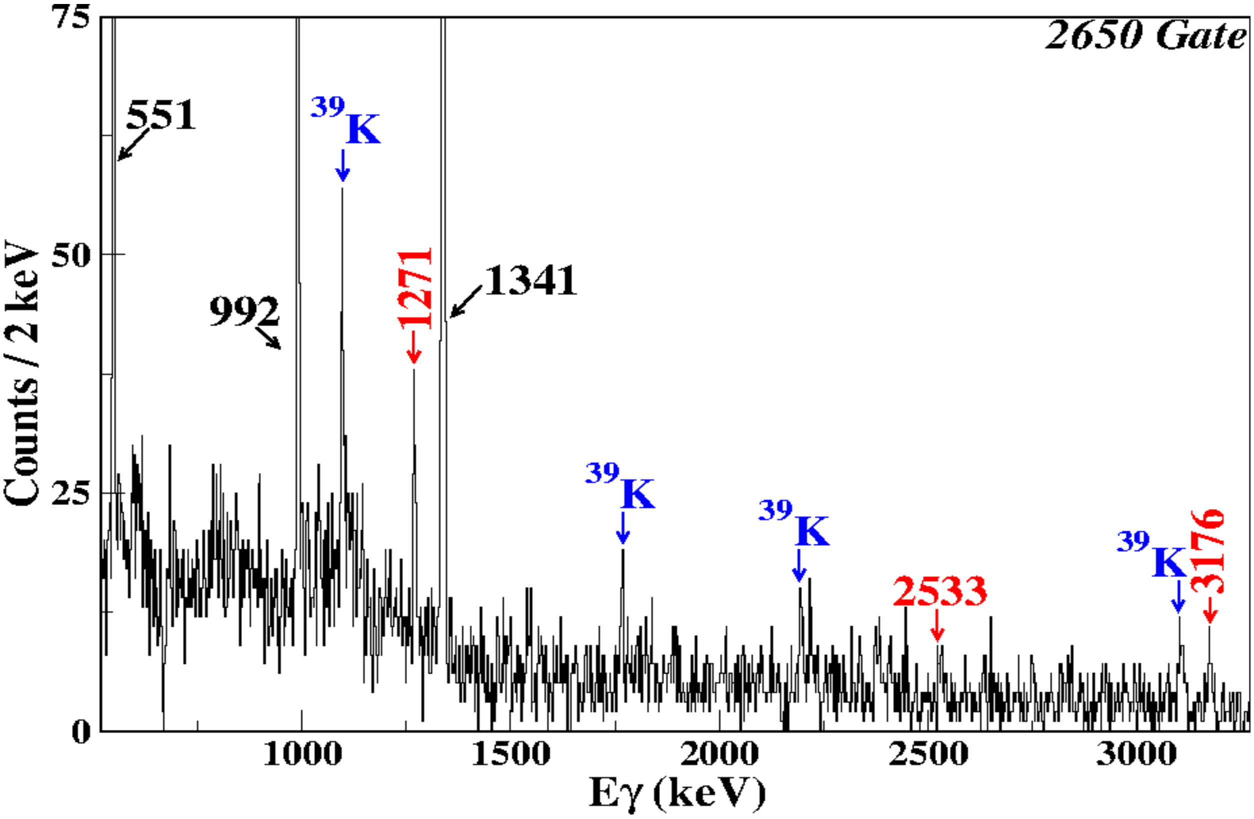

Figure 3.8: Spectrum taken from a gate made on the strongest γ transition in ^{39}Ar, 2650 keV. The spectrum shows three newly observed γ transitions, as shown with a red label, along with the three strongest γ rays that make up the yrast decay sequence.

Two γ transitions are said to be in true coincidence when they both appear in a gate made from the projection on each of the γ-ray peaks. The analysis process starts with previously observed γ transitions, pictured as black arrows in Figure 3.7, such as the strongest γ in ^{39}Ar at 2650 keV. A projection, or a “gate”, is made around the peak positioned at 2650 keV: the result, as shown in Figure 3.8, shows the γ rays that occur in coincidence with the 2650-keV γ. Notice that there are three strong peaks at 1341, 551, and 992 keV. Notice also that these three peaks correspond to the three previously reported γ transitions feeding directly into one another, cascading down to the 2650-keV γ ray, as shown in Figure 3.7. These three peaks are labeled using black, corresponding to the fact that they were previously observed. The peak labeled “Annih.” in green, is the signature 511-keV γ ray that comes from electron-positron annihilation. The remaining peaks, labeled in red, correspond to newly observed γ transitions. Since the 1271-, 2533-, and 3176-keV γ rays are present in the 2650-keV gate, they are said to be in coincidence with at least the 2650-keV γ transition. Separate gates must be made on each of the individual γ rays to be sure that the 2650-keV peak is present. Its presence gives greater confidence in the coincidence relationship with the 2650-keV γ transition.

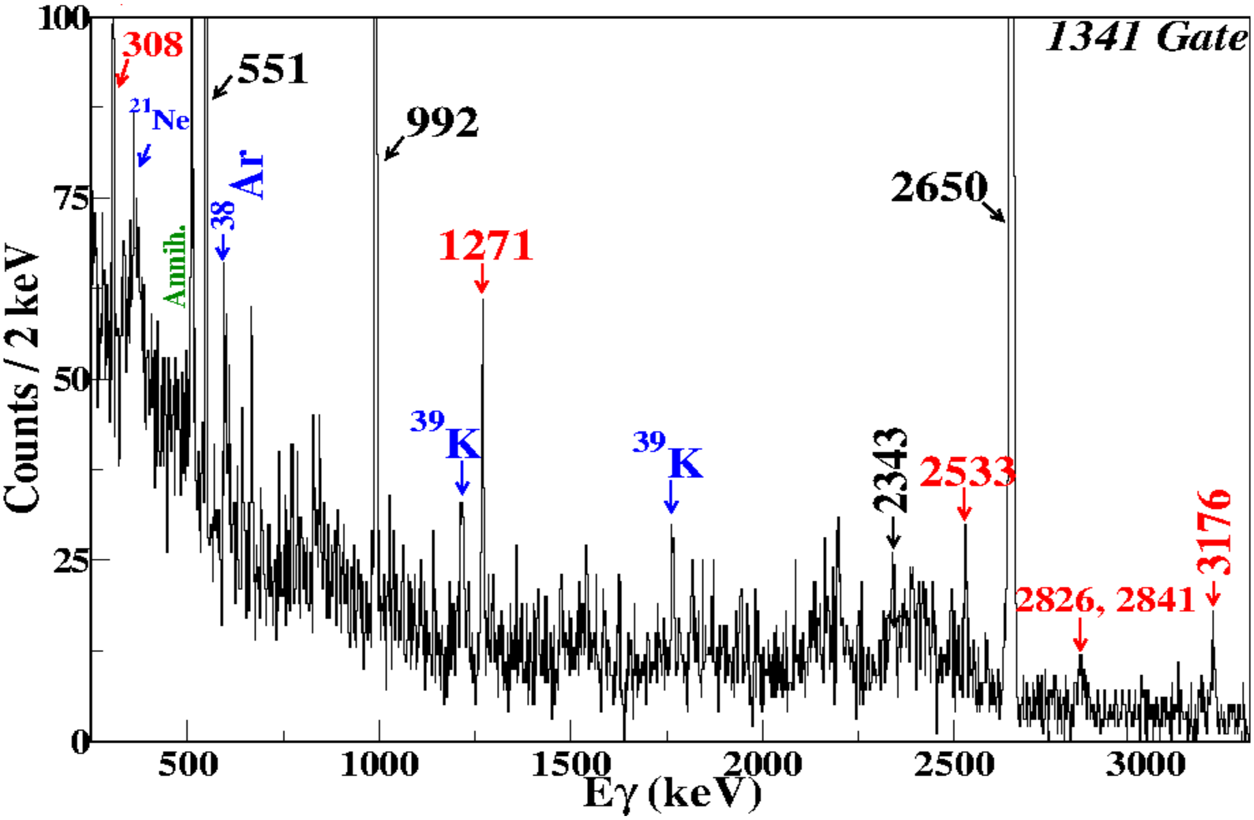

Figure 3.9: Spectrum taken from a gate made on the 1341-keV γ transition, showing five newly observed γ transitions and the other strong γ rays that make up the yrast decay sequence.

Before trying to determine how the various γ rays feed into one another, it is advantageous to double check the coincidence of the previously reported γ transitions. Figures 3.9, 3.10, and 3.11 all show spectra produced by making corresponding gates on each of the three strongest, previously reported, γ transition. Notice that each spectrum shows clear evidence for the remaining two γ rays and also the 2650-keV γ ray. It is fair to assume that the previously reported feedings in and out of these γ rays are as stands.

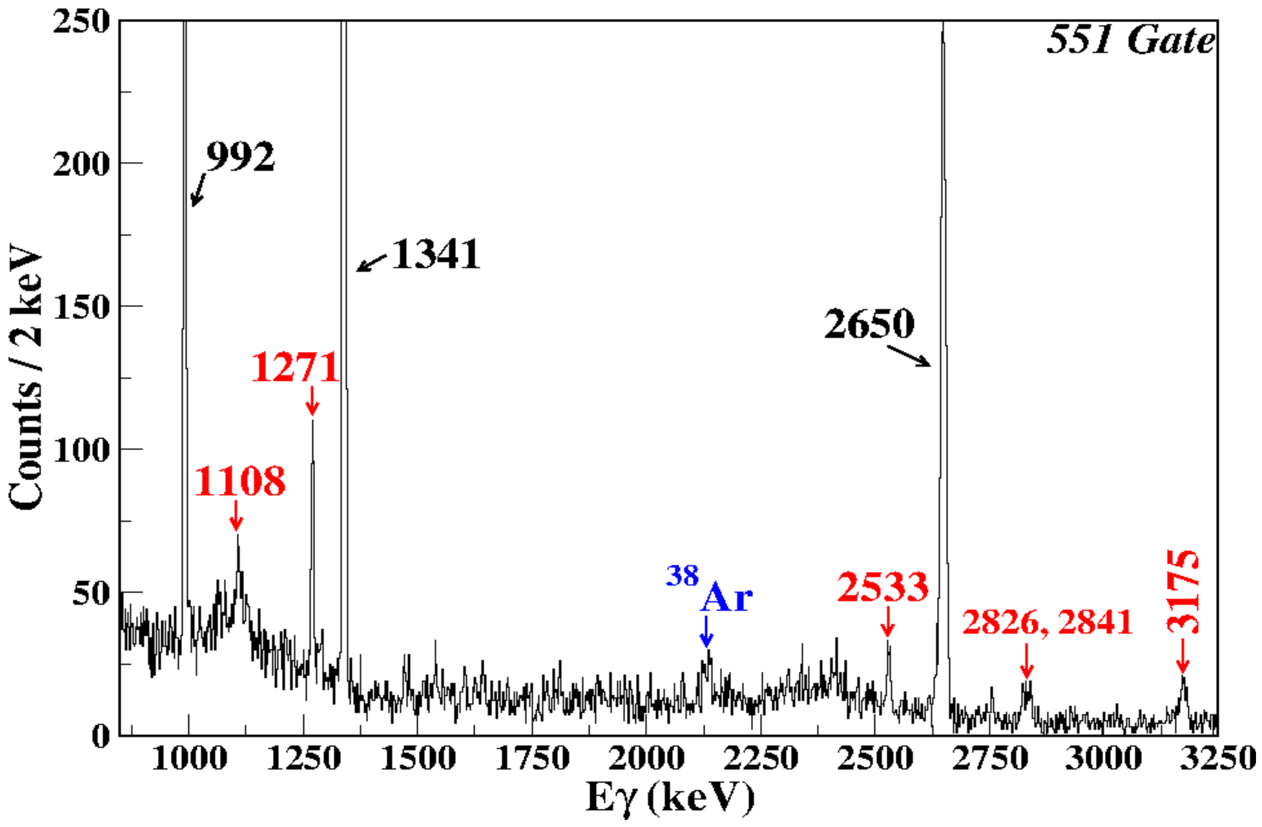

Figure 3.10: Spectrum taken from a gate made on the 551-keV γ transition, showing five newly observed γ transitions and the strong γ rays that make up the yrast sequence.

Heavy-ion reactions populate more favorably high-spin states. Because the γ decay strengths increase rapidly with transition energy, but *decrease* even more rapidly for spin changes of $2\hbar$ or more, the decay sequence of high-spin states tends to decay through the lowest state of a given spin. These special states are called “yrast” and the decays between them tend to be the most intense. With that, the intensity of the four γ rays as described above, along with the previously reported spin assignments demonstrate that they form the yrast sequence. This high-spin yrast sequence becomes rather important, as will be shown in Chapter 4, when trying to determine the J^{π} of newly observed excited states.

Not only do the four discussed γ transitions become important when helping to decide the J^{π} of newly observed excited states, they also make an excellent tool in uncovering the location of the new excited states. Notice that in Figures 3.8, 3.9, and 3.10 there is a γ ray residing at 1271 keV,

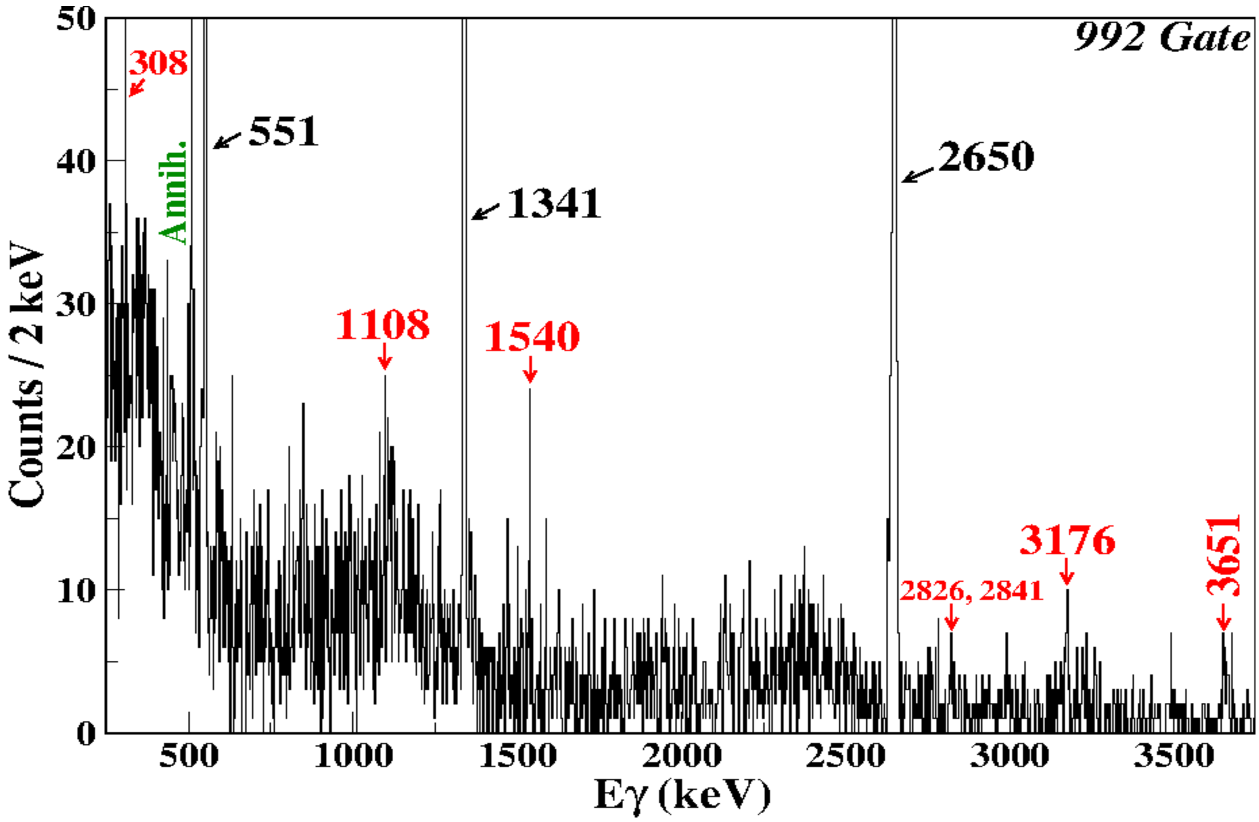

Figure 3.11: Spectrum taken from a gate made on the 992-keV γ transition, showing six newly observed γ transitions and the strong γ rays that make up the lower yrast sequence.

but Figure 3.11 does not have the 1271 peak. At first glance it is easy to see that the 1271-keV γ ray is in coincidence with the 2650-, 1341-, and 551-keV γ rays, meaning that it must feed somehow into all three excited states. Since the 992-keV γ spectrum shows no sign of the 1271, it can be assumed that the two γ-ray transitions do not feed into or out of each other, forcing the 1271-keV to feed directly into the 4542-keV state or some state above that will eventually feed directly into the 4542-keV state, completely bypassing the state at 5533 keV. To be certain that this is the case, a reverse gate needs to be made on the 1271-keV γ showing that the spectrum includes a 2650-, 1341-, and 551-keV peak but no 992-keV peak. Figure 3.12 shows the resulting spectrum, clearly showing a 2650-, 1341-, and 551-keV peak and no evidence of a 992-keV peak.

Although it is clear that the 1271-keV γ is in true coincidence with the yrast sequence up to 4542 keV, it is has potential to be problematic. In ^{39}Ar, the first excited state is a $3/2^{-}$ state at

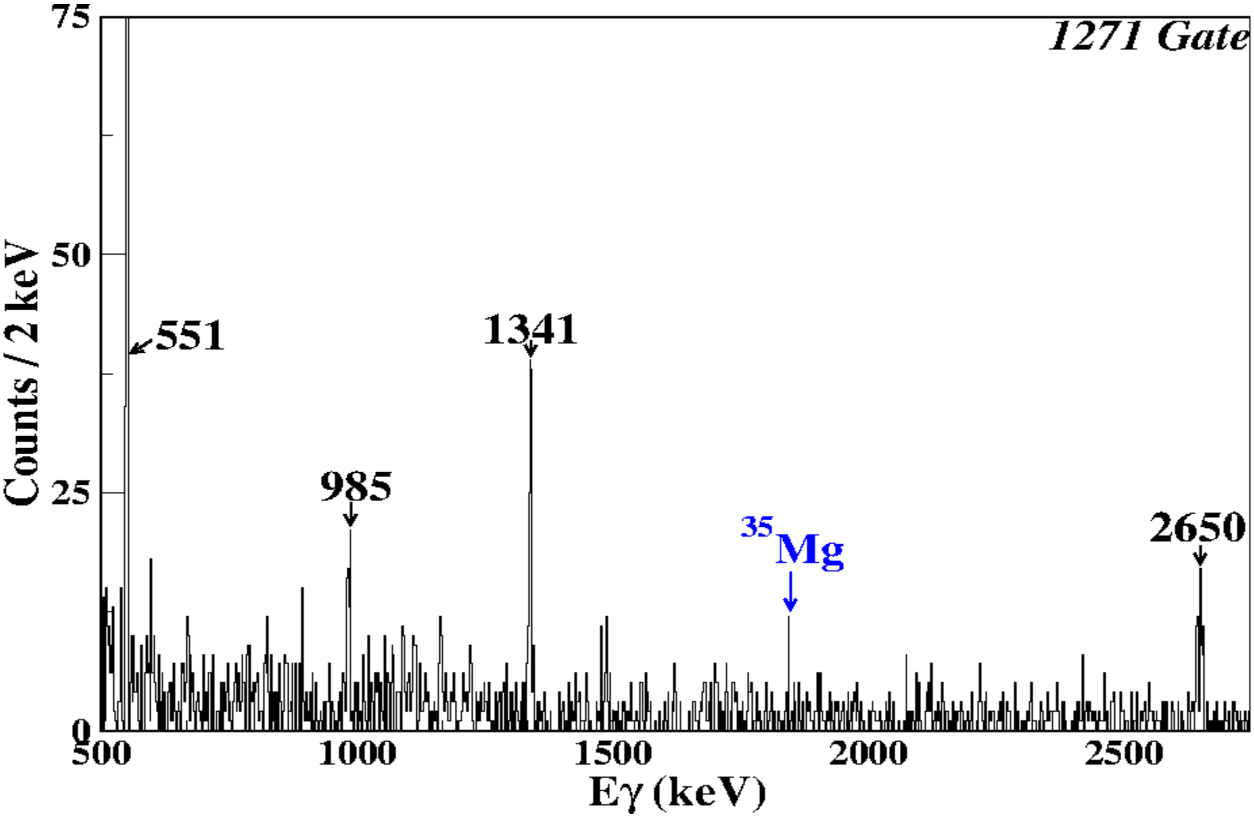

Figure 3.12: Spectrum taken from a cut on the 1271-keV γ transition. This spectrum shows clear coincidence with the 2650-keV γ transition, leading to the fact the 1271-keV γ is different than the 1267-keV γ transition from the first excited state in ^{39}Ar. If the two transitions were the same, then this spectrum would not show any signs of coincidence with the 2650-keV γ since both the 1267- and 2650-keV γ transitions go directly to the ground state.

1267 keV. This state does have a weak, previously reported, γ transition to the ground state with an energy of 1267 keV [1]. It is troublesome that this 1271-keV γ ray is in clear coincidence with the 2650-keV γ transition that goes directly from the 2650-keV excited state to the ground state: if the 1271-keV γ ray is the same as the previously reported 1267-keV γ ray, then the 2650-keV transition should not be showing clear coincidence. Fortunately, further investigation of the 1267 vs 1271 peak shows that the two transitions are actually separate. Figure 3.13 is a spectrum showing that there are two distinctive peaks in the 1270-keV region, thus concluding that the 1271-keV γ ray does in fact exist and matches perfectly to a previously reported excited state of 5821 (10) keV [1].

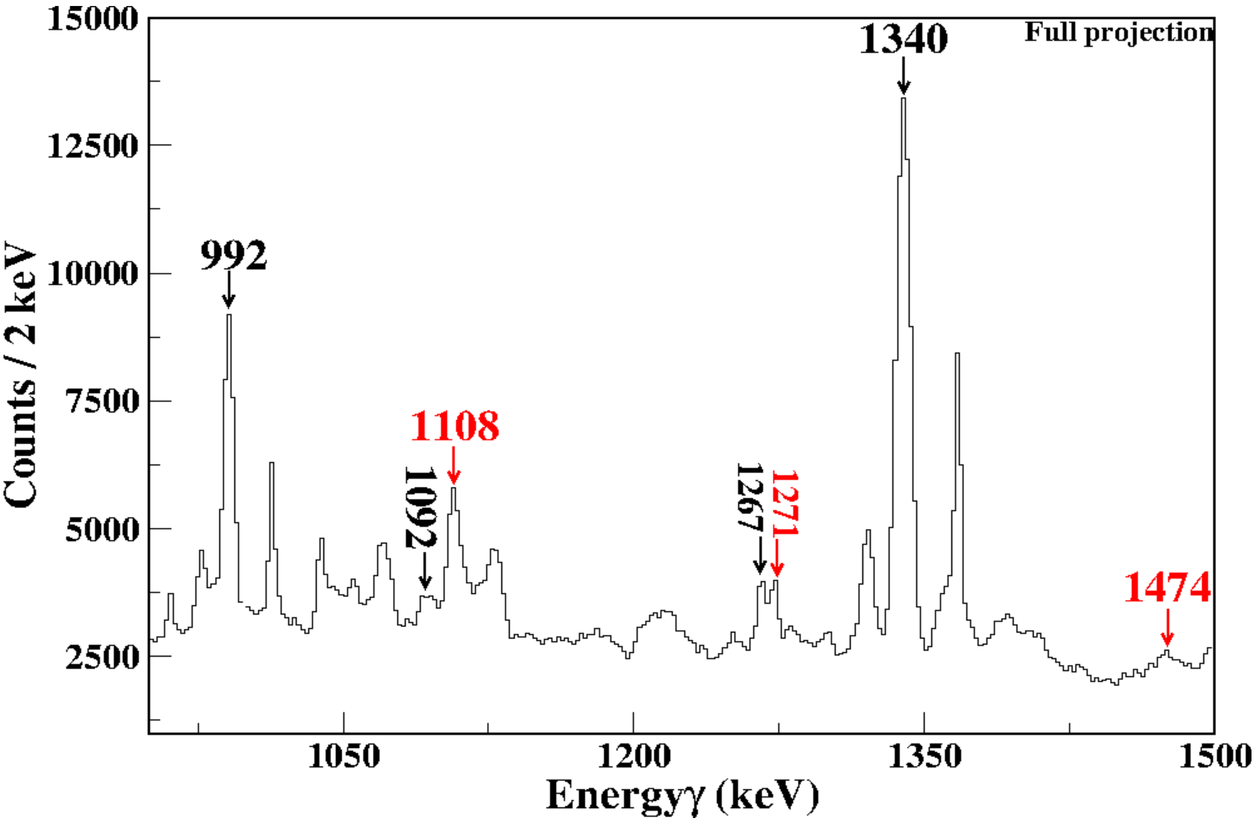

Figure 3.13: Spectrum taken from the full projection of the data and is generated using all of the available data from the experiment, with a proton gate and time-walk corrections applied. The spectrum shows clear separation between the 1267- and 1271-keV γ rays, further proving that the two are in fact different γ transitions.

In addition to the newly placed γ transition from a state at 5812 keV to the previously reported yrast state at 4542 keV, there is one other new γ transition feeding into the 4542-keV state. Figure 3.14 shows the spectrum generated when a gate is made on the 552-keV γ ray. A very evident 2533-keV peak can be seen in the spectrum, implying that the 2533-keV γ ray feeds into the 552-keV γ ray. A reverse gate, generated by making a gate on the 2533-keV peak, shows clear evidence for a 552-keV peak, demonstrating that the two γ rays are in fact in true coincidence with each other. The question now: where exactly does the 2533-keV γ ray belong? To determine the placement of the γ ray, various other gates need to be made to see if the peak is present in any other spectra. Figure 3.9 clearly shows a 2533-keV peak in the 1341-keV γ spectrum, concluding that the 2533-keV should be feeding both the 1341- and 552-keV γ rays from above. The spectrum generated by making a gate on the 992-keV γ ray, as shown in Figure 3.11, has no clear evidence of a peak residing at 2533 keV. Since the 992-keV spectrum has no 2533 keV peak, it can be assumed that the 2533-keV γ ray does not feed into the 5533-keV state, and thus, feeds directly into the state at 4542 keV. The newly generated state has an energy of 7074 keV.

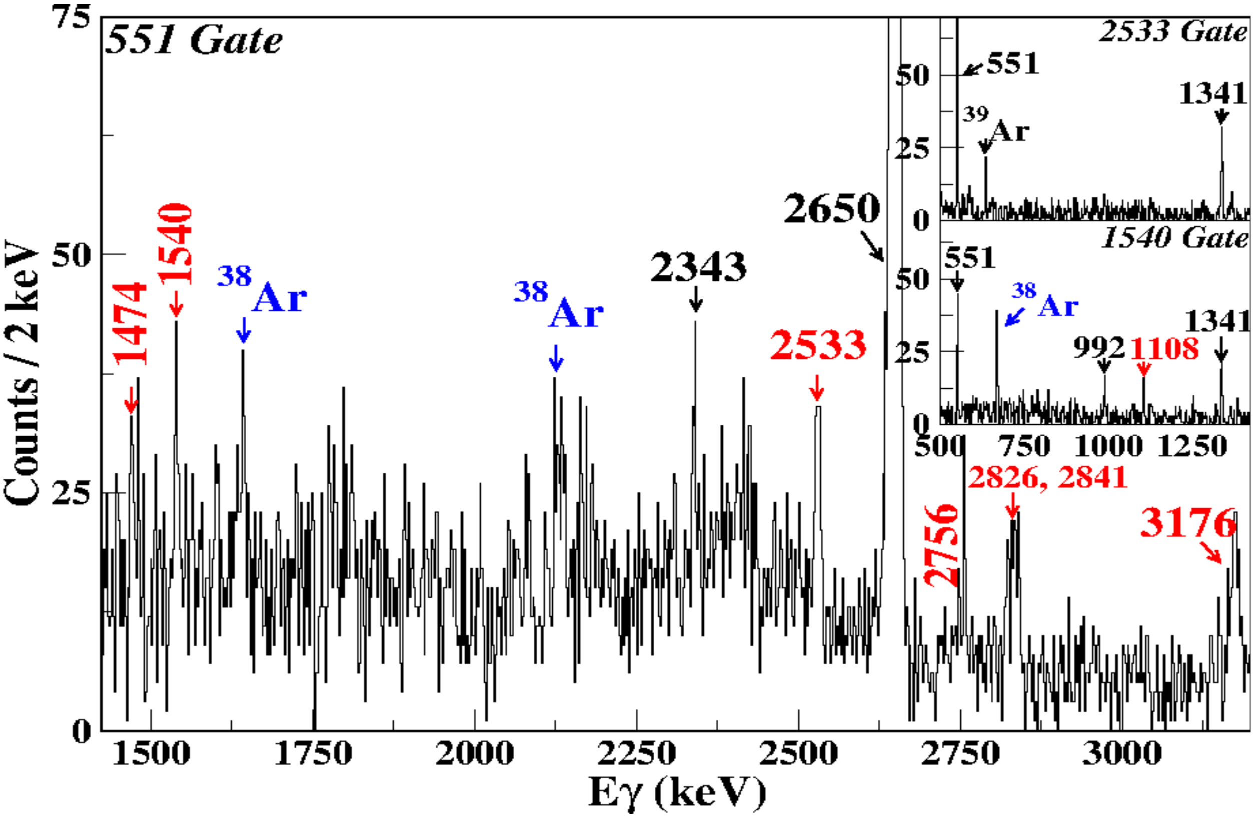

Figure 3.14: This spectrum is an extended spectrum showing the true coincidence of the 1540- and 2533-keV γ rays with the 551-keV γ ray. The larger of the spectra is taken from a gate on the 551-keV transition. The two smaller insert spectra are taken from gates on the 1540-keV (bottom) and 2533-keV (top) transitions. The two insert spectra show clear evidence of the 551-keV transitions and the 551-keV gate shows clear evidence of both the 1540-keV and 2533-keV transitions, proving that they are all in true coincidence.

Figure 3.14 does not only show the newly observed 2533-keV γ transition, it also shows several more: All of the newly observed γ rays are labeled in red. In the same manner, each suspected new γ transition must be checked to make sure that it is in true coincidence with the γ ray with whose spectrum it appeared and if it is in true coincidence then its placement must be determined. As mentioned above, the placement of a γ transition is determined through a series of gates on

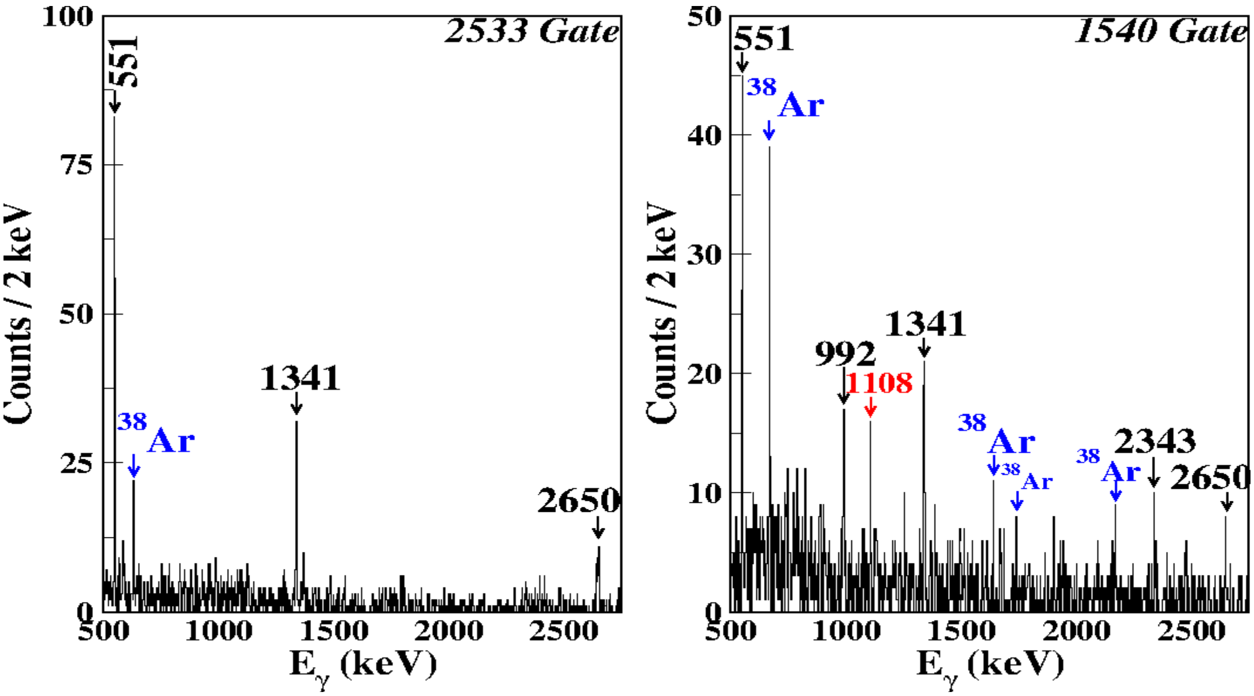

Figure 3.15: Spectra taken from gates made on the 2533-keV (left) and 1540-keV (right) transitions. These spectra show clear coincidence with the 1341- and 551-keV γ rays. The clear lack of evidence of the 992-keV peak in the 2533-keV spectrum shows that the two transitions are not in coincidence with each other and thus the 2533-keV γ transition is placed feeding directly into the 4542-keV excited state. On the other hand, the 1540-keV spectrum does show clear evidence of the 992-keV, meaning that it must feed into both the 4542-keV and 5533-keV excited states. The two newly observed transitions happen to both add up to the same energy of 7074-keV and have no evidence of coincidence with each other.

the various γ transitions. If a particular γ ray is present in one spectrum, then it can be assumed that the γ ray feeds the γ used to generate the spectrum. Likewise, if the γ ray does not appear in a particular spectrum then the γ does not feed into the γ that generated the spectrum. In addition to observing whether or not a γ ray is present in the various spectra, simple addition can also be utilized to help place newly observed γ transitions. Take for example the newly observed 1540-keV γ ray. Figures 3.9 and 3.14 both show a clear 1540-keV peak in the 1341- and 552-keV gated spectra, indicating that the 1540-keV γ feeds both γ rays. Unlike the 2533-keV γ transition, a spectrum taken from a gate on the 992-keV γ ray also shows clear evidence of the 1540-keV peak. Likewise, a reverse gate on the 1540-keV peak shows clear evidence of the 992-keV, meaning the two are also in true coincidence, as seen in Figure 3.15. Coincidentally, if the 1540-keV γ ray feeds directly into the 5533-keV excited state, the summation of the newly observed γ ray and the 5533-keV excited state adds up to a state having an energy of 7074 keV: the same excited state that the 2533-keV γ transition also generated. The proposition that both γ transitions come from the same excited state needs to be challenged. To do so, neither the 1540- or 2533-keV γ ray should be present in the other's spectrum. Figure 3.15 demonstrates that neither γ ray is present in the other's spectrum, proving that they are in fact from the same excited state.

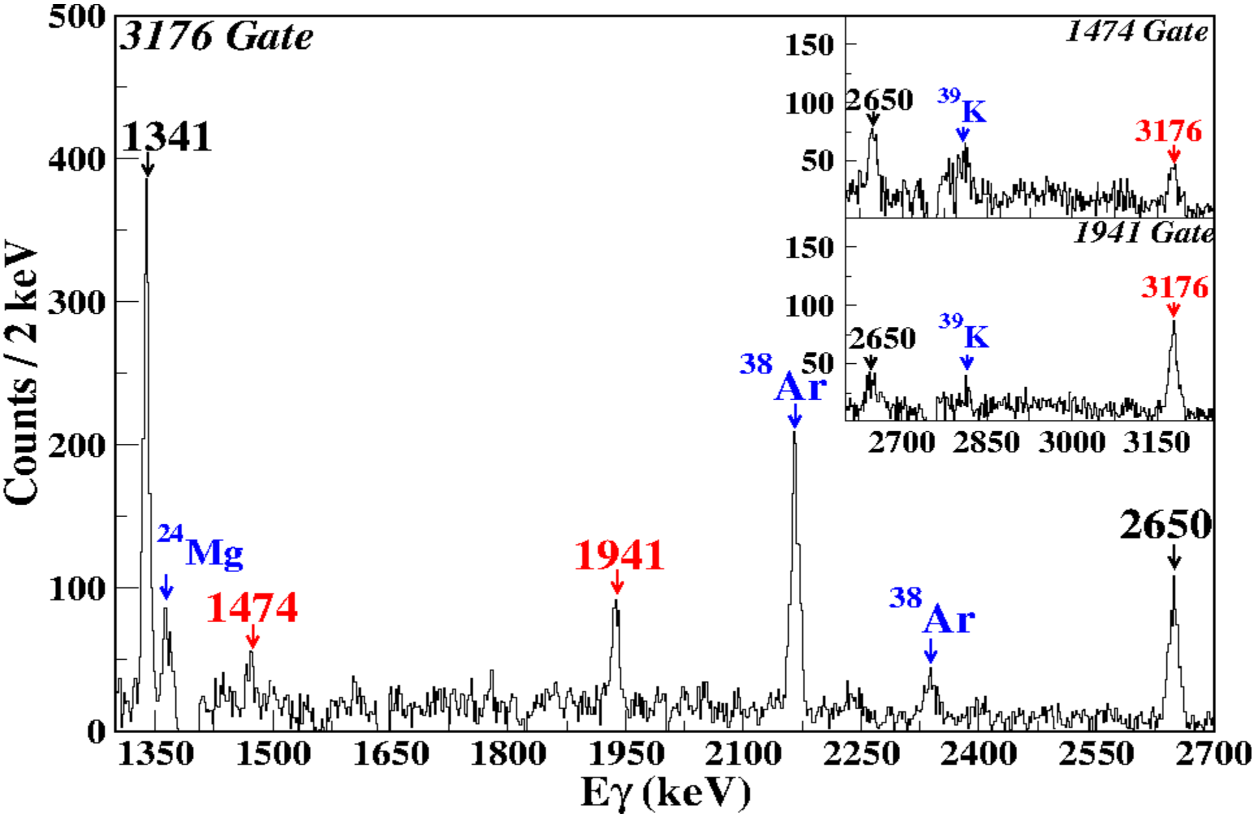

Figure 3.16: Spectrum taken from a gate made on the 3176-keV γ transition, showing clear coincidence with the newly observed 1473-keV and 1941-keV γ transitions. The two insert spectra are taken from gates on the 1473-keV (top) and 1941-keV (bottom) transitions, proving that the two γ rays are in true coincidence with the 3176-keV γ ray.

In the same manner, the remaining newly observed γ transitions and excited states were discovered and placed. Figure 3.17 shows the resulting new levels and γ transitions. Corresponding to the spectra described above, the newly observed γ transitions and states are denoted using the color red. The thickness of each arrow denotes the relative intensity of each γ transition, normalized to that of the 2650-keV γ ray. Table 3.1 depicts the excited states and their errors. Table 3.2 reports the relative intensity for each γ transition scaled to the 2650-keV transition. Chapter 4 will go into further detail regarding the J^π of each excited state, along with comparisons to Shell Model calculations.

Table 3.1: The observed excited states with their relative J^π assignments as proposed from this experiment, comparison to previously reported excited states [1], and with their γ transitions and relative branching ratios. Note, all values are in units of keV unless specified otherwise.

E_I	J^π	Previously Reported	E_γ	Branching Ratio (%)
2342.5 (17)	$(\frac{7}{2},\frac{9}{2}^-)$	2342.2 (2)	2342.5 (17)	100
2650.1 (12)	$\frac{11}{2}^-$	2651.12 (25)	2649.9 (12)	100 (3)
			308.2 (5)	17.6 (11)
3450.7 (20)	$(\frac{11}{2}\frac{17}{2})^+$	3448 (6)	1108.2 (10)	100
3991.0 (14)	$\frac{13}{2}^+$	3992.0 (4)	1340.6 (8)	100.0 (17)
			540.5 (2)	1.4 (2)
4541.5 (15)	$\frac{15}{2}^+$	4543.1 (4)	550.6 (5)	100
5031 (4)	$(\frac{11}{2}^-,\frac{13}{2}^+)$		1580 (3)	100
5533.4 (20)	$\frac{17}{2}^+$	5535.5 (5)	992.1 (13)	100
5812.4 (21)	$(\frac{15}{2})^+$	5811 (10)	1271.1 (15)	100
7074 (3)			2533 (4)	100 (9)
			1540.2 (19)	42 (6)
7383 (4)			2841 (4)	100
8289 (8)			2756 (7)	100
8359 (4)			2826 (3)	100
8709 (3)			3176.0 (20)	100
9185 (4)			3651 (3)	100
10183 (6)			1474 (5)	100
10650 (6)			1941 (5)	100

3.3 *DCO* Calculations

Directional Correlation of Oriented nuclei (*DCO*) ratios provide an experimental way to help put constraints on the spin and parity of an excited state. The *DCO* ratio is a ratio of counts between two transitions, γ_1 and γ_2. The ratio is calculated by taking the ratio of counts of γ_1 at 35° or 145° gated by γ_2 at 90° to the counts in γ_1 at 90° gated by γ_2 at 35° or 145°. To obtain

Table 3.2: The observed γ transitions and their relative intensities as observed in this reaction.

E_γ (keV)	I_γ(%)
308.2 (5)	10
540.5 (2)	3
550.6 (5)	73
992.1 (13)	26
1108.2 (10)	12
1271.1 (15)	4
1340.6 (8)	84
1474 (5)	1
1540.2 (19)	2
1580 (3)	2
1941 (5)	2
2342.5 (17)	26
2533 (4)	2
2649.9 (12)	100
2756 (7)	1
2826 (3)	5
2841 (4)	2
3176.0 (20)	12
3651 (3)	4

the ratios, a special square matrix must first be generated. For this study, all detectors placed at 35 and 145° are added to one axis, the x-axis, while the detectors placed at 90° are added to the y-axis. Placing the different angled detectors on opposite axes allow for projections to be made on the opposite axis, meaning that a gate can be selected around a γ ray from the x-axis, projected onto the y-axis, ultimately showing the data taken from the 90° angled detectors. The reverse projection can also be made, with a gate on the y-axis projecting onto the x-axis, in order to obtain the counts collected by the 35° and 145° angled detectors. Once these counts are obtained for both the 90° and 35° and 145° detectors, the *DCO* ratio is taken such that

$$DCO = \frac{\gamma_1 \text{ Counts from } 35^\circ \text{ and } 145^\circ \text{ gated by } \gamma_2 \text{ at } 90^\circ}{\gamma_1 \text{ Counts from } 90^\circ \text{ gated by } \gamma_2 \text{ at } 35^\circ \text{ and } 145^\circ} \tag{3.1}$$

The ratio then can give insight as to the type of transitions that are in question. The results for various γ transitions, as seen in Figure 3.17, are shown in Figures 3.18 and 3.19. Table 3.3 defines the various types of transitions and the use of *DCO* calculations will be further discussed in Chapter 4.

Table 3.3: Types of γ transitions possible depending on the change of spin and parity from the starting excited state to the final state.

Radiation Type	Name	l	$\Delta\pi$
E1	Electric Dipole	1	yes
M1	Magnetic Dipole	1	no
E2	Electric Quadrupole	2	no
M2	Magnetic Quadrupole	2	yes

Table 3.4: Depending on the transition type of the gated γ, the *DCO* ratio of γ_1/γ_2 can help predict the transition type of of γ_1.

Gated γ Transition Type	DCO Ratio	2nd γ Transition Type
Quadrupole	0.5	Dipole
	1	Quadrupole
Dipole	2	Quadrupole
	1	Dipole

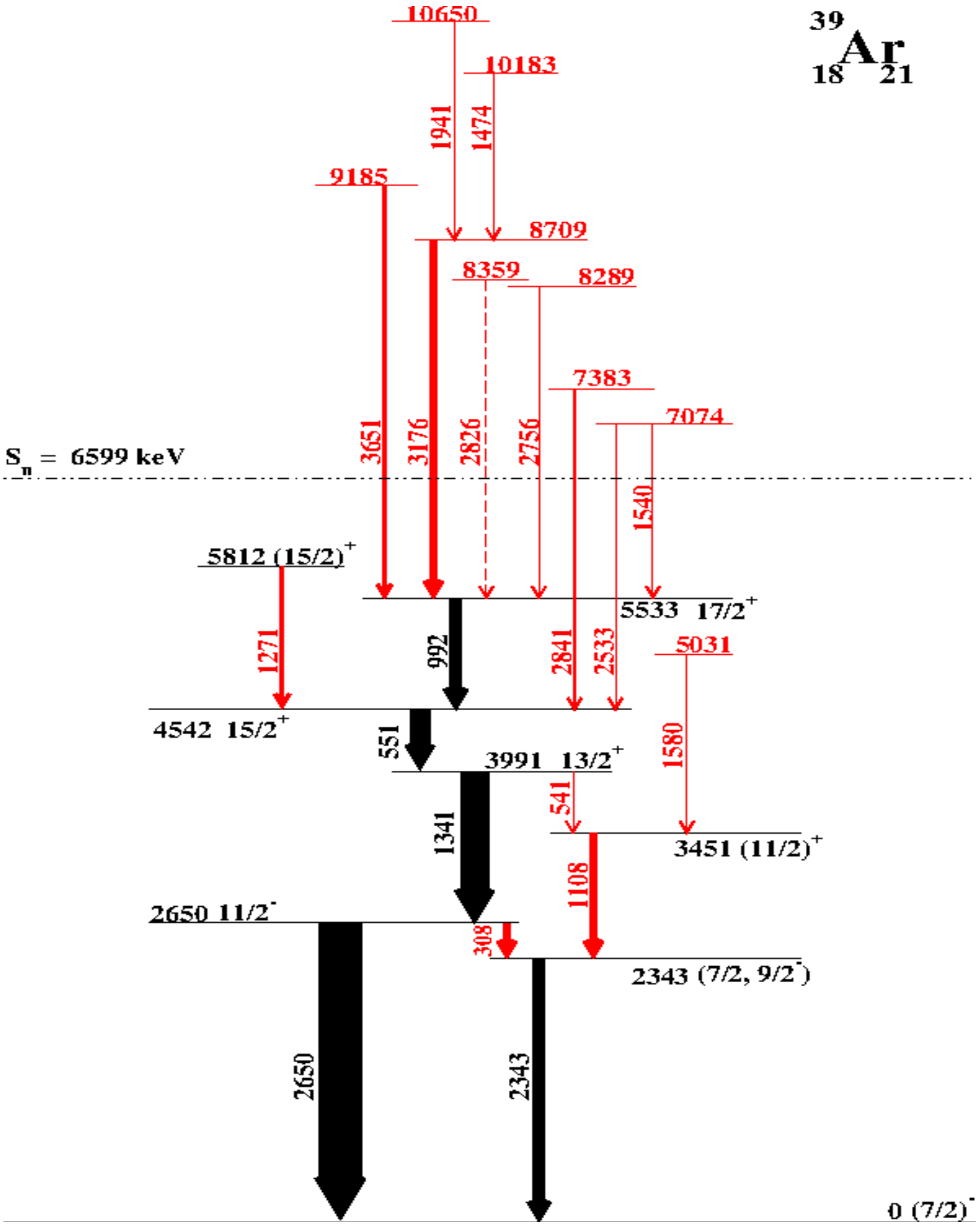

Figure 3.17: Partial level scheme of ^{39}Ar showing newly observed γ transitions and excited states in red and previously reported transitions and states in black. The thickness of the lines denotes the relative intensity of the γ transitions, normalized to the 2650-keV γ ray. This level scheme shows clearly the building of the yrast sequence, along with other high-spin states that sit well above the neutron separation energy (S$_n$). Assigned J$^\pi$ values for each excited state are also included.

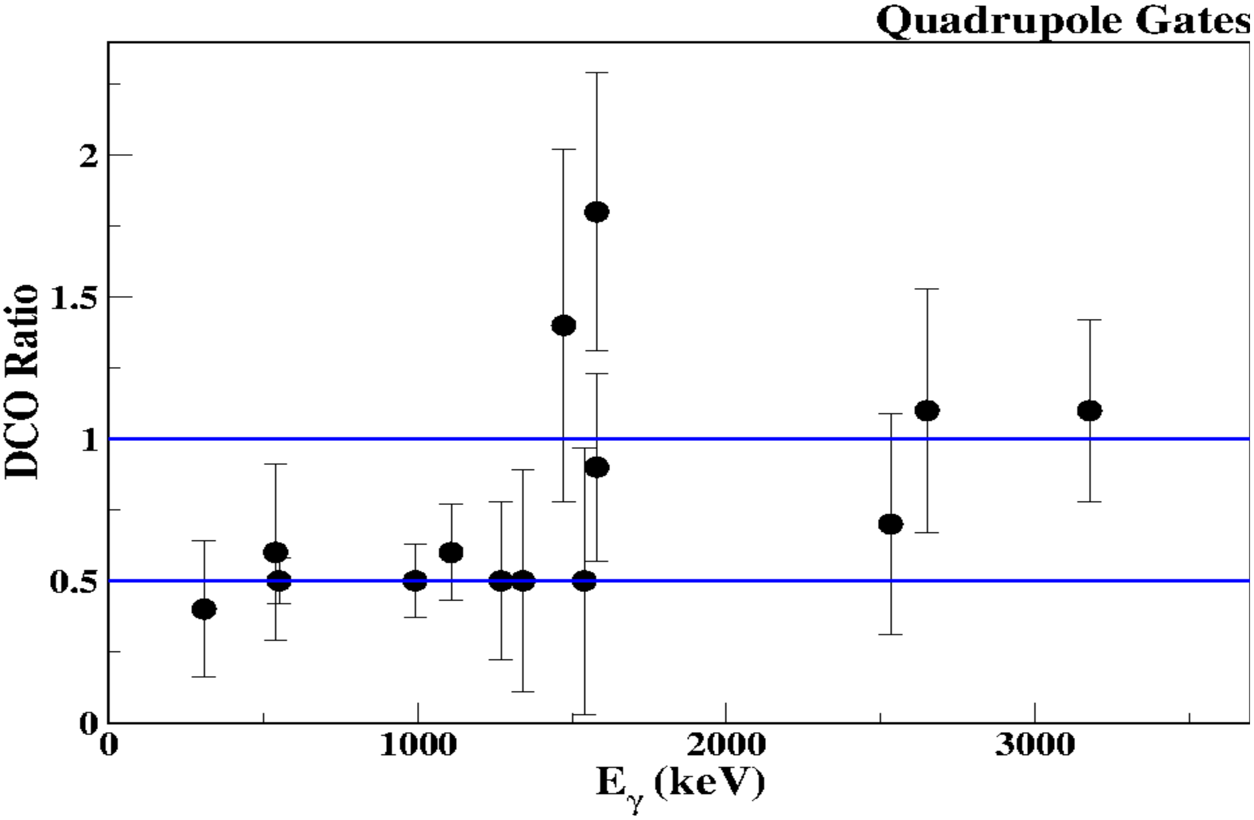

Figure 3.18: The *DCO* ratios as calculated by gating on quadrupole transitions.

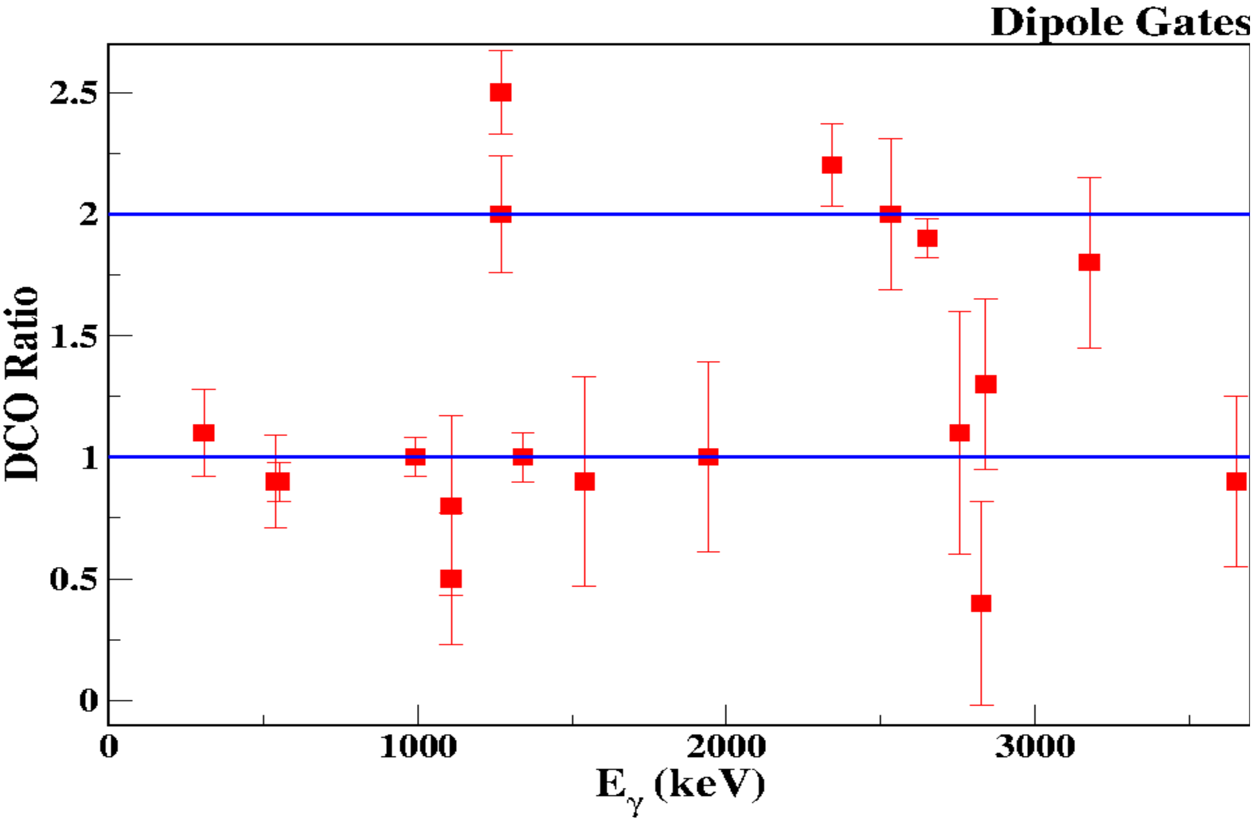

Figure 3.19: The experimentally calculated *DCO* ratios obtained when gating on dipole transitions.

CHAPTER 4

HIGH-SPIN TAKES ON THE SHELL MODEL

4.1 High Spin with the (α,d) Reaction

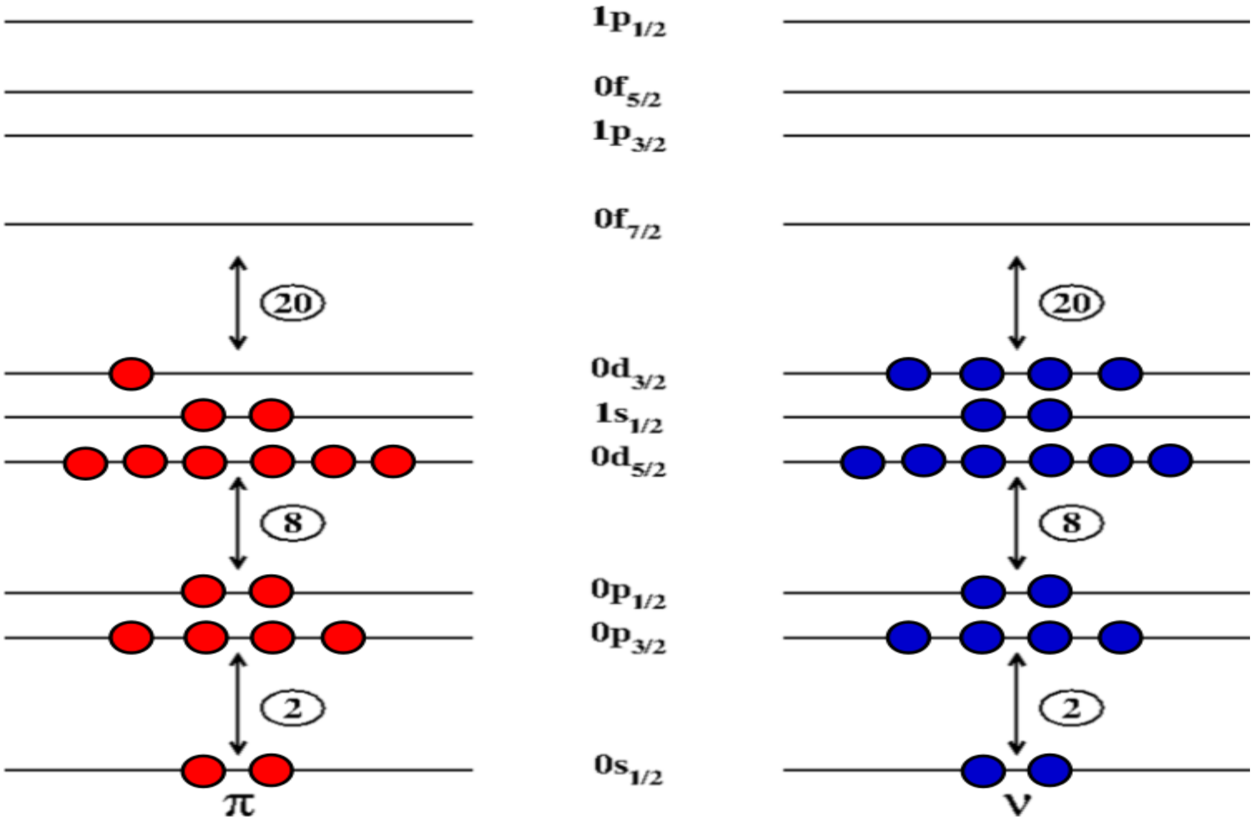

Figure 4.1: Schematic of the shell structure for ^{37}Cl, Z = 17 and N = 20. The proton shells are labeled as π, where as the neutron shells are labeled with ν.

The behavior of the fusion-evaporation reaction and the benefits of using this type of reaction were described in Chapter 2. The different types of reactions all have their own benefits, including the capability to produce excited states with different spin properties. For example, a (d,p) transfer reaction, where a neutron is dropped into a nucleus, is one of the reaction types that tends to favor the creation of excited states with relatively low spin. Conversely, an (α,d) transfer reaction tends to favor the creation of high-spin excited states. Since (α,d) reactions favor the creation of states with high spin, results from experiments utilizing this process can be compared to the results obtained through this current experiment done with the fusion-evaporation reaction.

A prime example of an (α,d) transfer reaction that can be used to compare results with is the reaction ^{37}Cl(α,d)^{39}Ar. Here, a proton and a neutron can be transferred to the ground state of ^{37}Cl. ^{37}Cl, Z = 17 and N = 20, has three vacant spots for the proton to be placed in the sd-shell but no room for the neutron: the neutron will have to be placed in the 0f$_{7/2}$ orbital in the fp-shell or higher (see Figure 4.1). The placement of the proton in the sd-shell and the neutron in the fp-shell gives rise to the structure of the ground state for ^{39}Ar, as shown in Figure 1.2, with a J$^{\pi}$ of 7/2^{-}. This is the simplest case for this (α,d) reaction. Excited states can be formed if the transferred proton is coupled to a different spin in the 0d$_{3/2}$ orbital or is placed in the fp-shell, while the neutron might be placed in other fp orbitals. The rearrangement of the transfrred nucleons allows for different states in ^{39}Ar to be created. If the proton and neutron are both placed in the 0f$_{7/2}$ orbital, their spins can be coupled to spins ranging from 0 to 7$\hbar$. The latter is the fully aligned configuration leading to a spin of 17/2^{+} because of the following configuration: [$\nu 7/2^{-} \bigotimes \pi 7/2^{-} \bigotimes \pi 3/2^{+}$]. Both Refs. [20, 21] used the ^{37}Cl(α,d)^{39}Ar reaction and have reported high-spin states leading up to the fully aligned state at 5.54 MeV. Further examination of this state and the excited state at 5812 keV will be explored in a later section when comparing the (α,d) results to shell model results.

4.2 FSU Shell Model Interaction

In Chapter 1 the basics of the Shell Model were explained, along with the fact that different regions of the Chart of Nuclei typically have different interactions that are utilized to model the region. For the sd- and fp-shell nuclei, our group has used the WBP-a [37] or PSDPF [38] interactions for nuclei with one nucleon in the fp-shell. Each interaction was determined by varying the single particle and cross-shell parameters in order to try and find the best fit for nuclei in the region of interest. Recently, at FSU, a new interaction was developed taking the basis of WBP (USDB and GXPF1A) and modifying it to span 30 sd-shell isotopes ranging from ^{23}Ne to ^{39}K [39]. A comparison of calculations using the three different interactions for the low-lying excited states seen in this experiment (see Figure 3.7) are shown in Tables 4.1 and 4.2. Table 4.1 shows the negative parity, zero-particle-zero-hole (0p-0h) states, which are obtained through the rearrangement

Table 4.1: Comparisons for 0p-0h states using three different interactions. Each result is matched to the experimental states with tentative J^π assignments as seen in this experiment. The Root Mean Square (RMS) deviation are calculated for each interaction.

FSU Int.		**WBP-a**	**PSDPF**	**Exp**	
Ex	J^π	Ex	Ex	Ex	J^π
0	$7/2^-$	0	0	0	$7/2^-$
1335	$3/2^-$	528	1761	1267	$3/2^-$
2031	$9/2^-$	2054	2140	2343	$(5/2^-,7/2,9/2^-)$
2065	$5/2^-$	1950	2208	2091	$5/2^-$
2326	$3/2^-$	2096	2465	2433	$3/2^-$
2373	$7/2^-$	2150	2623	2481	$7/2^-$
2391	$11/2^-$	2492	2681	2650	$11/2^-$
2673	$1/2^-$	2194	2771		
3402	$5/2^-$	2526	3476	2755	$5/2^-$
3416	$7/2^-$	2660	3485		
3622	$3/2^-$	2709	3941		
3946	$9/2^-$	3961	3675		
3973	$1/2^-$	3661	4422		
4348	$7/2^-$	4229	4071		
4485	$5/2^-$	4343	4361		
4511	$11/2^-$	8364	4149		
RMS=261		**RMS**=220	**RMS**=297		

of the protons within the sd-shell or the neutron moving in various orbitals within the fp-shell with particular magnetic substates. Table 4.2 shows the positive parity, one-particle-one-hole (1p-1h) states which are obtained through the promotion of a nucleon across the shell gap into the fp-shell. The Root Mean Square (RMS) values can be found under the respective interaction in each table. The remaining discussion will focus on the use of the FSU interaction.

4.2.1 The Matching Game

A great way to initially test how well an interaction is reproducing the experimental results is to compare the two results of known states. In ^{39}Ar, the first four high-spin states that make up the yrast sequence are perfect for comparing. With the interaction of choice being the FSU interaction, comparison of these four states to the theory calculated states are shown in Figure 4.2.

The FSU interaction is able to reproduce the four yrast sequence states with an RMS of 306, showing that this interaction is capable of reproducing the high-spin states of ^{39}Ar. Figure 4.3

Table 4.2: Interaction comparisons for 1p-1h states. Each interaction is matched to the experimental states with tentative J^π assignments as seen in this reaction. The Root Mean Square (RMS) are calculated for each interaction.

FSU Int.		**WBP-a**	**PSDPF**	**Exp**	
Ex	J^π	Ex	Ex	Ex	J^π
1570	$3/2^+$	1755	1343	1517	$3/2^+$
2235	$1/2^+$	2839	1928	2358	$1/2^+$
2545	$1/2^+$	3843	3075	2829	$1/2^+$
2546	$5/2^+$	3198	2745	2503	$(5/2)^+$
2719	$7/2^+$	2993	2494	2523	$(5/2^-,7/2,9/2^-)$
2914	$3/2^+$	3434	3071	2949	$(3/2^+,5/2)$
3313	$3/2^+$	4019	3881	3381	$3/2^+,5/2^+$
3432	$11/2^+$	4039	3773	3451	$(11/2:17/2)^+$
3542	$9/2^+$	4098	3798		
3593	$7/2^+$	4268	3811		
3689	$5/2^+$	4136	3581	3360	$5/2^+$
3845	$3/2^+$	4434	4132	3381	$3/2^+,5/2^+$
3849	$5/2^+$	4713	4045	4473	$3/2^+,5/2^+$
3973	$11/2^+$	4687	3921	3448	$(11/2:17/2)^+$
4061	$1/2^+$	4673	4362		
4137	$5/2^+$		4452	3890	$(5/2)^+$
4175	$7/2^+$	4365	3829		
4186	$13/2^+$	4784	4259	3991	$(13/2)^+$
4244	$3/2^+$		4562	4530	$(3/2)^+$
4332	$11/2^+$		4894	4927	$(11/2,13/2)^+$
4561	$15/2^+$	5163	4662	4542	$(15/2)^+$
5014	$17/2^+$	6538	6532	5533	$(17/2)^+$
5736	$15/2^+$	6552	5741	5812	$(13/2:17/2)^+$
RMS=291		**RMS**=643	**RMS**=355		

shows the comparison of *all* the high-spin states relative to the Shell Model calculated states. Further examination of the comparison shows that each experimental high-spin state has a theoretically calculated candidate. The relative J^π values associated with each match are all in good agreement with observed decay patterns, along with calculated *DCO* ratios. Notice that beyond the experimental state at 2650 keV no further high-spin negative parity states have been observed. The FSU interaction also shows this as well, with the first $13/2^-$ state located at 8.4 MeV. This shows that it is more energetically favorable to promote a nucleon across the shell gap, rather than recouple the protons in the sd-shell to a spin greater than $2\hbar$.

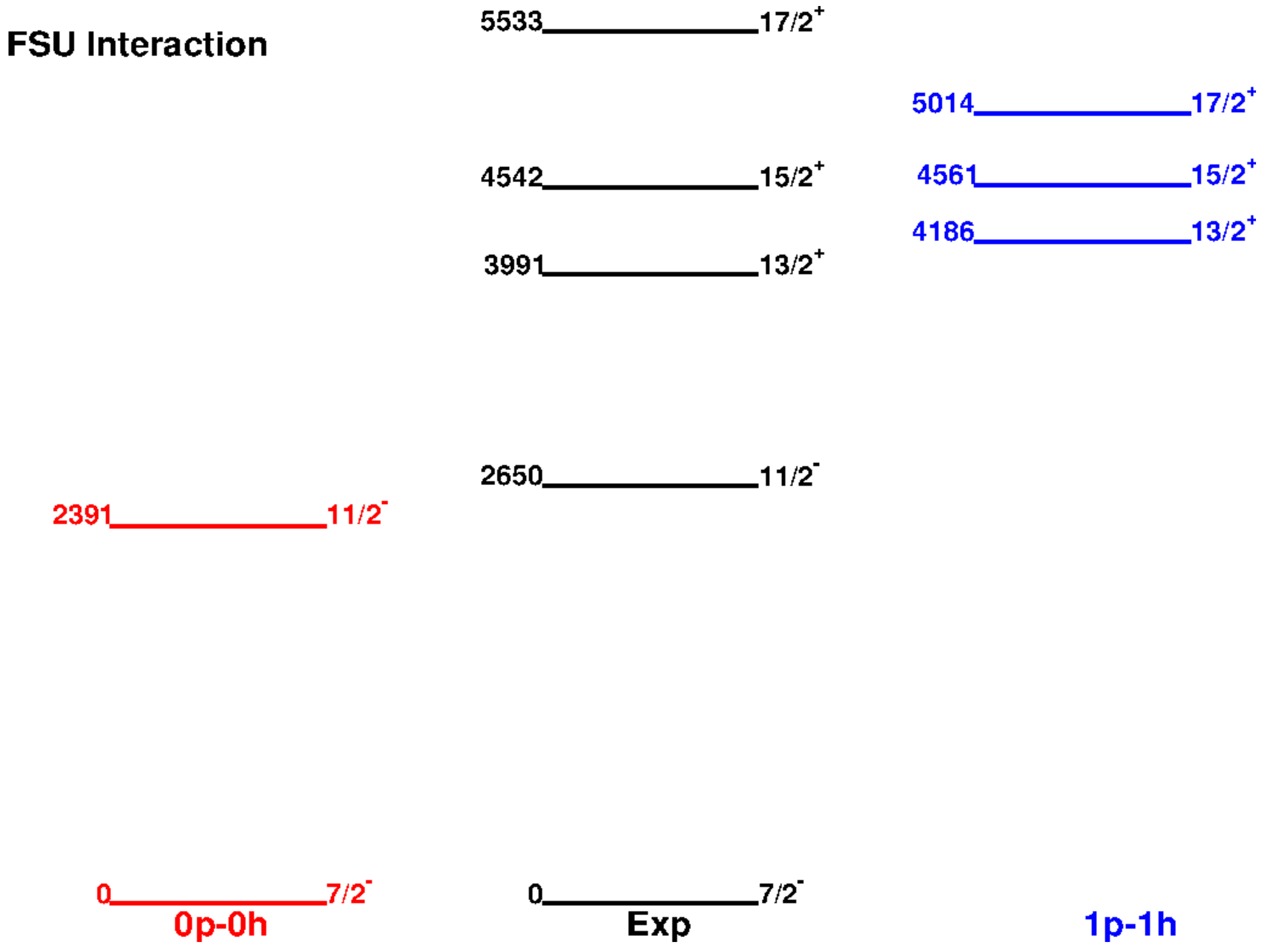

Figure 4.2: The calculated theory states using the FSU interaction were compared to the first four high-spin states with previously assigned J$^\pi$. The comparison of the four states give an RMS of 306.1, indicating that FSU is capable of reproducing the known high-spin states in ^{39}Ar. Further comparison to the remaining high-spin states will be made in Figure 4.3.

4.2.2 Occupancies

The majority of the pairing of experimental states and theory states are done through the use of γ decay patterns, such as the fact that in a fusion-evaporation reaction, γ rays will have a tendency to decay from a state of higher spin to a state with lower spin. The use of *DCO* ratios also played a role in determining whether or not the change in spin was an $l = 1$ or an $l = 2$ transition. The occupancy of a state can be theoretically calculated and can help give insight as to where the nucleons are in order to create that excited state. This becomes useful when comparing a state such

Table 4.3: The calculated occupancies for the high-spin states with previous tentative J^π assignments. The occupancies can be used to compare to states observed in the ^{37}Cl(α,d) reaction, along with give insights as to the general structure of the sd- and fp-shells as nucleons are promoted across the shell gap.

Energy (keV)	J^π		Occupancy $\mathbf{0f}_{7/2}$	$\mathbf{1p}_{3/2}$	$\mathbf{0f}_{5/2}$	$\mathbf{1p}_{1/2}$
4186	$13/2^+$	Z	0.232	0.002	0.008	0.001
		N	1.702	0.035	0.018	0.002
4561	$15/2^+$	Z	0.182	0.001	0.010	0.000
		N	1.759	0.031	0.017	0.001
5014	$17/2^+$	Z	0.877	0.000	0.008	0.000
		N	1.101	0.001	0.012	0.000
5736	$15/2^+$	Z	0.459	0.005	0.012	0.003
		N	1.474	0.015	0.028	0.004

as the $17/2^+$ excited state at 5533 keV to the same state as created in the ^{37}Cl(α,d)^{39}Ar reaction. In the (α,d) reaction, it is very likely the 5533 keV is produced by placing a proton in the $0f_{7/2}$ orbital, along with a neutron also in the $0f_{7/2}$ orbital, as explained above. This state is the fully aligned or fully stretched state and would look similar to a theory state with an occupancy number close to one for both the proton and neutron in $0f_{7/2}$. If such a theory state exists, it will most likely correspond to the excited state with a $J^\pi = 17/2^+$.

Table 4.3 shows the occupancies for the first $17/2^+$ state as calculated using the FSU interaction. Notice that the $0f_{7/2}$ orbital is composed of nearly half neutrons and half protons, meaning that it contains one proton and one neutron. Prior to that, the majority of the 1p-1h states are created through the promotion of a neutron rather than a proton, as can be seen in Table 4.5. The promotion of a neutron instead of a proton is more energetically favorable due to the fact that, even though a neutron pair is broken in the $0d_{3/2}$ orbital, a neutron pair is created in the $0f_{7/2}$ orbital. If the proton were instead promoted, a pair would be broken and both protons would remain unpaired. However, the highest J^π obtainable through the promotion of a neutron is $15/2^+$, by $\nu[7/2 \bigotimes 5/2 \bigotimes 3/2]^+$ and $(-1)^{l=2}$ for the unpaired neutron in the $0d_{3/2}$ orbital. This state is also shown in Table 4.3 as the first $15/2^+$ state, with the $0f_{7/2}$ orbital composed of approximately 74% extra neutron and 23% proton. The $17/2^+$ state with approximately equal distribution of

Table 4.4: The calculated occupancies of the first 11 0p-0h states as calculated using the FSU interaction. The occupancies show that the majority of excited states are created by changing the magnetic substate of the neutron in the $0f_{7/2}$ orbital, with the exception of the the first $3/2^-$, and the cluster of states at 3 MeV. The 3416 is indicative of the magnetic substate change relative to the original substate in the theory state at 3402 keV.

		Occupancy			
Energy (keV)	J^π	$\mathbf{0f_{7/2}}$	$\mathbf{1p_{3/2}}$	$\mathbf{0f_{5/2}}$	$\mathbf{1p_{1/2}}$
0	$7/2^-$	0.992	0.007	0.001	0.000
1335	$3/2^-$	0.228	0.764	0.000	0.008
2031	$9/2^-$	0.999	0.000	0.001	0.000
2065	$5/2^-$	0.950	0.044	0.004	0.001
2326	$3/2^-$	0.766	0.227	0.001	0.005
2373	$7/2^-$	0.888	0.110	0.002	0.000
2391	$11/2^-$	1.000	0.000	0.000	0.000
2673	$1/2^-$	0.000	0.390	0.001	0.608
3402	$5/2^-$	0.189	0.799	0.001	0.011
3416	$7/2^-$	0.324	0.674	0.001	0.001
3622	$3/2^-$	0.058	0.926	0.001	0.015

neutrons and protons is indicative of the fully stretched state seen in the (α,d) reaction, further concreting the fact that the excited state at 5533 keV is in fact a $J^\pi = 17/2^+$ state. Additionally, Ref. [20, 21] both show a smaller, but still strong, peak to the left of the 5.54 MeV peak at 5.81 MeV. This state corresponds to the 5812 keV state as seen in the current experiment and is simply the $17/2^+$ state with reconfigured magnetic spin states. This becomes apparent when observing the occupancies for the second $15/2^+$ state as shown in Table 4.3. Notice that the $15/2^+$ state no longer shows an almost equal distribution of protons and neutrons in the $0f_{7/2}$ orbital, but still shows a significant contribution from a promoted proton comparatively to the first excited $15/2^+$ state with almost no proton contribution in the $0f_{7/2}$ orbital.

The theoretically calculated occupancies are also useful to try and understand how the nuclear structure changes as the nucleons move about within the various shells; little things such as the observation of the excited 0p-0h state at 2391 keV with a $J^\pi = 11/2^-$. For this state, the neutron is 100% in the $0f_{7/2}$ with no other contribution from the other fp orbitals unlike the surrounding states. Even the ground state with a $J^\pi = 7/2^-$ has a 99% contribution from the $0f_{7/2}$ orbital and a 0.07% contribution from the $1p_{3/2}$ orbital. The reason that the $11/2^-$ state has 100% contribution from the $0f_{7/2}$ is because there is no possible way to obtain a J^π of $11/2^-$ if the neutron is in the

$1p_{3/2}$ orbital. Observations such as this or the fact that up until the first $17/2^+$ state neutrons are predominately promoted across the shell gap allow for the structure of the shells (sd and fp) to be more thoroughly understood, ultimately allowing for interactions to be modified to fit a larger span of isotopes.

Table 4.5: The calculated occupancies for the first nine 1p-1h states as calculated using the FSU interaction. The occupancies show that for the majority of the 1p-1h states, a neutron is promoted across the shell gap rather than a proton. This shows that it is more energetically favorable to break the neutron pair in the $0d_{3/2}$ orbital and create a pair in the $0f_{7/2}$ orbital. This configuration is capable of creating a J^{π} up to $15/2^+$. All spin values greater than 15/2 requires the promotion of a proton across the shell gap.

Energy (keV)	J^{π}		Occupancy $\mathbf{0f}_{7/2}$	$\mathbf{1p}_{3/2}$	$\mathbf{0f}_{5/2}$	$\mathbf{1p}_{1/2}$
1570	$3/2^+$	Z	0.048	0.003	0.004	0.001
		N	1.778	0.140	0.014	0.013
2235	$1/2^+$	Z	0.038	0.002	0.003	0.001
		N	1.842	0.097	0.009	0.008
2545	$1/2^+$	Z	0.208	0.012	0.017	0.003
		N	1.688	0.046	0.021	0.006
2546	$5/2^+$	Z	0.094	0.001	0.007	0.000
		N	1.745	0.132	0.015	0.005
2719	$7/2^+$	Z	0.103	0.007	0.006	0.002
		N	1.756	0.105	0.014	0.006
2914	$3/2^+$	Z	0.248	0.021	0.013	0.006
		N	1.606	0.072	0.025	0.008
3313	$3/2^+$	Z	0.325	0.019	0.010	0.005
		N	1.363	0.246	0.016	0.014
3432	$11/2^+$	Z	0.402	0.012	0.016	0.005
		N	1.490	0.036	0.030	0.006
3542	$9/2^+$	Z	0.146	0.004	0.009	0.002
		N	1.779	0.034	0.021	0.005

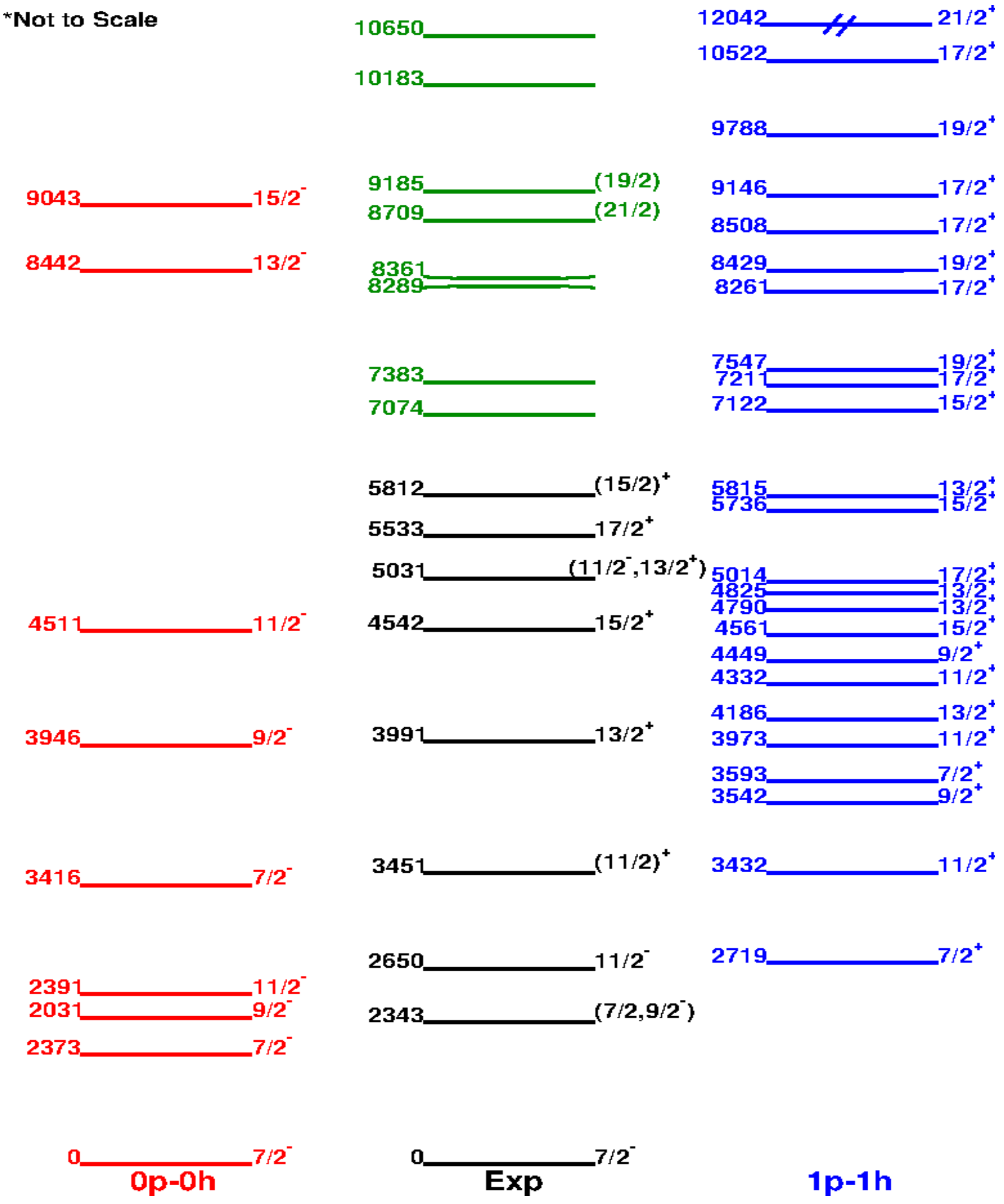

Figure 4.3: A full comparison of the FSU interaction calculated states to the high-spin states as seen in this reaction. All experimental states have a theoretical state match that fits well with decay patterns and *DCO* ratios.

CHAPTER 5

BETA DECAY OF EXOTIC NUCLEI AT THE NSCL

5.1 Beta Decay

Fusion-evaporation reactions, as described in Chapter 2, are one of the more common ways to create nuclei in excited states that can be studied with the use of γ spectroscopy. The fusion of stable beams and particles cannot create nuclei that are very far from stability and thus, these exotic nuclei require a different process in order to create them. Fragmentation of stable beams at higher energies is capable of producing a small fraction of these more exotic nuclei. γ spectroscopy can then be used to study the beta (β) decay daughters that are created during the process. β decay is the process of a neutron decaying into a proton or vise versa. When a nucleus undergoes β decay, it moves closer to stability and thus becomes more energetically favorable as the imbalance between protons and neutrons decreases. If a proton is converted into a neutron, the process is called β^+ decay, likewise, if a neutron is converted to a proton, the decay is denoted as β^-. For the purpose of this study, β^- decays will be the main focus.

During β^- decay, a neutron in a nucleus transforms into a proton and an [undetected] anti-neutrino is emitted. The reaction looks as such:

$$^{A}_{Z}X \longrightarrow ^{A}_{Z+1} Y + \beta^- + \bar{\nu} \tag{5.1}$$

with $^{A}_{Z}X$ being the parent nucleus undergoing the β^- decay and $^{A}_{Z+1}Y$ being the resulting daughter nucleus. β^- decay can leave the daughter nucleus in any number of states, including the ground state, if allowed by energy conservation and spin-parity change rules as shown in Table 5.1. If the β^- decay leaves the daughter nucleus in an excited state below the neutron-separation energy, S_n, then the state will decay through the emission of γ rays. However, if the daughter nucleus is left in an excited state above the S_n, then the mode of decay will be through the emission of a neutron and will create the β^--n daughter, $^{A-1}_{Z+1}Z$. This process is shown in Equation 5.2. Once the β^- daughter or β^--n daughter nucleus has decayed down to the ground state, it can then also β^-

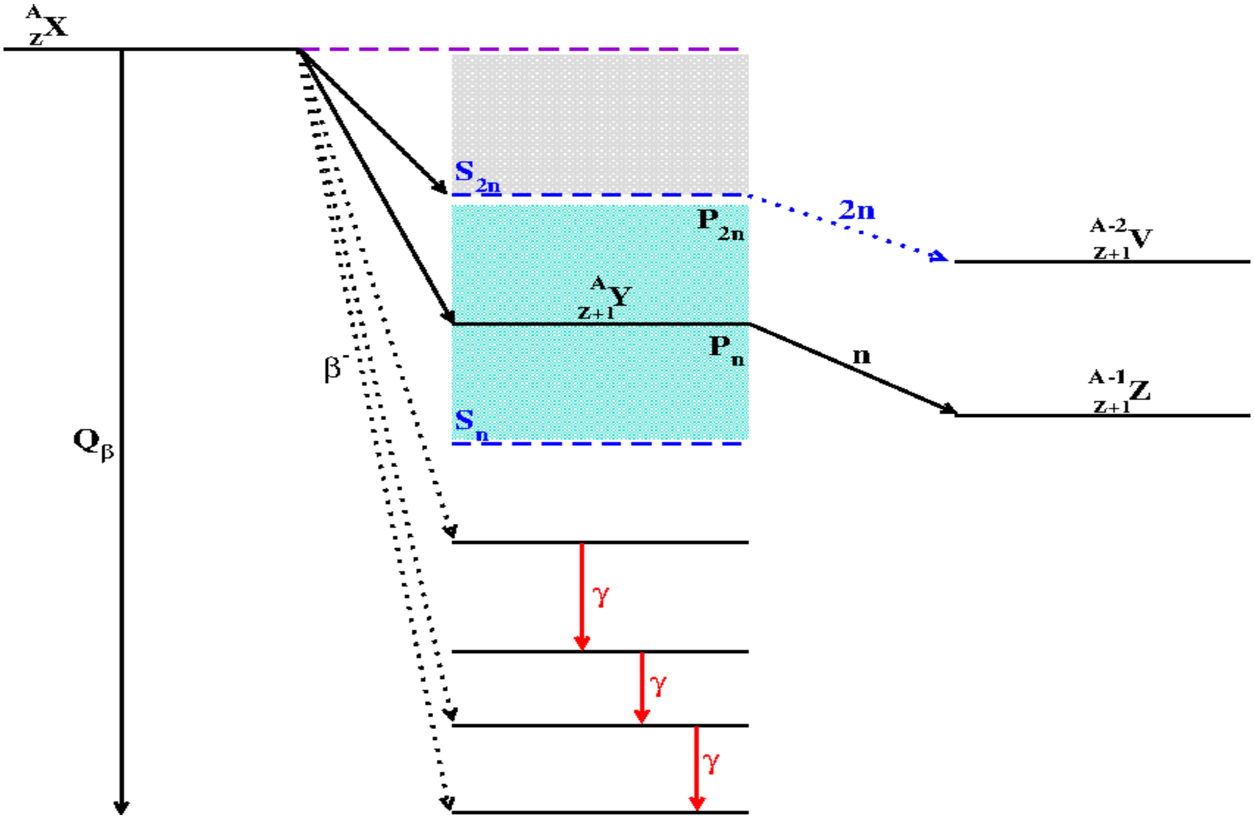

Figure 5.1: A schematic of a β^- decay followed by γ-ray or neutron emissions. P_n and P_{2n} are the probabilities that one or two neutrons will be emitted after the β^- decay.

decay, creating $^A_{Z+2}W$, the granddaughter, as shown in Equation 5.3, starting the entire process all over again.

$$^A_{Z+1}Y \longrightarrow ^{A-1}_{Z+1} Z + n \tag{5.2}$$

$$^A_{Z+1}Y \longrightarrow ^A_{Z+2} W + \beta^- + \bar{\nu} \tag{5.3}$$

The emitted γ rays become very important when it comes to understanding the structure of the daughter nucleus. The detection of the γ rays occurring in coincidence with the β^- decay allows for the unveiling of excited states within the nucleus and provides J^π constraints to be placed on said excited states. The constraints are made using selection rules for β^- decay. Table 5.1 is a list of the selection rules.

Table 5.1: β decay rules in terms of change of J$^{\pi}$ and logft [2]

Transition Type	ΔJ	$\Delta\pi$	logft
Superallowed	0	No	2.9 - 3.7
Allowed	0,1	No	$\geq$ 4.4
First Forbidden	0,1,2	Yes	$\geq$ 6
Second Forbidden	1,2,3	No	$\geq$ 10
Third Forbidden	2,3,4	Yes	$\geq$15

The intensities of the observed γ rays allow for branching ratios to be measured for each excited state, which in turn, allows for logft values to be calculated. Logft values, which are a combination of the partial half-life, t, and the Fermi function, determine which excited states are populated during the β^- decay of the parent nucleus to the daughter nucleus. Knowing the logft allows for the decay to be charactorized as "allowed", "forbidden", etc., placing constraints on the J$^{\pi}$ of the state being populated (see Table 5.1). The following equation

$$\frac{1}{ft} = \frac{1}{6147 \pm 7}\left(\frac{g_A}{g_V}\right)^2 B(\mathrm{GT})_{i \longrightarrow f} \tag{5.4}$$

with $\frac{g_A}{g_V} = -1.266$ [2] allows for logft values to be translated into B(GT) values. B(GT) is the reduced transition probability for a Gamow-Teller (GT) transformation [8] and can be used to compare to Shell Model values.

5.2 Experimental Details

Exploration of excited states in ^{39}P produced in the β^- decay of ^{39}Si is goal of this study. With N = 25 and Z = 14, ^{39}Si is an exotic nucleus and requires a facility that is capable of producing radioactive beams for its investigation. One such facility is the National Superconducting Cyclotron Laboratory (NSCL) at Michigan State University. In March of 2015, a five day experiment using the NSCL β Counting System (BCS) [6] was conducted in order to study the γ radiation in ^{39}P following the β decay of ^{39}Si. Approximately 186,000 $\beta - \gamma$ events were recorded.

The BCS is comprised of a thick planar germanium detector, with a radius of 9 cm and a thickness of 1 cm, and the Segmented Germanium Array (SeGA). The planar Ge detector is a double-sided strip detector (GeDSSD) and is electrically segmented into 16 5-mm strips, in both the x and y-directions, with one set of strips on the front of the detector and the other set perpendicular

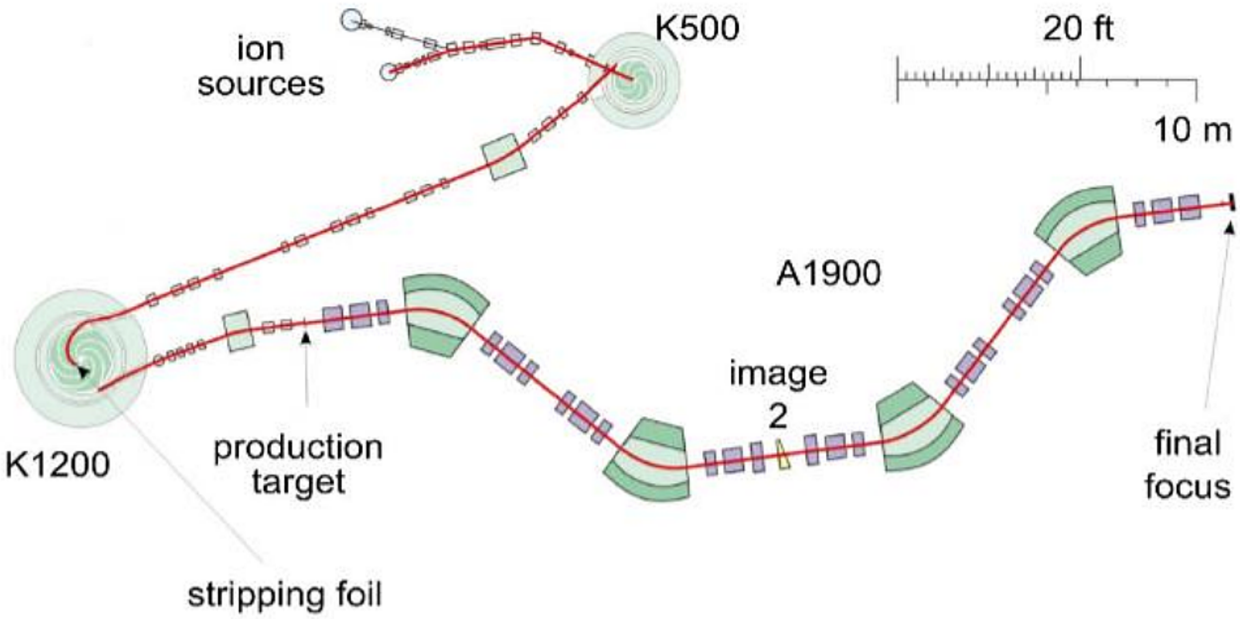

Figure 5.2: Schematic of the NSCL, showing the location of the A1900 Isotope Separator [6].

on the back of the detector, producing a total of 256 individual pixels [40]. SeGA surrounds the GeDSSD and contains 16 HPGe detectors, each individually calibrated using standard sources. Figure 5.3 shows SeGA with the GeDSSD at the heart of the array.

A stable primary beam of ^{48}Ca with an energy of 140 MeV/amu, 80 pnA intensity, was fragmented by impinging on a 795 mg/cm^2 thick ^{9}Be target. The A1900 fragment separator was then used, with 5% momentum acceptance [7], to filter out the rare isotopes that were of interest to the experiment [41]. The emerging cocktail beam was centered about ^{36}Mg consisting of other nearby nuclei such as neon, sodium, aluminum, and silicon isotopes shown in Figure 5.5. The fragments are identified in Z and A, such as in Figure 5.5, which is generated from the energy loss measured in a silicon PIN detector upstream from the experiment and the time-of-flight (TOF) between a scintillator at the dispersive image of the A1900 (labeled "Image 2" in Figure 5.2) and the PIN detector [6].

As the cocktail secondary beam hits the GeDSSD, the rare isotopes are stopped and implanted into the pixels (detecting both the implant and the decay): the implantation rate was kept at a low rate of 100 Hz, to maximize the efficiency of the correlated ion and β^- decay [7]. γ rays that are in coincidence with the β^- particles from a particular implant who's β^- decay occurred to an excited state in the daughter nucleus are detected using SeGA. Figure 5.4 demonstrates this basic concept.

In order to correlate the implantation of a nucleus, with measured Z and N, to the later β^- and γ rays, it is necessary to keep the implantation rate low enough so most of the implants have time to decay before another implant takes place. The segmented detector allows for a rate that is approximately equal to the number of exposed pixels, thus a low rate of 100 Hz was chosen to utilize most of the pixels. The analysis software maintains a table of which isotopes have been implanted into each pixel. The subsequent β^- decay of an implanted isotope within the same pixel are also recorded within a correlation time which is decided based on the half-life of the nuclei of interest. The time-correlated γ rays are then detected using SeGA with high energy resolution. The results of the $\beta^- - \gamma$ coincidences can be found in Chapter 6.

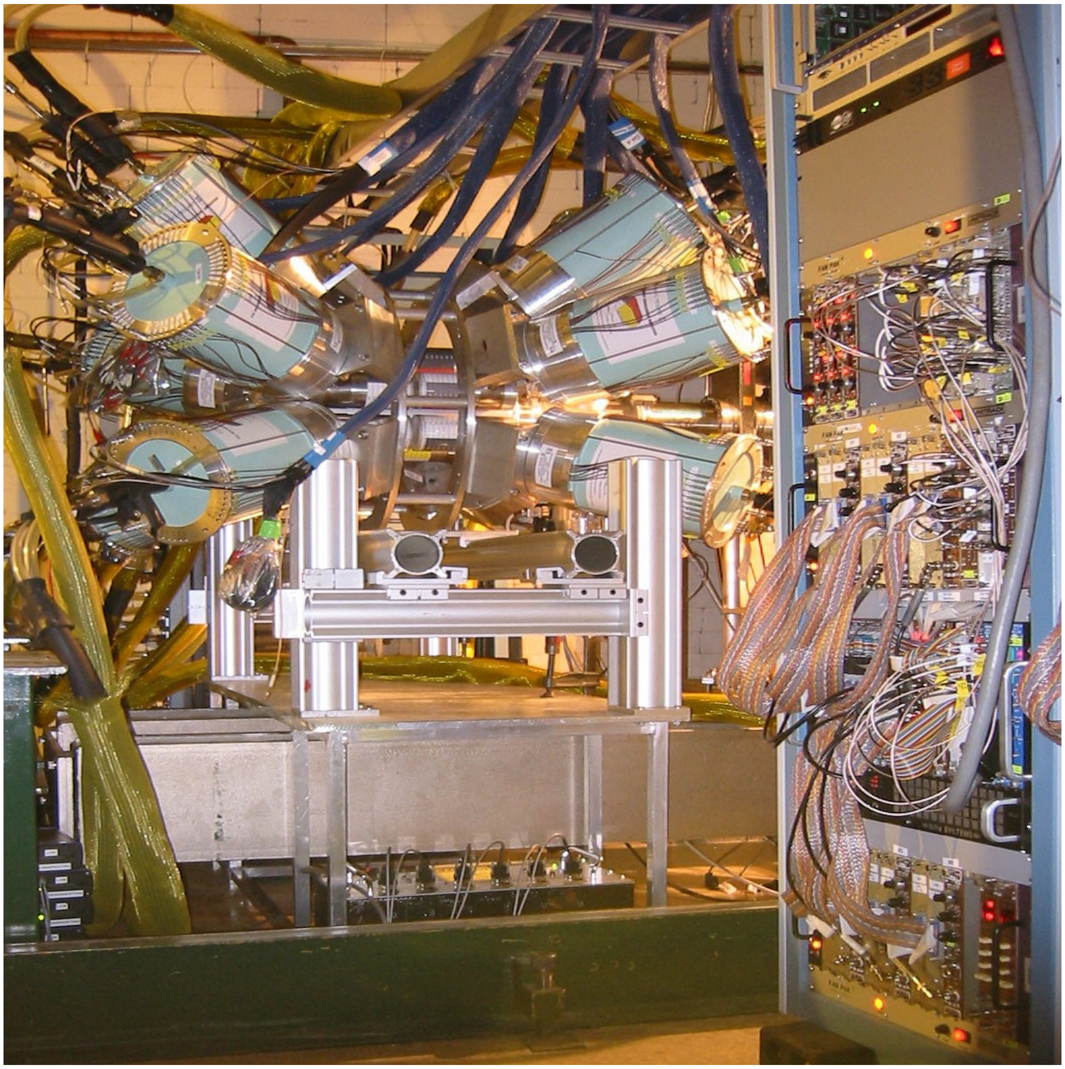

Figure 5.3: The final configuration of SeGA coupled with the GeDSSD.

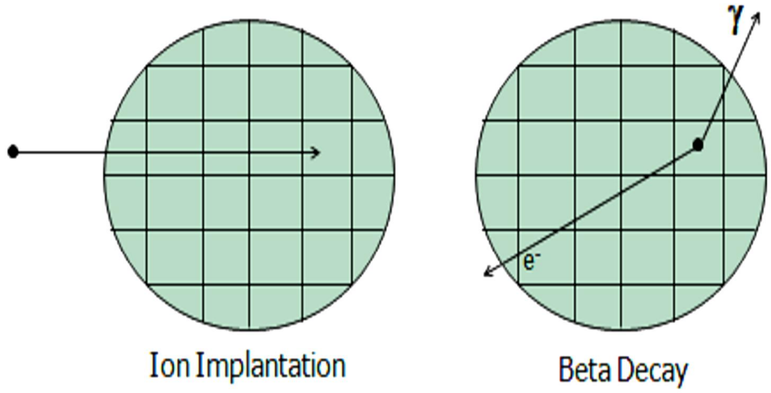

Figure 5.4: A schematic representation of the implantation of an ion followed by the β^- decay of the implanted ion in coincidence with the emission of γ rays.

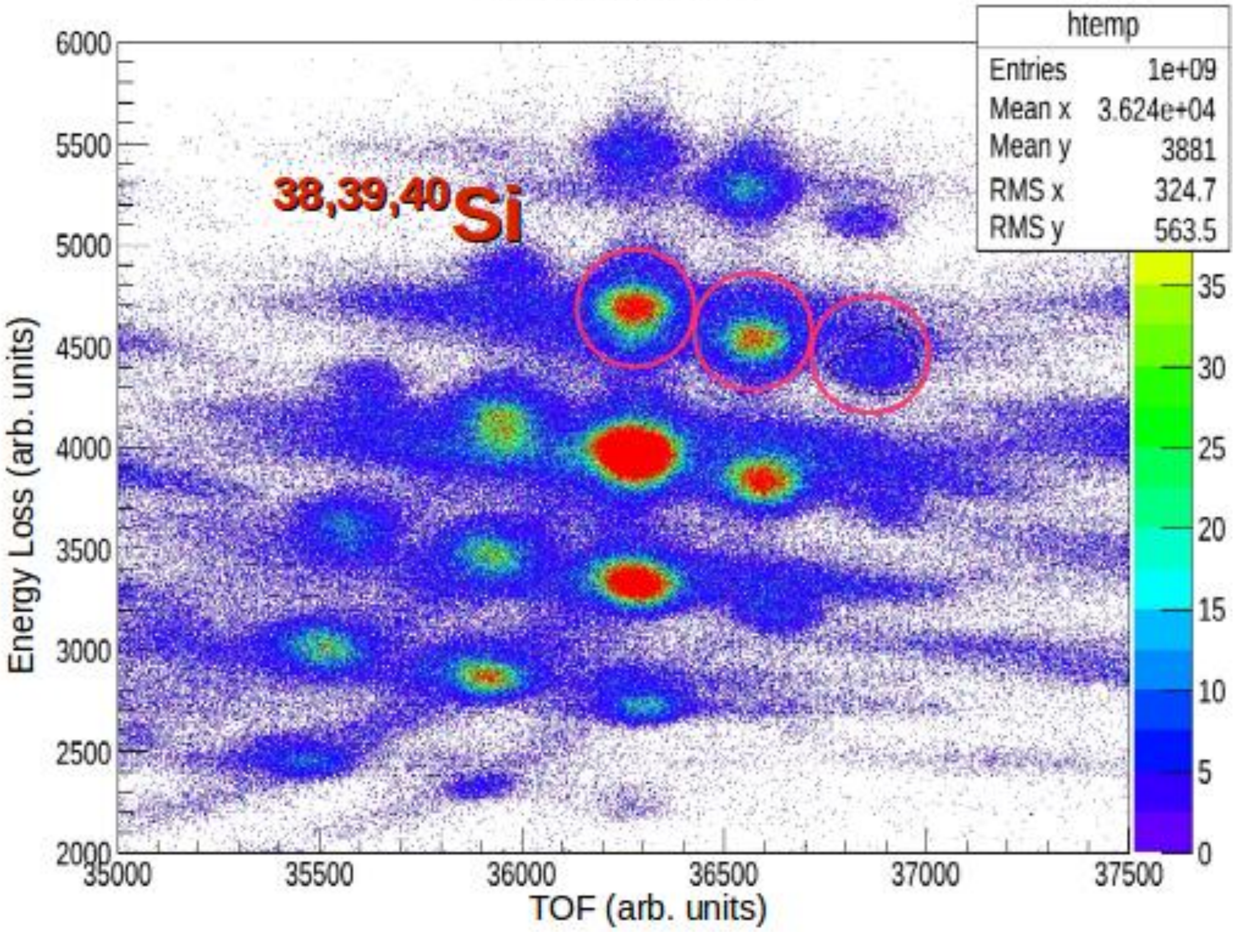

Figure 5.5: With time-of-flight between a scintillator at the A1900 and the PIN detector on the x-axis and energy loss in the PIN detector on the y-axis, the various nuclei produced by the fragmentation of the primary beam can be identified. The three strongest silicon isotopes, circled in red, were selected and gated on with a particular focus on the β^- decay of ^{39}Si.

CHAPTER 6

EXPERIMENTAL RESULTS: ^{37,39}P

β^- decay, as described in the previous chapter, provides a multitude of vital information about the nucleus undergoing the decay. One such piece of information that can be extracted is the half-life of the decaying nucleus. Half-life measurements become important for astrophysical processes and, more importantly, when comparing to theory models, as is the goal of this dissertation. The half-life of a decaying nucleus can be extracted through time correlations of implants and decays, creating a fragment-β correlation curve, or a decay curve. The decay curves are histograms that depict the decaying and creation of isotopes through the decay sequence and can be fitted using the full Bateman equation. The fact that the experiment was done using a cocktail beam allows for several isotopes to be analyized. The β^- decay of ^{37,39}Si into ^{37,39}P will be the primary focus of this discussion: the results for even-A phosphorus isotopes, ^{38,40}P, were published in 2017 [7]. Figures 6.1 and 6.2 show the β^- decay components of the two isotopes of interest. Due to the

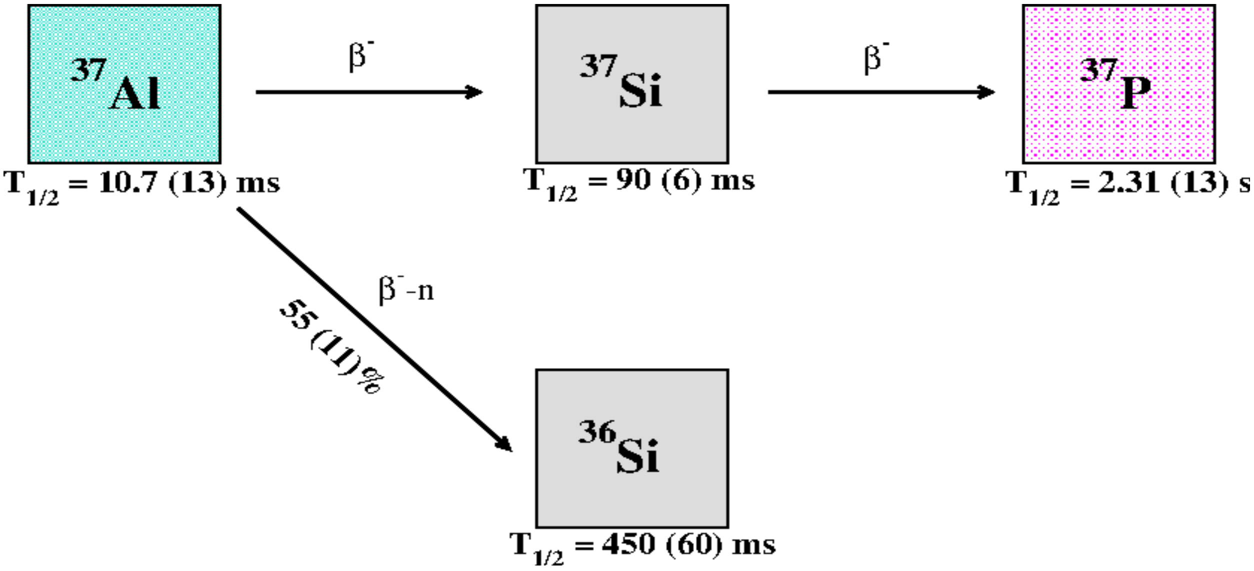

Figure 6.1: Schematic of the ^{37}Al β^- decay chain with all values obtained from Ref. [1].

relatively short half-lives of the isotopes involved in each decay chain, a correlation time of 1000 ms was chosen to generate the decay curves.

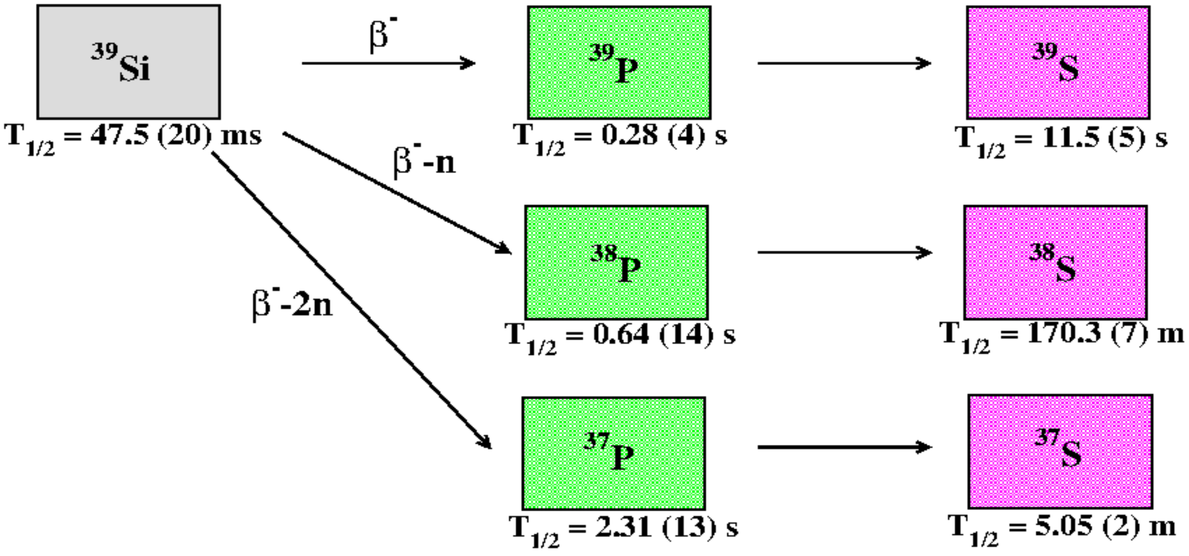

Figure 6.2: Schematic of the ^{39}Si β^- decay chain with values obtained through Ref. [1].

6.1 ^{37}Si Half-life

In the previous chapter, the PID spectrum, as seen in Figure 5.5, shows the very evident silicon isotope chain. However, ^{37}Si has very little counts relative to the other silicon isotopes. Fortunately, ^{37}Al is one of the strongest isotopes in the cocktail beam, allowing for significant production of ^{37}Si from its decay that would not have been present otherwise. Since the starting point is ^{37}Al and not ^{37}Si, the decay component associated with the ^{37}Al decay must be taken into account when fitting the decay curve. Equation 6.1 is the full Bateman equation used to fit the decay cuve as shown in Figure 6.3. Equation 6.1 includes the inital activity for ^{37}Al, denoted as N_{A0}, along with the decay constant for both ^{37}Al and ^{37}Si, λ_{37Al} and λ_{37Si} respectively, and the branching ratios, $P(0)$ and

$P(n)$, for the β^- and β^--n decays. An additional exponential background was included. The cause for need of an exponential background instead of a constant background is due to the fact that not *all* decays are taken into account (only the ones as shown in Figure 6.1) and the correlation time was selected to only be 1000 ms, meaning that longer-lived implants and decays contribute to the background.

$$\begin{aligned} N_{37_A}(t) = N_{A0}e^{-\lambda_{37Al}t} + P(0)\left[\frac{\lambda_{37Si}N_{A0}}{(\lambda_{37S} - \lambda_{37Al})}(e^{-\lambda_{37Al}t} - e^{-\lambda_{37Si}t})\right] \\ + P(n)\left[\frac{0.00154N_{A0}}{(0.00154 - \lambda_{37Al})}(e^{-\lambda_{37A}t} - e^{-0.00154t})\right] + b_1e^{-0.0007t} \end{aligned} \tag{6.1}$$

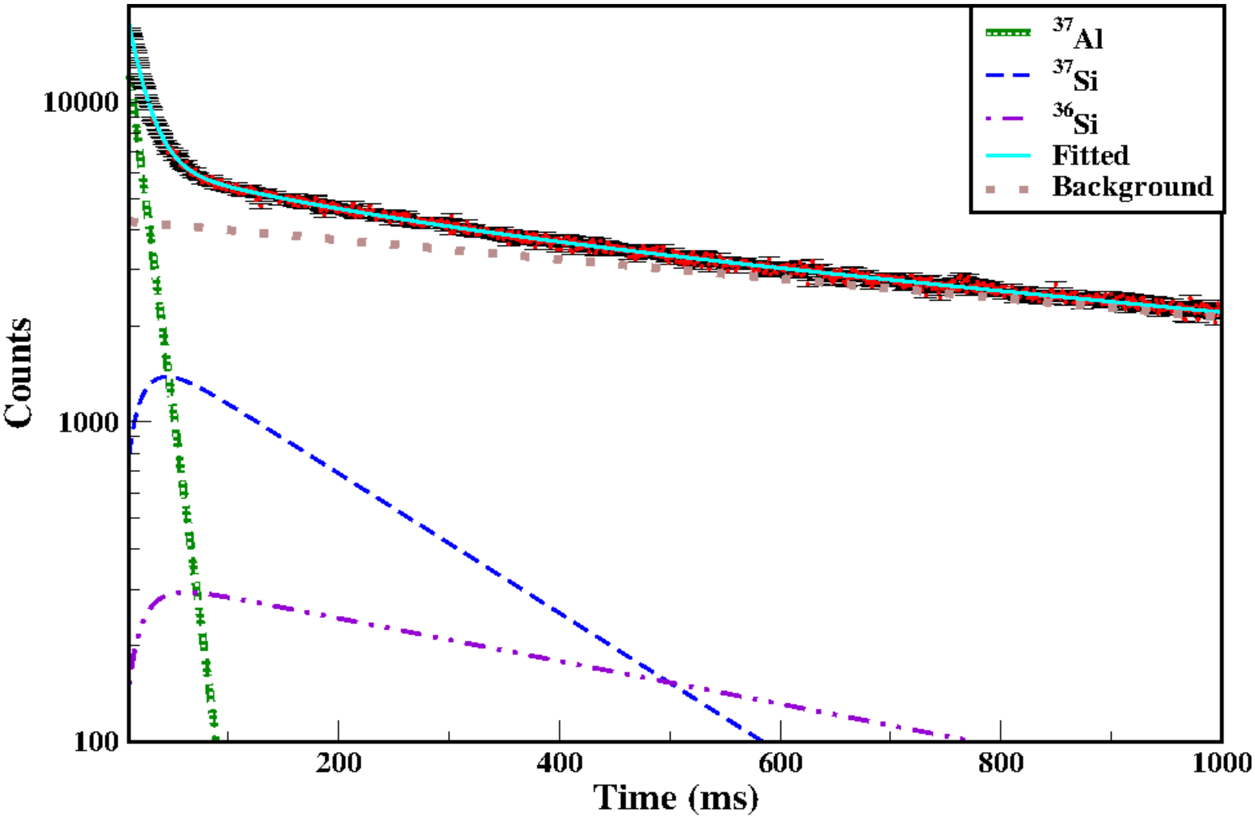

Figure 6.3: The decay curve of ^{37}Al taken for one second from the initial ^{37}Al implant, including the parent and daughter isotopes. Each individual component, labeled accordingly, correspond to each piece of the decay curve in the full Bateman decay equation with an additional slowly decaying exponential background, as given by Equation 6.1.

The fit using Equation 6.1, in which the free variables were the inital activity of ^{37}Al and background, extracted a half-life of 138 (4) ms for ^{37}Si. $P(n)$ was set to 55% as reported from Ref. [1] and the decay constant for ^{37}Al remained fixed, after previously extracting a half-life of 11.3 (2) ms through a γ gated decay curve. An inital activity, N_{A0}, of approximately 23.3 K, was also extracted.

In addition to extracting the decay curve through the correlation of implants and decays, the same decay curve can be obtained by making a gate on γ rays that are in coincidence with the β^- decaying nucleus of interest. In this case, since the desired half-life is of ^{37}Si, the decay curve will be generated using γ rays that are emitted from ^{37}P. The benefit of obtaining half-life measurements through this method is the reduction in decay components that are required for the fit. Referring back to Figure 6.1, if the decay curve is generated through the γ rays present in ^{37}P, then the only fitting required is the portion of ^{37}Si that is being created and is decaying. Figure 6.4 shows the resulting fit extracted from the previously reported 861-keV γ ray in ^{37}P [1]. For this fit, a background with a very small exponential variance was used due to the fact that *only* the creation and decay of ^{37}Si isotopes are present during this 1000 ms time correlation between decay of the parent nucleus and the γ rays emitted from the granddaughter nucleus and is thus not as sensitive to longer-lived implant isotopes as the prior fit. The resulting half-life extracted of 134 (8) ms is in excellent agreement with the half-life extracted without γ coincidences.

6.2 Half-life of ^{39}Si

In a similar manner to ^{37}Si, the half-life of ^{39}Si was extracted. Again, 1000 ms correlation time was used and Equation 6.2 shows the full Bateman equation that was utilized to fit the decay curve of ^{39}Si. The decay components that were included in the fit can be seen in Figure 6.2. The initial activity of ^{39}Si, N_{S0}, and the decay constant, $\lambda_{^{39}Si}$ were fit, along with the branching ratios, $P(0)$ and $P(n)$. Figure 6.5 shows the result of the fits.

$$\begin{aligned} N_{^{39}Si}(t) = N_{S0}e^{-\lambda_{^{39}Si}t} + P(0)\left[\frac{0.00248N_{S0}}{0.00248-\lambda_{^{39}Si}}(e^{-\lambda_{^{39}Si}t} - e^{-0.00248t})\right] \\ + P(n)\left[\frac{0.00108N_{S0}}{0.00108-\lambda_{^{39}Si}}(e^{-\lambda_{^{39}Si}t} - e^{-0.00108t})\right] + b_2e^{-0.0006t} \end{aligned} \tag{6.2}$$

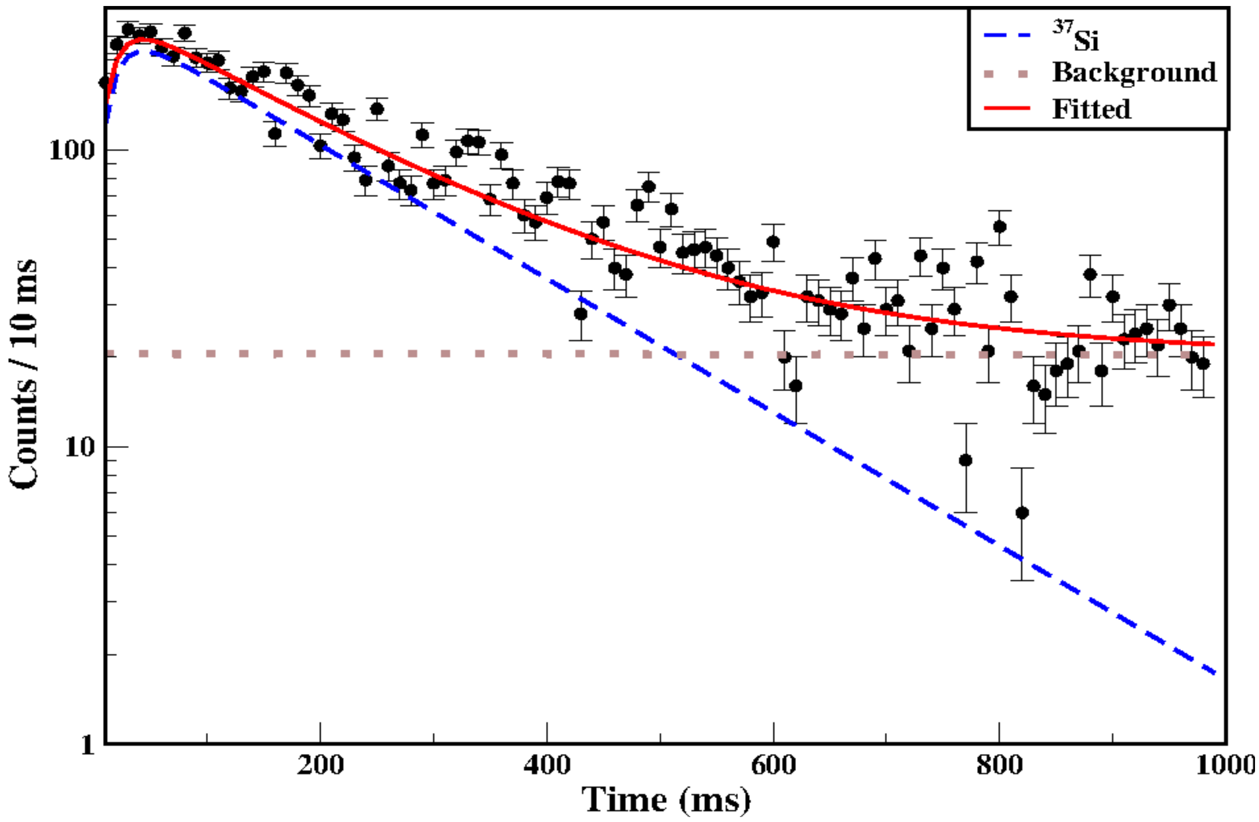

Figure 6.4: The γ-gated decay curve for ^{37}Si in coincidence with the 861-keV γ ray from ^{37}P. The reduction in counts is countered by the fact that only the decay component of ^{37}Si and a very small exponentially varying background is required, thus eliminating errors that come from the various fit components as shown in Equation 6.1.

As mentioned prior, an exponentially-varying background is utilized due to the fact that the background is highly sensitive to the implants of longer-lived isotopes. A half-life of 38.6 (1.3) ms was extracted from the fit, along with an initial activity, N_{S0}, of 57K.

The alternative method for extracting the half-life through the use of γ rays in the daughter nucleus was also utilized. In this case, the two strongest previously reported γ rays, 356- and 974 keV [1], in ^{39}P were used to gate the decay curve. Since the decay curve was taken from the γ rays found in the daughter nucleus, only the decay component of the parent, ^{39}Si, was required in the fit. Additionally, a constant background was used due to the fact that *only* the decay of ^{39}Si isotopes are present during this 1000 ms time correlation between decay of the parent nucleus and the γ rays emitted from the daughter nucleus and is thus not sensitive to longer-lived implant isotopes.

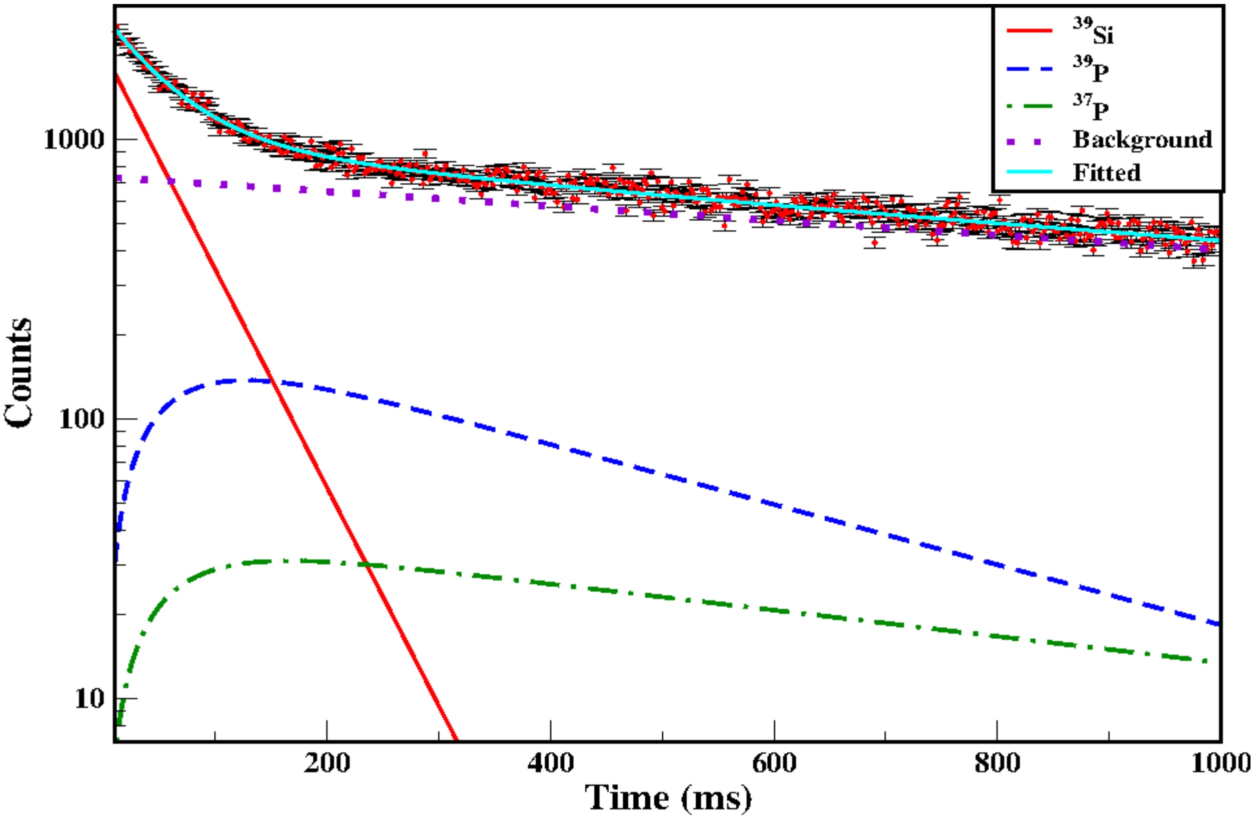

Figure 6.5: The decay curve of ^{39}Si taken during the time interval of one second, including the parent and daughter isotopes in Figure 6.2. Each individual, labeled accordingly, demonstrate the various decay fits for each piece of the decay curve using the full Bateman decay equation, as shown in Equation 6.2 with an additional slowly decaying exponential background.

Figure 6.6 shows the resulting fit. A half-life of 39 (3) ms was obtained and is in excellent agreement with the half-life obtained from Figure 6.5. Our half-life measurements reveal a somewhat shorter half-life than previously measured [42].

6.3 Fragment-$\beta - \gamma - \gamma$: Building the Levels

Extracting the half-life of a decaying nucleus does not only provide vital information that can be used to compare to theory models, it can also provide useful information for the analysis of the data. In the above section it was discussed that an exponentially varying background was required due to the contributions of longer-lived implanted isotopes. These longer-lived isotopes also pose problems when observing the $\beta^- - \gamma - \gamma$ coincidences as well. One benefit of extracting the half-life

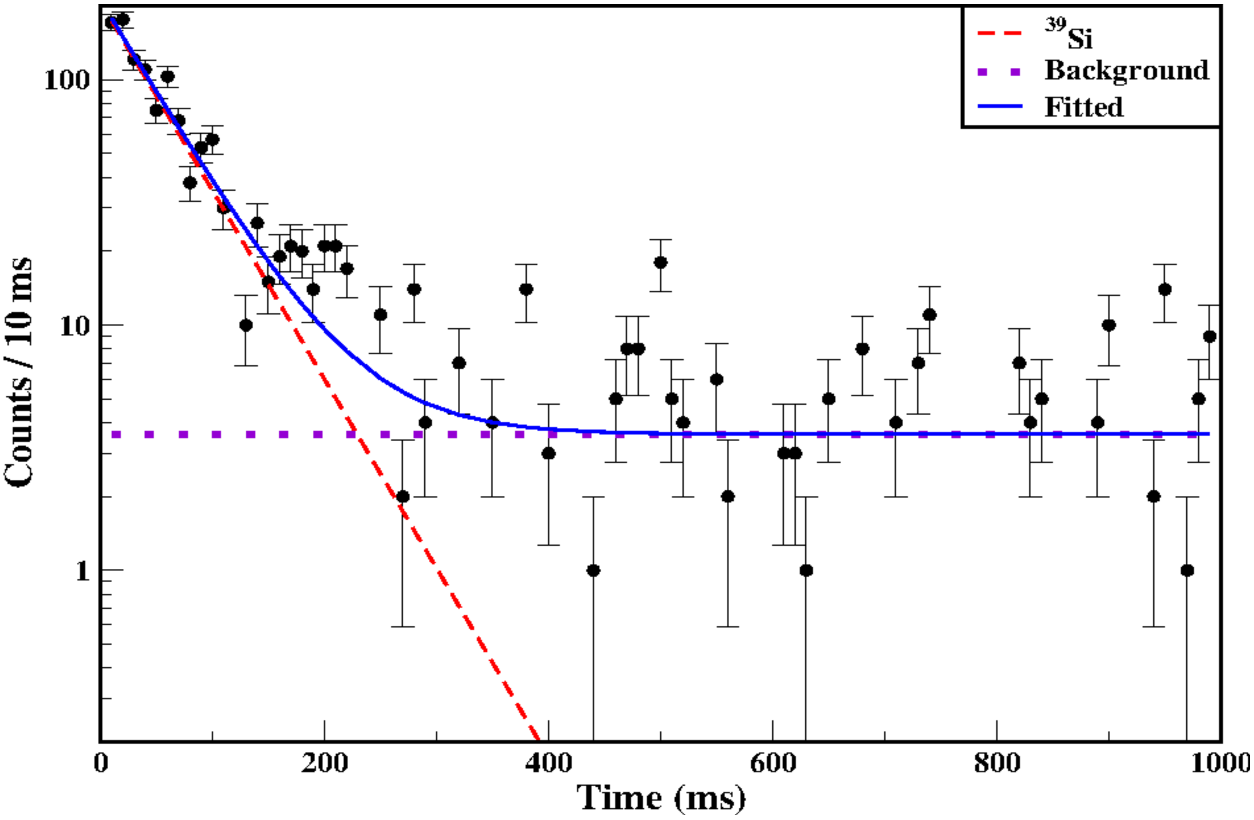

Figure 6.6: The γ-gated decay curve for ^{39}Si was extracted using the 356-keV and 974-keV γ rays in ^{39}P. Due to the lack of contributing factors to the decay curve, as in Figure 6.5, an initial fit for the half-life could be extracted easily without significant fluctuations from the background or various other contributions.

is that a relative time scale can be determined that will provide the most statistics with the least amount of contribution from longer-lived isotopes. Figure 6.7 shows how the different correlation time scales increase or decrease the peak-to-background ratio for the γ rays of interest. The half-life extracted for ^{39}Si was approximately 39 ms. This means that by 40 ms, exactly half of the starting ^{39}Si isotopes have decayed into an excited ^{39}P, meaning that the majority of counts in regards to the γ transitions from the excited states in ^{39}P will be present by 40 ms. Notice that in Figure 6.7 the 30-ms spectrum shows a significant 356- and 974-keV γ ray with a smaller peak at the 511 keV coming from the positron annihilation. Although the 30 ms time scale provides one of the cleanest spectrum, it is advantageous to also analyze a time scale in which approximately 90% of the ^{39}Si isotopes have decayed into ^{39}P. To determine a time scale that allows such, the standard decay

Table 6.1: Half-life measurements for ^{37,39}Si obtained through the fitting of the decay curves as shown in Figures 6.3, 6.4, 6.5 and 6.6. The † denotes the γ-gated values.

Isotope	$T_{1/2}$ (ms)	Previously Reported $T_{1/2}$ (ms)
^{37}Si	138 (4) 134 (8)†	90 (60) [1]
^{39}Si	38.6 (1.3) 39 (3)†	47.5 (20) [1]

equation can be used.

$$N(t) = N_0 e^{-\lambda t} \tag{6.3}$$

Recall that λ is the decay constant for ^{39}Si, or the parent nucleus, which was extracted through the half-life fit. Using the λ that was extracted and requiring that at least 90% of the silicon isotopes have decayed, the resulting time scale, t, is approximately 128 ms. After this time scale, the peaks that are from γ transitions in ^{39}P will not continue to grow relative to the background. This becomes apparent in Figure 6.7 with the 350 ms and 500 ms time scale spectra. The two ^{39}P peaks do not grow relative to the background, however the 511-keV peak and a new peak at 646 keV start to become rather large compared to the 30 ms spectrum. The peak at 646 keV is the ground state transition in ^{37}S which is produced through the decay of ^{37}P and is a contaminate.

With an appropriate time scale in place, the excited states can be identified through the γ transitions, starting with the two previously reported γ rays, 356- and 974 keV [1]. Unlike the data presented in Chapter 3, the data obtained through this particular experiment has poor statistics. The minimal counts can become a hindrance, however the relatively high selectivity and low background allow for useful information to be obtained despite the poor statistics. The only other concern is the potential of misidentifying whether or not a γ ray has the potential to be a transition from ^{38}P or other close isotopes with little to no knowledge about them, as will be discussed later.

The lowest ground-state transition, 356 keV, decaying from a $J^{\pi} = 3/2^{+}$ state, and the second lowest ground-state transition, 974 keV, decaying from a $J^{\pi} = 5/2^{+}$ state, are thought to be the best γ transitions to observe $\gamma - \gamma$ coincidences. Because the parent nucleus, ^{39}Si, has a tentative ground state of $J^{\pi} = (5/2^{-})$ and β^{-} decays favor decaying to a state with the same parity (see

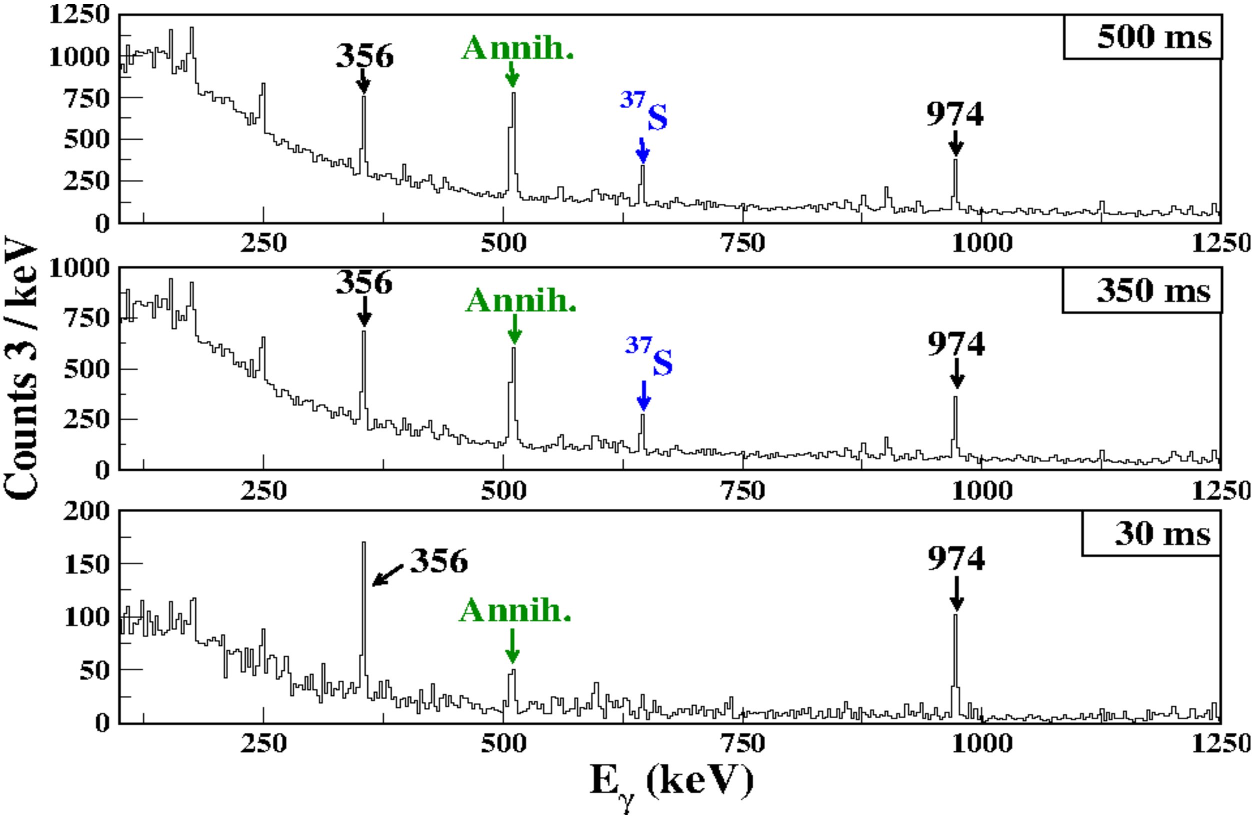

Figure 6.7: Spectra taken from different time correlation windows, comparing the growth of γ transitions from ^{39}P relative to the growth of transitions from longer-lived isotopes such as ^{37}S. The spectra show that at the shortest time scale of 30 ms, the two strongest γ transitions are already prominent relative to the background, whereas the transition from ^{37}S or the peak from positron annihilation only become prominent relative to the background at larger time scales.

β^--decay rules in Table 5.1), the likeliness of a direct β^- decay to either of these states is very small: it can therefore be assumed that they are being fed through other γ transitions. This hypothesis is thoroughly proven to be the case as all of the newly discovered γ transitions in this study cascade through either the 356- or 974-keV γ rays.

The lowest transition is the second strongest γ transition, with a relative intensity [scaled to the 974-keV γ ray] of 79% and has four out of the 15 newly observed γ transitions feeding into it. The previously reported γ transition of 619 (7) [1] was observed as a very weak γ ray at 618 keV with approximately 11% relative intensity. Additionally, three stronger and one weak tentative new transitions were observed to feed directly into the 356-keV γ transition. Figure 6.8 shows the five

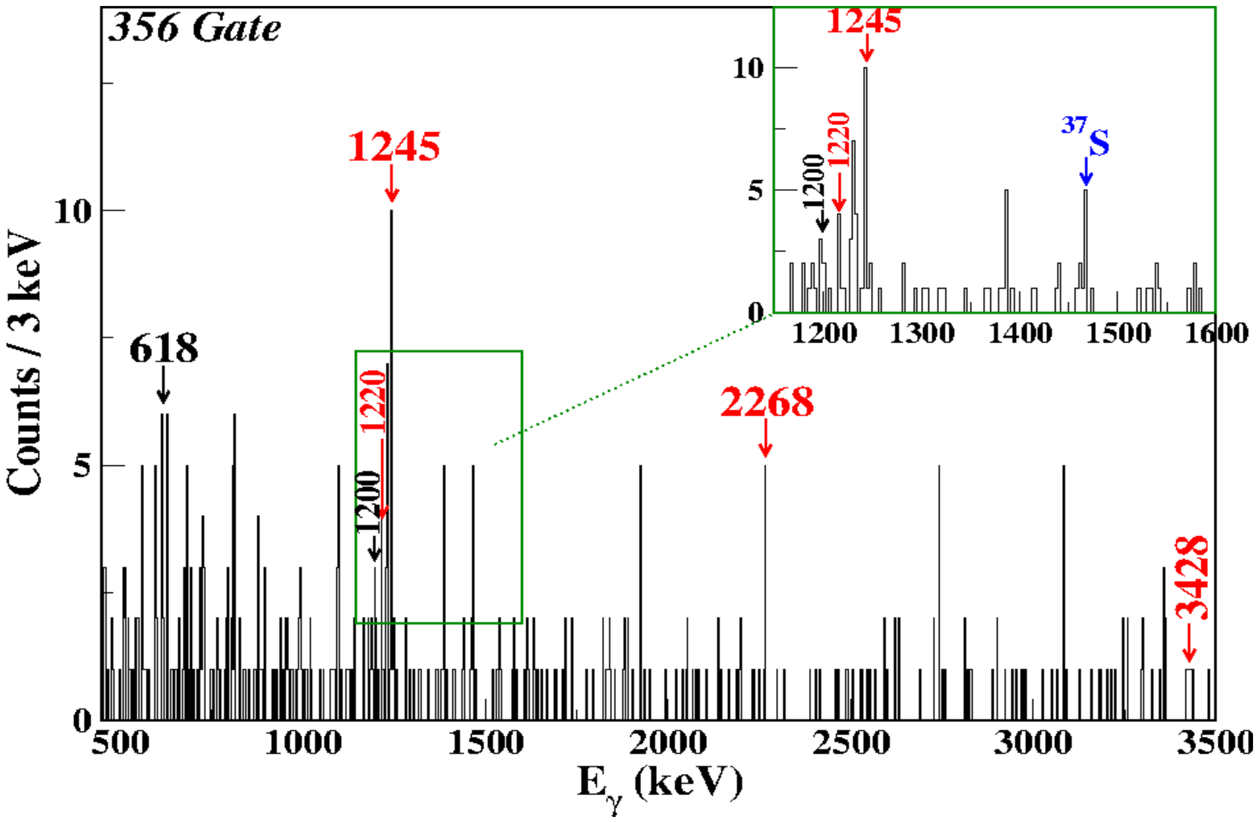

Figure 6.8: A spectrum obtained with a gate on the lowest γ transition, 356-keV. The spectrum shows the cluster of γ rays near 1200 keV, along with three other γ peaks that feed directly into the 356-keV excited state. The spectrum was taken using a 225-ms time correlation window.

γ rays that directly feed the 356-keV γ ray.

To be sure that these five γ rays are in true coincidence with the 356-keV γ ray, reverse gates are required. As explained in Chapter 3, in order for two γ rays to be in true coincidence with each other, they must appear in each others gates. Figure 6.9 shows the 356-keV γ ray, along with reverse gates obtained from the 2268-keV γ ray (top) and the 3428-keV γ ray (bottom). Both reverse gates show a very clear and distinct 356-keV peak showing that they are both in true coincidence with the 356-keV γ transition. Additionally, Figure 6.9 shows three other transitions not previously mentioned. These three γ transitions feed directly into the 974-keV excitd state and are apparent in the 356-keV gate because of the fact that the 618-keV γ ray decays from the 974-keV state to the 356-keV state, allowing for the transitions that are seen in the 974-keV gate

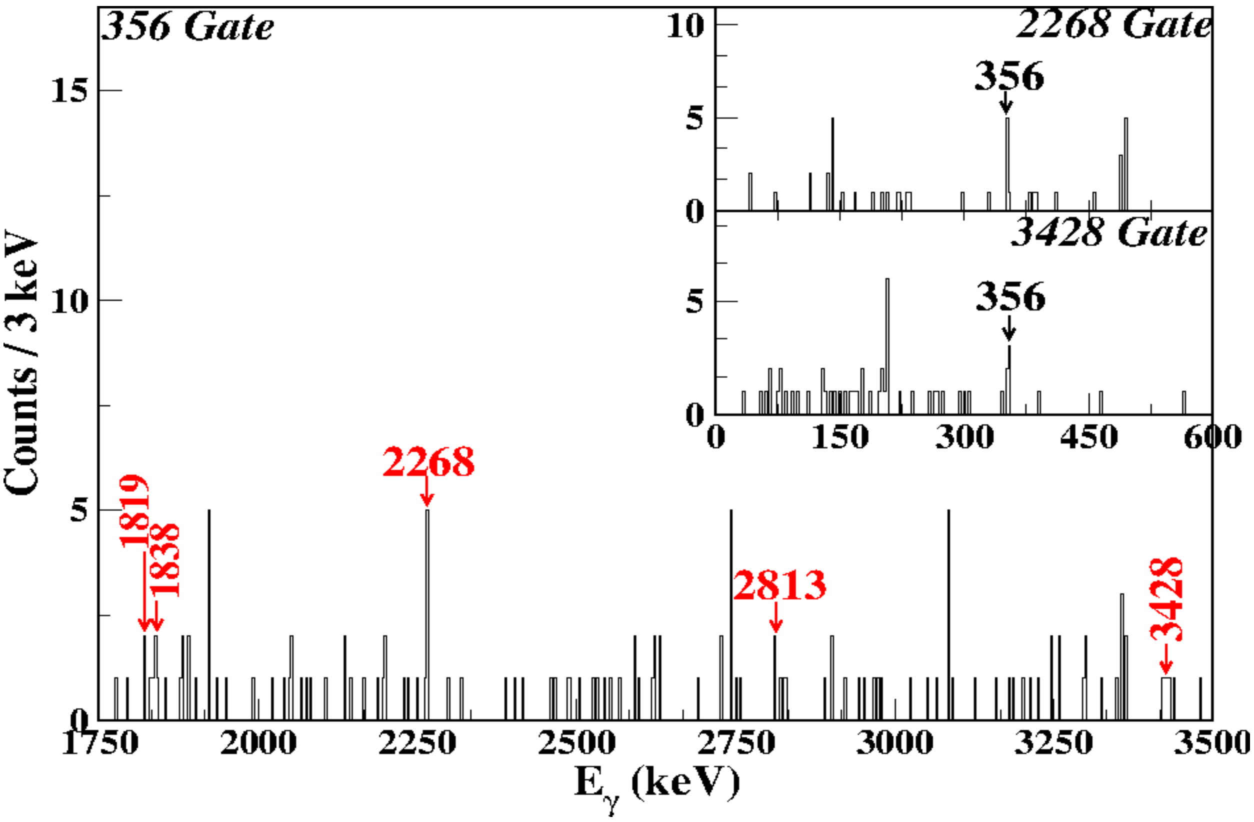

Figure 6.9: The same spectrum as obtained in Figure 6.8 with the addition of two other γ transitions that directly feed the excited state at 974 keV instead of the 356-keV excited state. Additionally, the inserted spectra demonstrate that the 3428-keV γ ray (bottom) and 2268-keV γ ray (top) are in true coincidence with the 356-keV γ ray.

to also be seen in the 356-keV gate. This is also how to determine whether or not a γ ray feeds into the 974-keV state or directly to the 356-keV state.

Although the majority of γ transitions decay to one of the first two excited states, it is also possible for a new γ transition to cascade through a series of transitions. One such example can be observed from the prominent 1245-keV γ transition. This transition is one of the strongest, with a relative intensity of 20%, creating a new excited state at 1600 keV. The new state is then fed by another newly observed γ transition, 2237 keV. Figure 6.10 shows the spectrum generated by gating on the 1245-keV γ ray, showing a very distinctive peak at 2237 keV, along with a 356-keV peak. The smaller insert spectrum, taken from a reverse gate on the 2237-keV γ ray shows a clear 1245-keV peak, proving that the two are in fact in true coincidence. The next question is whether or not the 2237-keV γ ray feeds directly into the 356- or 1245-keV γ ray. This can be determined through the intensity of each of the γ rays relative to each other. Notice that the 1245-keV peak is significantly stronger than the 356-keV peak in the 2237-keV gate: this indicates that the 2237-keV γ ray feeds directly into the 1245-keV γ ray or vice versa, creating a new excited state at 3837 keV. The presence of the 974-keV γ also is indicative that the 2237-keV γ transition sits above the 1245-keV γ ray.

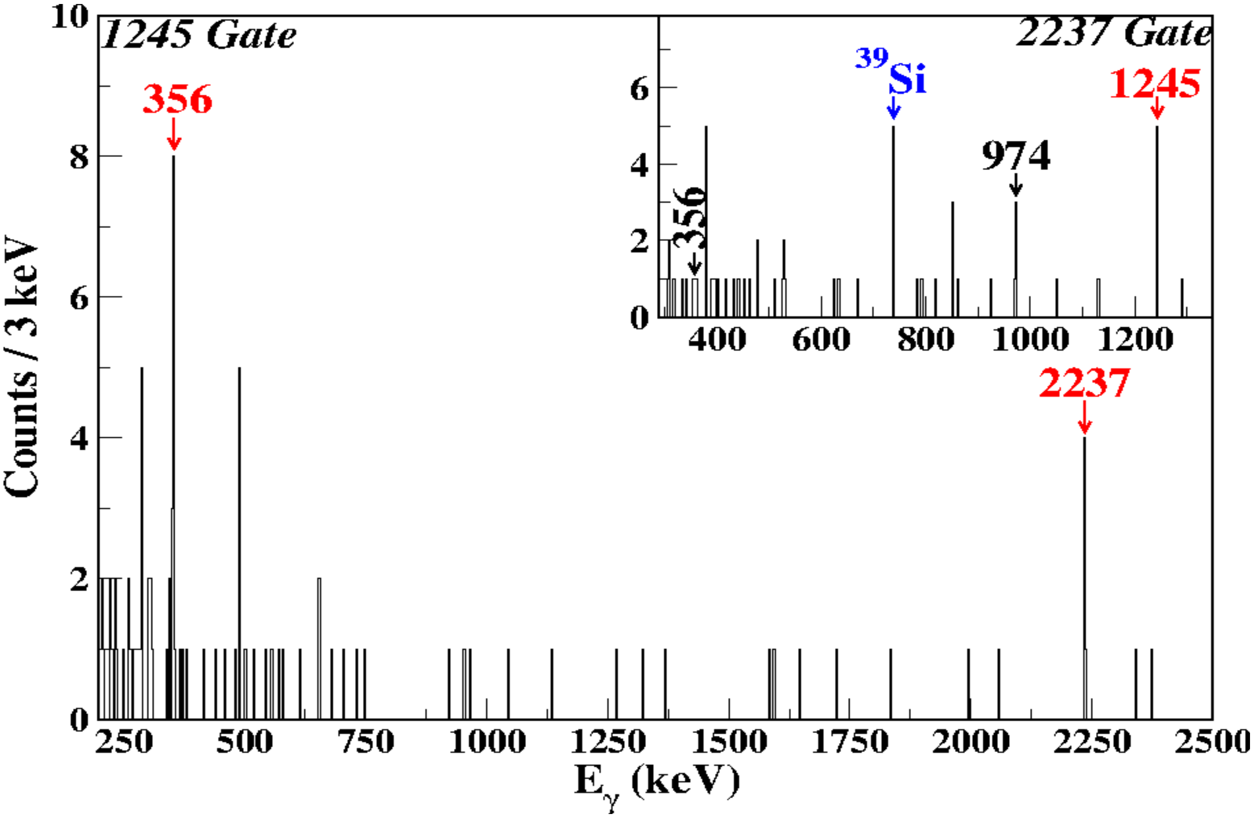

Figure 6.10: Spectrum generated through a gate made on the strongest γ transition feeding the excited state at 356 keV. The 1245-keV γ gated spectrum shows a strong peak at 356 keV along with a strong peak at 2237 keV, implying that 1245-keV γ transition is in coincidence with both γ rays. The inserted reverse gated spectrum made on the 2237-keV γ ray further proves that the 1245-keV and 2237-keV γ rays are in true coincidence with each other. Both spectra were obtained using a 225-ms time correlation window.

The remaining newly observed γ transitions all filter through the 974-keV excited state. Figure 6.11 shows a typical spectrum taken from a gate on the 974-keV γ ray. The first thing to take notice of is the peak at 1220 keV. Notice that this peak is present in both the 974- and 356-keV spectrum (see Figure 6.8): this indicates that the 1220-keV γ feeds into the 974-keV excited state and not directly into the 356-keV state, just as the 2237-keV γ as mentioned above. Conversely, the 1245-keV peak which is present in the 356-keV gate is not present in the 974-keV gate. This verifies that the 1245-keV γ transition feeds directly into the 356-keV state. Observing the appearance or lack thereof a certain peak in the various gates, such as this, helps to place the γ rays within the level scheme.

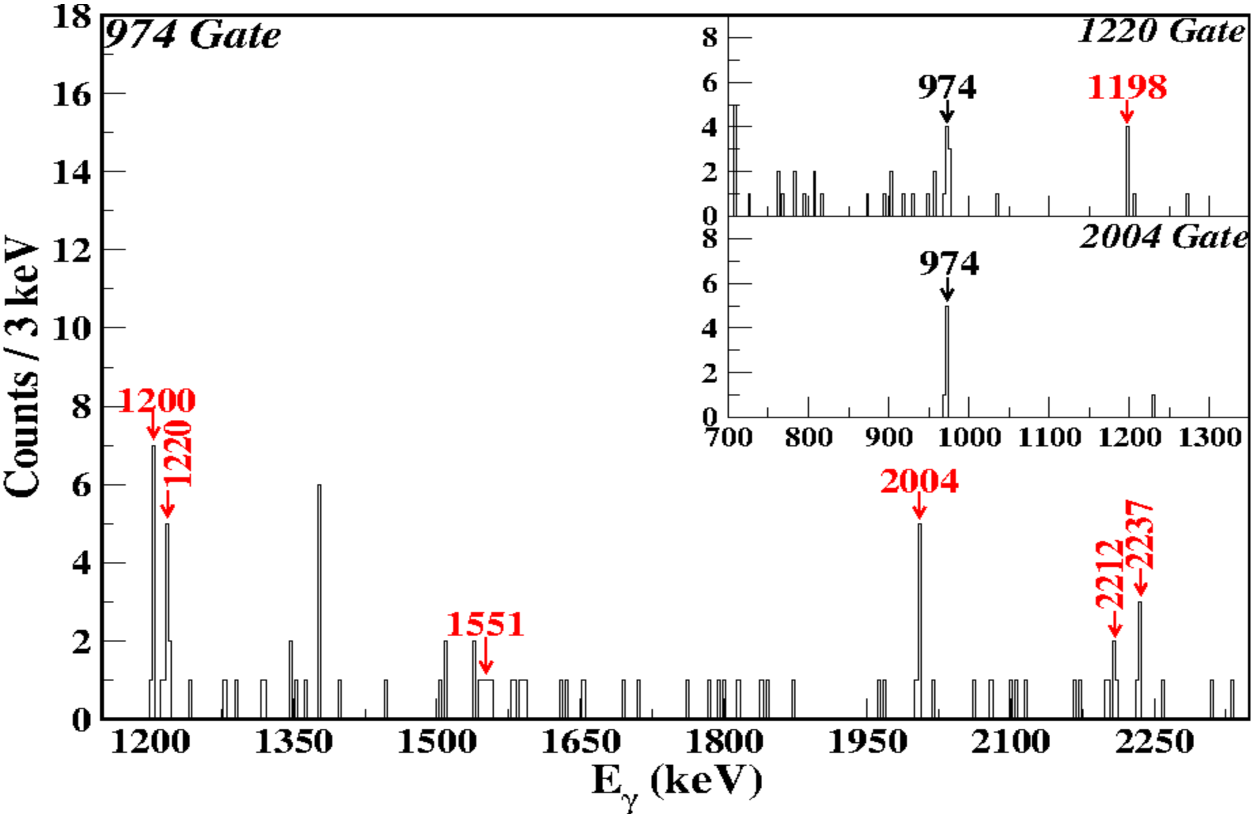

Figure 6.11: A spectrum obtained with a gate on the strongest γ transition, 974-keV. The spectrum show some of the stronger γ transitions that feed directly into the 974-keV excited state. Additionally, two inserted reverse spectra made through gates on the 2004-keV γ ray (bottom) and the 1220-keV γ ray (top) demonstrate that the two γ transitions are in true coincidence with the 937-keV γ ray. The 1220-keV spectrum also shows clear coincidence with the 1198-keV γ ray, placing the transition such that the 1198-keV γ transition directly feeds the 1220-keV γ ray. The spectra were all taken using a 225-ms time correlation window.

The majority of the time, simple series of gates is all that is required to determine the placement of a newly observed γ transition. However, despite the fact that the selectivity is high due to the threefold requirement of $\beta^- - \gamma - \gamma$, it is possible for γ transitions to be present that come from a near by contaminate. This was briefly discussed above and is one of the reason for selecting a certain time window for the analysis. As the neutron number significantly increases, and the nuclei become more exotic, naturally, less is known about them. The lack of knowledge can pose problems when trying to identify whether or not an observed γ ray belongs to one particular isotope or another. This is the case with a newly observed γ ray with an energy of 1551 keV. Figure 6.11 shows a broad peak at 1551 keV in the 974-keV gated spectrum. Figure 6.13 shows the reverse gate made on the 1551-keV γ ray. Notice a very clear peak at 974 keV and also at 1819 keV. A separate gate on the 1819-keV γ ray (top spectrum, Figure 6.13), also shows clear peaks at 974- and 1551-keV. It is clear that the 1551- and 1819-keV γ rays are in true coincidence with each other. The relationship among the two and the 974-keV transition is slightly ambiguous.

Observing the 974-keV gated spectrum in Figure 6.11 shows that there is at least one count where the 1819-keV peak should be. Naturally, it could be assumed that this is simply background, however the clear 974-keV peak in the 1819-keV gated spectrum begs to differ. It is quite possible that the 1819-keV γ transition does not directly feed into the 974-keV γ ray, which would reduce the intensity of the 1819-keV peak in the 974-keV spectrum. If this be the case, the 1819-keV γ ray would feed directly into the 1551-keV γ ray, which in turn would feed directly into the 974-keV state. Doing so would create the highest observed excited state at 4343 keV.

The arrangement of the three γ rays is taken to be true for this study, although with slight hesitation, making their placement in the level scheme for ^{39}P inconclusive.

6.4 Calculating log*ft*

With the γ transitions in place, it is important to try and put constraints on the J$^{\pi}$ of the newly observed excited states. In Chapter 5, log*ft* was described as a method of determining whether or not the β^- decay transition is to a particular state is considered allowed or forbidden, with Table 5.1 showing the rules for each type of transition. The log*ft* of a particular state is directly related to the probability of the parent nucleus to feed directly to that particular state. I_β, or the direct β feeding, is therefore used to determine what percentage the state is being populated through β^- decay or γ transitions from a higher lying state. The equation below, shows the simple idea of how

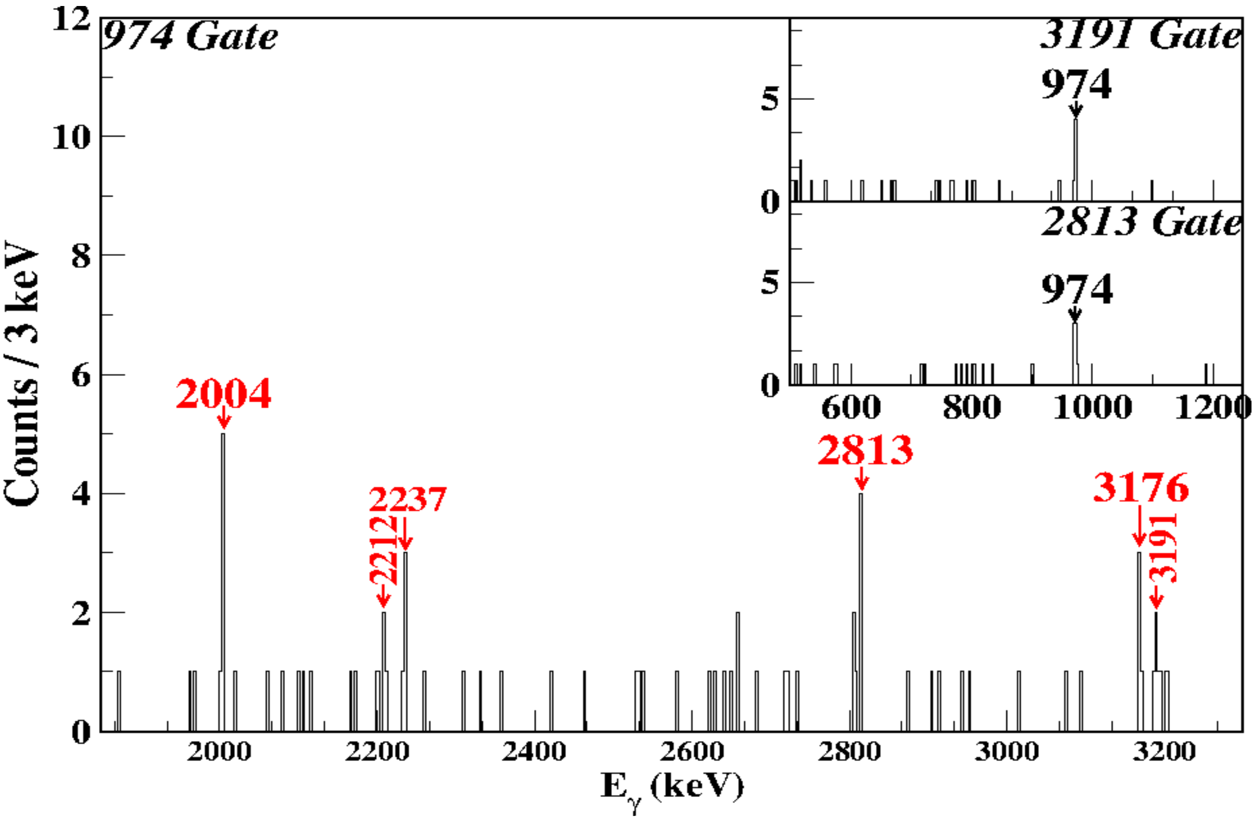

Figure 6.12: The same spectrum generated as in Figure 6.11 showing additional γ rays, including one of the most intense γ transition, 3191 keV. Reverse gates made on the 3191-keV and 2813-keV γ transitions (top and bottom, respectively) demonstrate that the two γ rays are in true coincidence with the 974-keV γ ray.

I_β is calculated.

$$I_\beta = \sum \text{Efficiency Corrected Counts Out} - \sum \text{Efficiency Corrected Counts In} \tag{6.4}$$

Once the β^- branching of a state is calculated and normalized to the initial activity of the parent nucleus, the logft of the state can be calculated using a logft calculator, such as can be found in Ref. [1]. The results are presented in the table below, along with on the tentative level scheme, as seen in Figure 6.15. Table 6.2 shows the γ rays and their relative intensity that were used to calculate the logft. Further discussion of the logft results can be found in Chapter 7 and in Table 6.3.

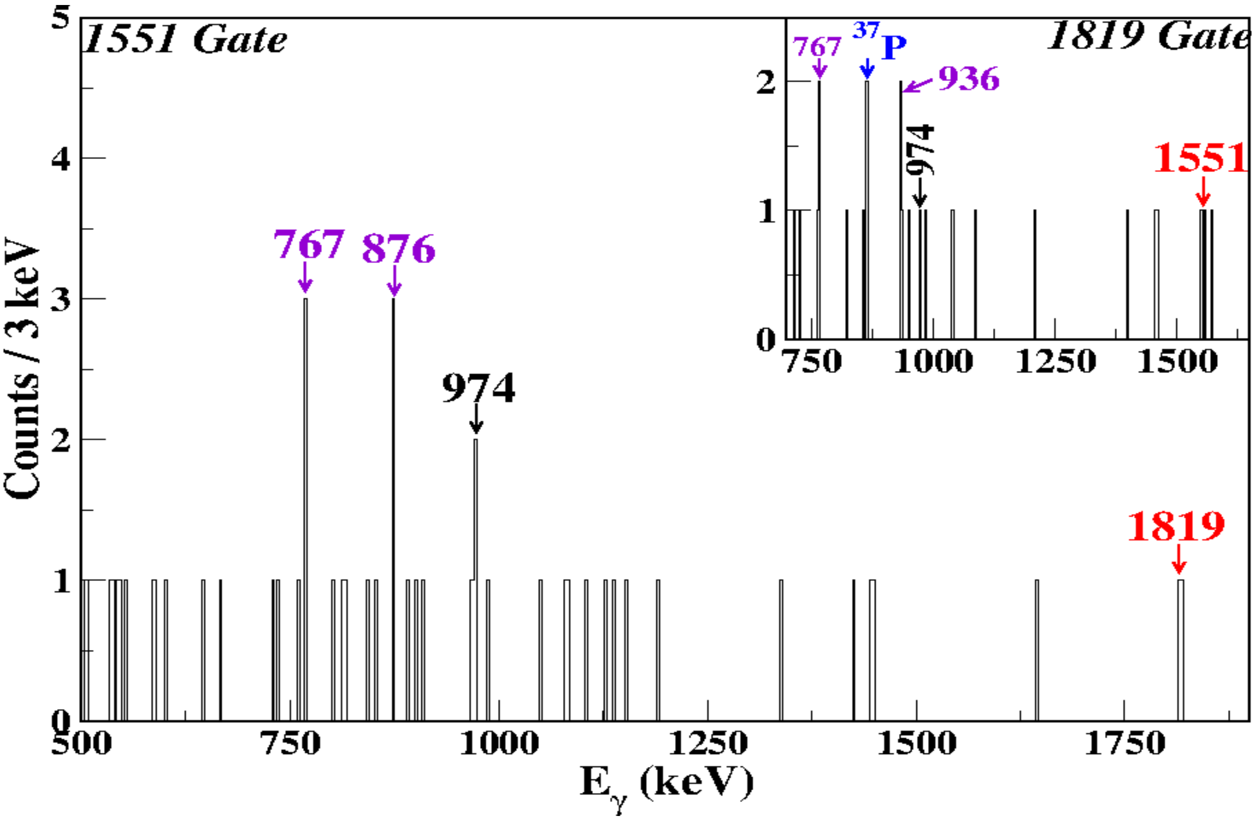

Figure 6.13: A 1551-keV γ gated spectrum showing the 974-keV and 1819-keV γ rays. A reverse gate made on the 1819-keV γ ray show the two are in true coincidence. In addition to the two γ transitions labeled in black and red, the peaks labeled in purple indicate γ rays that are of interest: it is inconclusive whether or not these three peaks belong to ^{39}P or if they are new transitions in surrounding isotopes such as ^{38}P. As all other spectra, these spectra were taken from a 225-ms time correlation window.

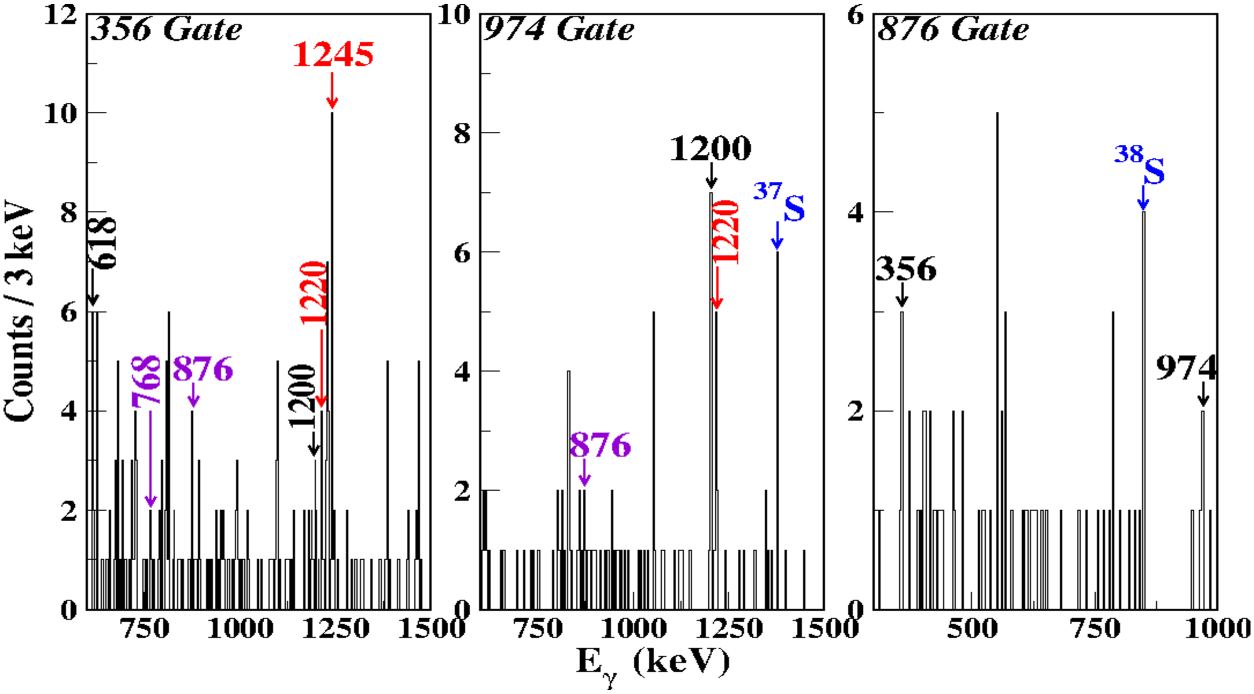

Figure 6.14: The spectra made through gates on the two strongest transitions at 356 and 974 keV, along with a gate made on the 876-keV γ transition. The three spectra show clear coincidence with each other, suggesting that the 876-keV γ ray may possibly belong to ^{39}P and requires further investigation.

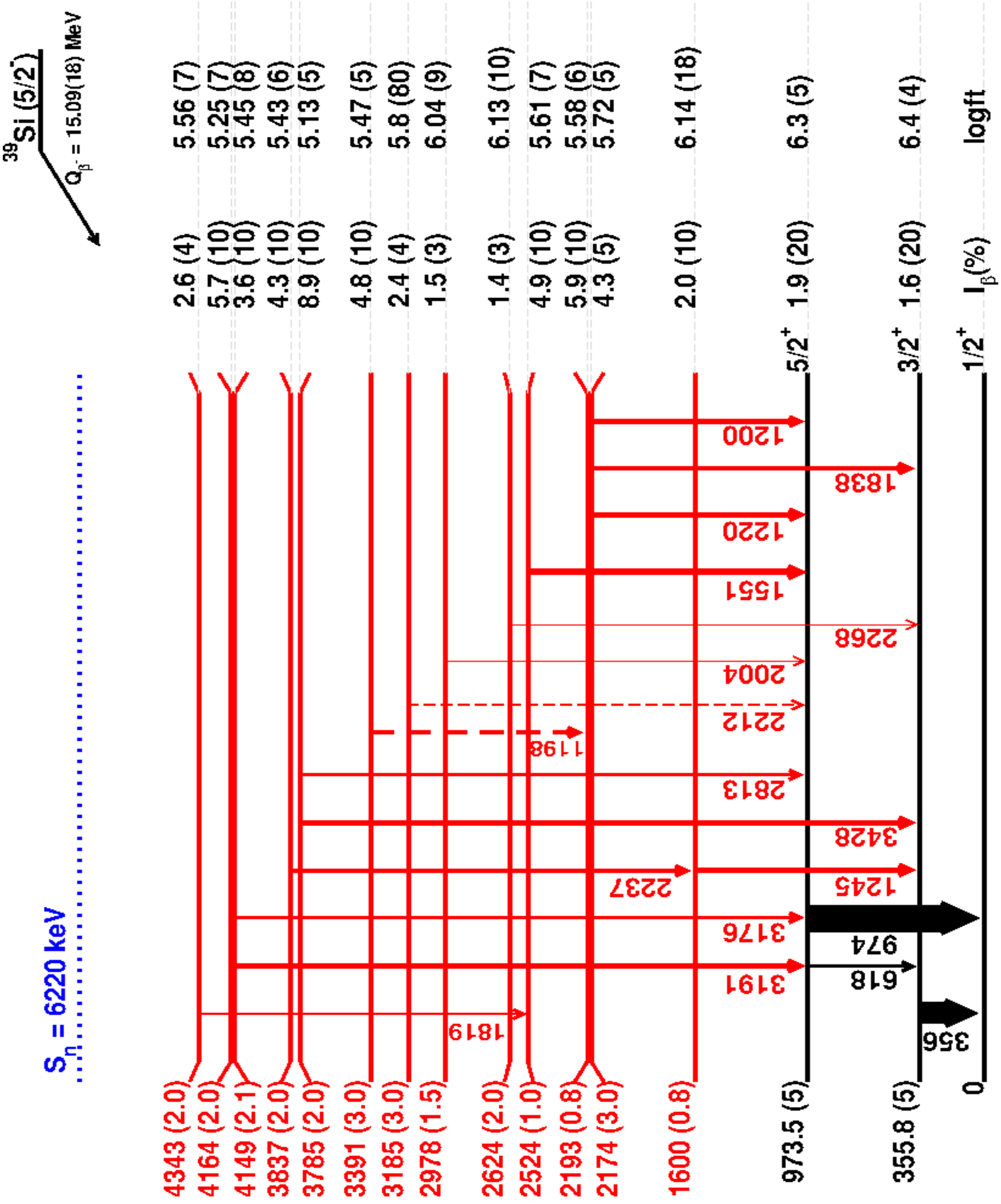

Figure 6.15: Level scheme for ^{39}P with calculated direct β feeding (I$_\beta$) and logft values. The red lines denote newly observed γ transitions and states. The black denotes previously observed transitions and states. The thickness of the transitions represent the relative intensity of the γ transitions scaled to the 974-keV γ ray.

Table 6.2: Excited states in ^{39}P as seen in this experiment with corresponding γ transitions and their relative intensity, normalized to the 974-keV γ ray.

Energy (keV)	Previously Reported	J^π	E_γ (keV)	Relative Intensity (%)
355.8 (5)	355 (1)	$(\frac{3}{2}^+)$	355.8 (5)	79 (7)
973.5 (5)	973 (1)	$(\frac{5}{2}^+)$	617.8 (20)	11 (3)
			973.5 (5)	100 (10)
1600.2 (8)			1244.5 (6)	20 (4)
2174 (3)	2167 (11)?		1200 (2)	14 (3)
2193.4 (8)			1219.9 (6)	18 (4)
			1837.7 (7)	17 (5)
2524.4 (10)			1550.9 (6)	25 (6)
2623.9 (20)			2268.1 (15)	4 (2)
2977.9 (15)			2004.4 (10)	5 (2)
3185 (3)			2211.5 (20)	7 (3)
3391 (3)			1198 (3)	15 (4)
3785.2 (20)			2812.5 (12)	11 (5)
			3427.8 (16)	20 (7)
3837.3 (20)			2237.1 (16)	14 (5)
4149.2 (21)			3175.7 (20)	13 (5)
4164.2 (20)			3190.7 (20)	21 (7)
4342.9 (20)			1818.5 (7)	9 (3)

Table 6.3: The excited states in ^{39}P with their direct β feedings (I_β) and resulting logft values, as calculated using the logft calculator available in Ref. [1]. The extracted T$_{\frac{1}{2}}$ along with the Q$_\beta^-$ of ^{39}Si were also required for the logft calculations.

Energy (keV)	I_β(%)	logft
355.8 (5)	1.6 (20)	6.4 (4)
973.5 (5)	1.9 (20)	6.3 (5)
1600.2 (8)	2.0 (10)	6.14 (18)
2174 (3)	4.3 (5)	5.72 (5)
2193.4 (8)	5.9 (10)	5.58 (6)
2524.4 (10)	4.9 (10)	5.61 (7)
2623.9 (20)	1.4 (3)	6.13 (10)
2977.9 (15)	1.5 (3)	6.04 (9)
3185 (3)	2.4 (4)	5.8 (80)
3391 (3)	4.8 (10)	5.47 (5)
3785.2 (20)	8.9 (10)	5.13 (5)
3837.3 (20)	4.3 (10)	5.43 (6)
4149.2 (21)	3.6 (10)	5.45 (8)
4164.2 (20)	5.7 (10)	5.25 (7)
4342.9 (20)	2.6 (4)	5.56 (7)

CHAPTER 7

β^- TAKES A WALK ON THE SHELL MODEL SIDE: COMPARISON OF β^- EXPERIMENTAL RESULTS TO SHELL MODEL CALCULATIONS

In Chapter 3, the use of *DCO* ratios as a way to help add constraints to the spin of excited states was discussed. β decay is a selective reaction that favors certain states over the other. Using this selectivity, along with the selection rules as discussed in Table 5.1, spin and parity constraints can be assigned, provided that the J^π of the parent ground state is known. In order to determine if a particular state is favored or not, $\log ft$ values are calculated experimentally as described in Chapter 6, with the results for ^{39}P shown in Table 7.1.

Table 7.1: The experimental $\log ft$ for the states as seen through the β^- decay of ^{39}Si, along with the direct β feeding (I_β) for each branch. $\text{Log}ft$ values were calculated using the $\log ft$ calculator in Ref. [1].

Exp (keV)	I_β(%)	$\log ft$
355.8 (5)	1.6 (20)	6.4 (4)
973.5 (5)	1.9 (20)	6.3 (5)
1600 (0.8)	2.0 (10)	6.14 (18)
2174 (2.9)	4.3 (5)	5.72 (5)
2193 (0.8)	5.9 (10)	5.58 (6)
2524 (1.0)	4.9 (10)	5.61 (7)
2624 (2.0)	1.4 (3)	6.13 (10)
2978 (1.5)	1.5 (3)	6.04 (9)
3185 (3.0)	2.4 (4)	5.8 (80)
3391 (3.0)	4.8 (10)	5.47 (5)
3785 (2.0)	8.9 (10)	5.13 (5)
3837 (2.0)	4.3 (10)	5.43 (6)
4149 (2.1)	3.6 (10)	5.45 (8)
4164 (2.0)	5.7 (10)	5.25 (7)
4343 (2.0)	2.6 (4)	5.56 (7)

Table 5.1 in Chapter 5 give range limits on the $\log ft$ that are used to determine if the β^- decay to a particular state is allowed or not. For an allowed decay, there is no change in parity and the

change in spin relative to the parent ground state can range from ΔJ = 0, ±1. Using these rules it can be seen that the majority of states are allowed but have very weak strengths. The states with relatively low logft (< 5.5) indicate the location of the states that likely have a negative parity, with a spin ranging from 3/2 to 7/2. These states are assumed to have negative parity due to the fact that the parent nucleus, ^{39}Si, has a ground state J$^{\pi}$ = $5/2^-$ meaning that the allowed β^- decays will go to states that have a negative parity and are within $1\hbar$ of the parent's ground state J$^{\pi}$.

Further constraints on the spin and parity of the states can be made by comparing Shell Model predictions. For this particular experiment, the SDPF-MU interaction is the interaction of choice. The SDPF-MU interaction is based off of the USD interaction for the sd-shell and the GXPF1B interaction for the fp-shell [3]. Figure 7.3 is the Shell Model interaction, SDPF-MU, compared to the excited states as seen in this experiment. In the figure, the left-hand side are the states predicted using the SDPF-MU interaction and the right-hand side are the experimental states. The blue experimental states denote the newly observed excited states that do not have a previously reported J$^{\pi}$. The red theoretical states denote the beginning of the negative states with spin ranging from 3/2 to 7/2.

Table 7.2: The theoretically calculated logft values for states with J$^{\pi}$ = $3/2^-, 5/2^-, 7/2^-$ using the SDPF-MU interaction [3]

Ex	J$^{\pi}$	logft
3.1	$7/2^-$	6.06
3.45	$3/2^-$	5.15
3.62	$5/2^-$	8.35
3.71	$5/2^-$	5.79
3.71	$7/2^-$	6.73
3.78	$3/2^-$	5.68
3.89	$3/2^-$	6.76
3.93	$7/2^-$	6.83
3.95	$5/2^-$	4.83
4.08	$3/2^-$	6.29
4.14	$7/2^-$	6.53
4.19	$5/2^-$	6.02
4.22	$5/2^-$	6.14
4.24	$3/2^-$	5.47
4.33	$7/2^-$	5.15

Observing the comparison between the theoretically calculated states and the experimental states, it is easy to see that the SDPF-MU interaction reproduces the low-lying states quite well. Additionally, the SDPF-MU interaction does not predict negative parity states until after approximately 3 MeV. This is comparable to what is seen experimentally with the logft values. The first two excited states that have a log$ft < 6.0$ are 2193 and 2524 keV. These states, however, have theory predicted candidates that have a positive parity. The next excited state with a log$ft < 6.0$ is the state at 3185 keV with a log$ft = 5.8$. The SDPF-MU interaction has the first $7/2^-$ state predicted to be at 3.10 MeV with a log$ft = 6.06$, indicating that this state is quite possibly the first negative parity state. The excited state at 3785 keV has the lowest logft value and matches well with the theory state at 3.45 MeV with a logft predicted to be 5.15. This is the first predicted $3/2^-$ state. The remaining results can be found in Table 7.2. The negative parity states in ^{39}P are created by promoting a nucleon, the solitary proton, across the Z = 20 shell, classifying the negative parity states as intruder states. The occurrence of intruder states at low excitation energies signify a reduced shell gap as seen in other neutron-rich nuclei.

Interestingly enough, there is no single state that carries the majority of the β^- decay strength in ^{39}P. Observation of the surrounding isotope decays, such as the β^- decay of ^{37}Al to ^{37}Si (also observed in this experiment), there is one particular state that carries the majority of the strength of the β^- decay. The SDPF-MU interaction also shows this. Additionally, the even-A phosphorus isotopes, as seen in Ref. [7] have one branch that is favorable. Since the strength of the β^- decay is fragmented between the excited states for odd-A phosphorus isotopes in this mass region, it may indicate that there is a poor overlap between the ground state of the parent nuclei, the silicon isotopes, and the negative parity states in the daughters, thus feeding a cluster of negative parity states with a spin ranging from 3/2 to 7/2.

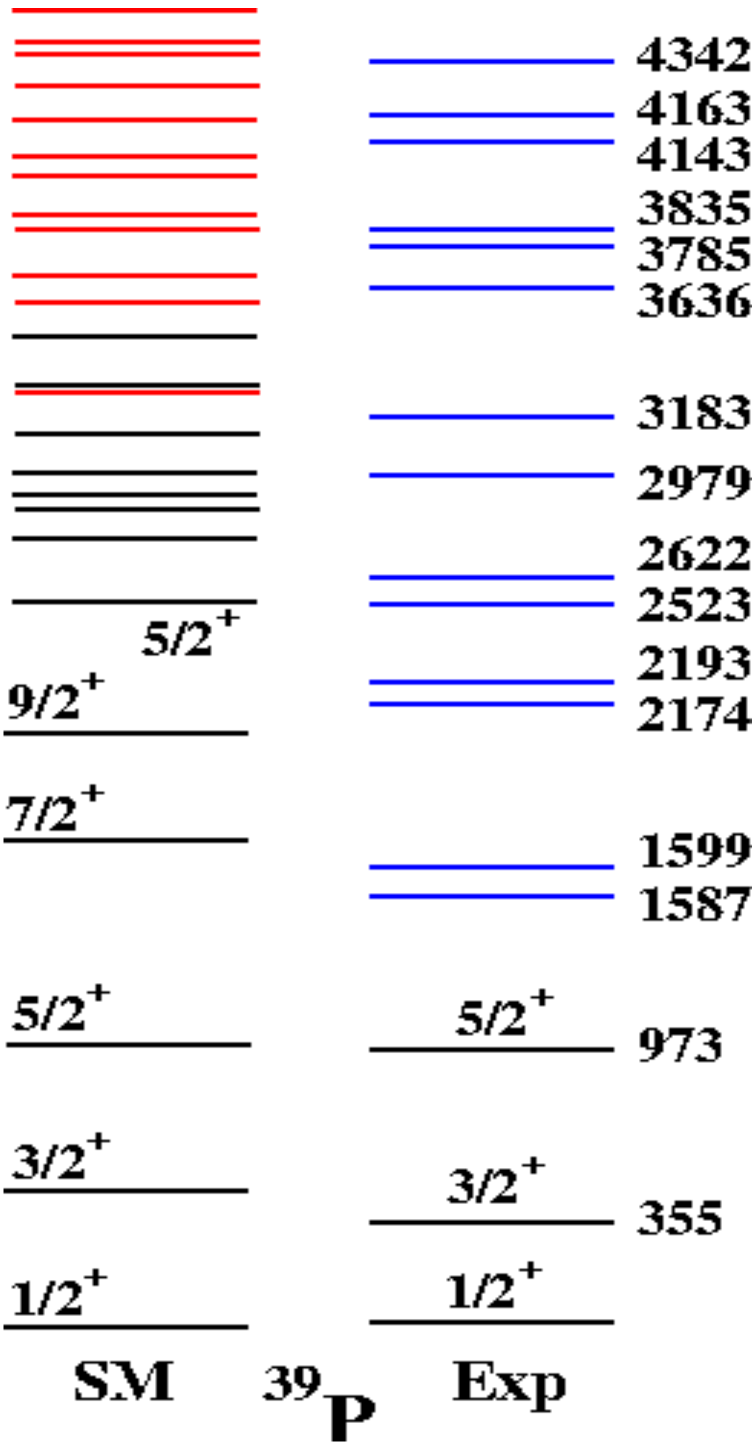

Figure 7.1: Comparison of the experimental states in ^{39}P, as seen in this experiment, compared to the theoretically calculated states obtained through the use of the SDPF-MU interaction [3]. The blue states denote experimental states with unknown J$^{\pi}$ and the red states denote the negative theory states with a spin ranging from 3/2 to 7/2. Due to the high level density, only the first five states of each spin are shown here.

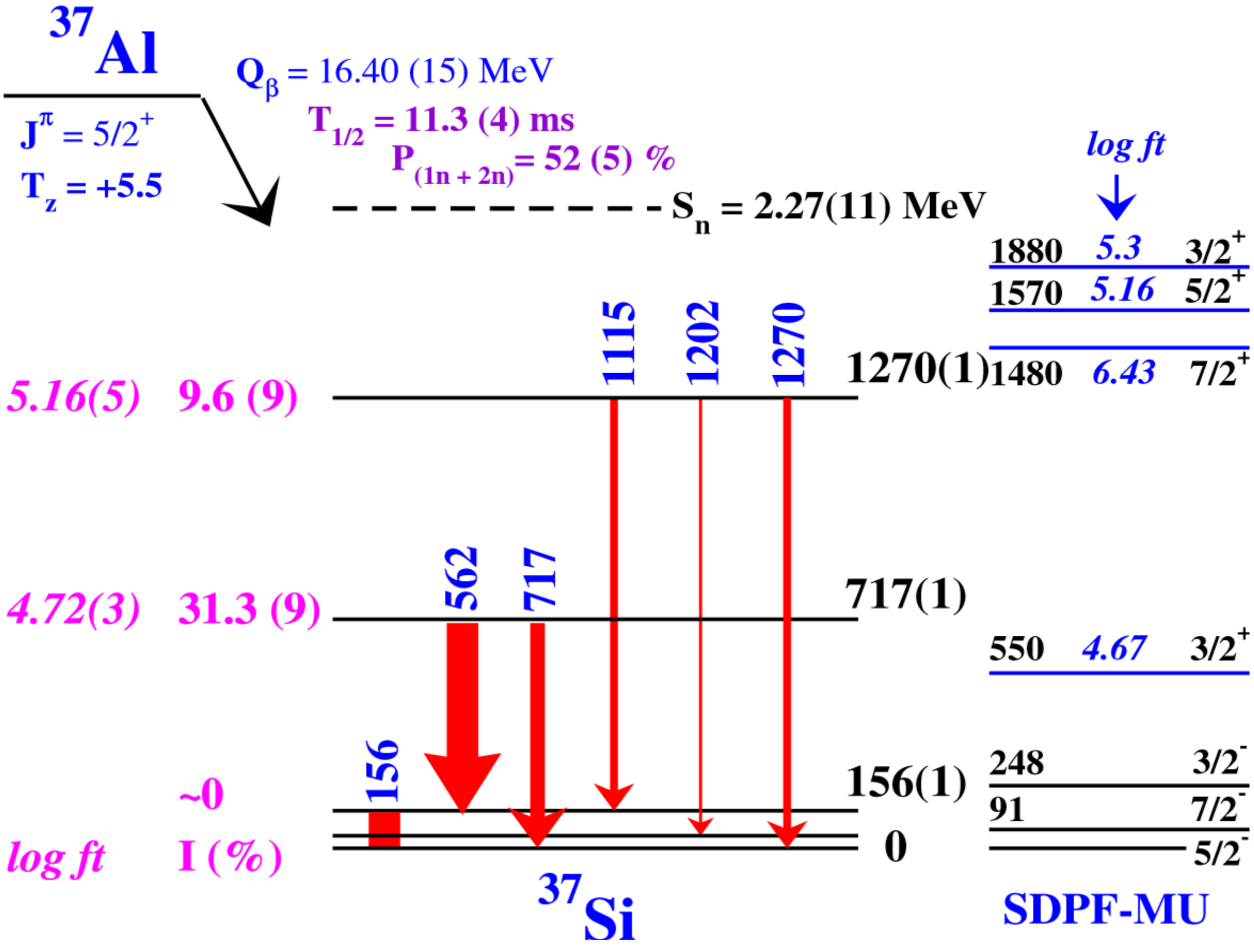

Figure 7.2: A partial level scheme of the β^{-} decay of ^{37}Al. Notice that the excited state at 717 keV contains the majority of the β^{-} decay strength. The SDPF-MU interaction also reproduces this.

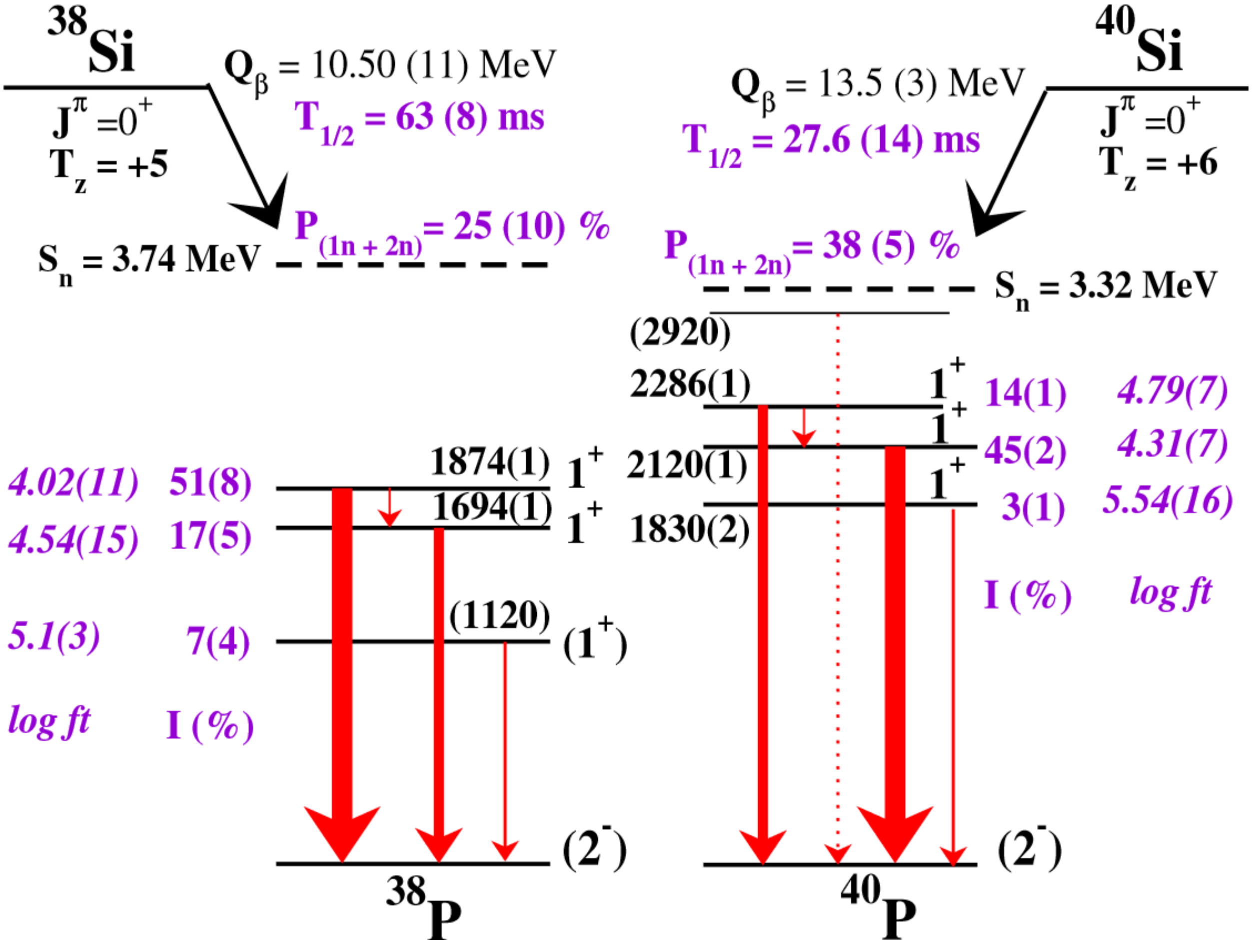

Figure 7.3: A partial level scheme for the even-A phosphorous isotopes as seen in this experiment [7]. Like the β^- decay of ^{37}Al, there seems to be one particular excited state that has the majority of the decay strength.

CHAPTER 8

CLOSING REMARKS

The structure of nuclei has been of interest for more than a century. With the advancement of accelerators and experimental/analyzing techniques, more and more knowledge is available to be obtained regarding the structure of nuclei. Whether it is learning more in-depth about previously studied isotopes or studying the structure of an isotope for the very first time, there is plenty of room for exploration for the years to come. Along with the improvement of the experimental data, the theoretical models also need to be constantly improving. Fortunately, the two go hand-in-hand with each other and allow for continuous advancements.

Through the study of high-spin using a fusion-evaporation reaction, the structure of intruder states across the shell gap between the sd- and fp-shells was explored. Transfer reactions that favor the creation of excited states with high-spin allowed for the comparison of two excited states between the two varying experiments, allowing for confirmation and constraints of spin assignments to be made. A new Shell Model interaction developed at FSU further confirmed spin assignments, while showing improvement for the prediction of intruder states relative to two other Shell Model interactions. The observation of several new high-spin states give rise to the idea that perhaps some of them may be two-particle-two-hole (2p-2h) states, meaning that two nucleons are promoted across the shell gap instead of one. This type of intruder state configuration would allow for high spins to be created but will change the parity to become negative instead of the positive parity that comes from 1p-1h states.

Moving down the A = 39 isobar chain from ^{39}Ar to ^{39}P, the use of β-delayed γ spectroscopy completed at the NSCL provided previously unknown knowledge regarding the nuclear structure of ^{39}P. Due to the fact that the experiment was conducted with a cocktail beam, half-life measurements were able to be done on ^{37}Si in addition to ^{39}Si, further constraining the half-life which had a very large error. After the newly observed excited states were finalized, the states and their logft values were able to be compared and characterized with another Shell Model interaction, further placing constraints on the spin and parity of each state. A observation of the behavior of the β^- strength to the intruder states in ^{39}P as seen experimentally and theoretically give rise to more questions such as why no one particular excited state carries the majority of the β^- decay strength when surrounding isotopes do.

Although a lot of new information is reported in this study for both isotopes, the newly gained information only further leads to more questions and experiments that need to be conducted in the further. The possible existence of 2p-2h states and a Shell Model code capable of calculating such states, along with the understanding of why ^{39}P does not have just one state that carries the majority of the β^- decay strength and whether or not other isotopes exhibit such behavior, are all significant questions that need to be answered about the structure of nuclei and require the work such as done in this report in order to find the answers.

REFERENCES

[1] National Nuclear Data Center. `http://nndc.bnl.gov`.

[2] B. Rubio and W. Gelletly *Lect. Notes Phys.*, vol. 764, pp. 99–151, 2009.

[3] Y. Utsuno, T. Otsuka, B. A. Brown, M. Honma, T. Mizusaki, and N. Shimizu *Phys. Rev. C*, vol. 86, p. 051301, 2012.

[4] John D. Fox Superconducting Linear Accelerator Laborator. `http://fsunuc.physics.fsu.edu`.

[5] LISE^{++}. `http://lise.nscl.edu/lise.html`.

[6] S. A. Suchyta, *Studies of the Neutron-Rich Nuclei Near N=40 Through β Decay.* PhD thesis, Michigan State University, 2014.

[7] V. Tripathi, R. S. Lubna, B. Abromeit, H. L. Crawford, S. N. Liddick, and Y. t. Utsuno *Phys. Rev. C*, vol. 95, p. 024308, 2017.

[8] V. Zelevinsky and A. Volya, *Physics of Atomic Nuclei.* Wiley-VCH, 2017.

[9] CoSMo. `http://www.volya.net`.

[10] K. S. Krane, *Introductory Nuclear Physics.* John Wiley and Sons, Inc., 1988.

[11] R. Bass, H. P. Haenni, T. W. Bonner, and F. Gabbard *Nuclear Phys.*, vol. 28, p. 478, 1961.

[12] R. Bass, U. Fanger, and F. M. Saleh *Nuclear Phys.*, vol. 56, pp. 569–576, 1964.

[13] R. Bass and F. M. Saleh-Bass *Nuclear Phys. A*, vol. 95, no. 1, pp. 38–64, 1967.

[14] R. Bass and F. M. Saleh-Bass *Nuclear Phys. A*, vol. 131, no. 3, pp. 673–678, 1969.

[15] R. R. Johnson and R. J. Griffiths *Nuclear Phys. A*, vol. 108, no. 1, pp. 113–123, 1968.

[16] J. F. Tonn, R. E. Segel, J. A. Nolen, W. S. Chien, and P. T. Debevec *Phys. Rev. C*, vol. 16, p. 1357, 1977.

[17] S. Sen, C. L. Hollas, C. W. Bjork, and P. J. Riley *Phys. Rev. C*, vol. 5, p. 1278, 1972.

[18] J. L. Wiza, J. D. Garrett, and R. Middleton *Nuclear Phys. A*, vol. 183, no. 2, pp. 439–448, 1972.

[19] E. K. Warburton, J. W. Olness, J. J. Kolata, and A. R. Poletti *Phys. Rev. C*, vol. 13, p. 1762(R), 1976.

[20] J. F. Tonn, R. E. Segel, W. C. Corwin, and L. R. Rutledge Jr *Phys. Rev. C*, vol. 16, p. 2065(R), 1977.

[21] H. Nann, W. S. Chien, A. Saha, and B. H. Wildenthal *Phys. Rev. C*, vol. 15, p. 1959, 1977.

[22] B. Rosner and E. J. Schneid *Phys. Lett.*, vol. 19, pp. 692–694, 1966.

[23] A. Graue and L. Herland *Phys. Norvegica.*, vol. 2, p. 137, 1967.

[24] S. Sen, S. E. Darden, W. A. Yoh, and E. D. Berners *Nuclear Phys. A*, vol. 250, no. 1, pp. 45–72, 1975.

[25] W. C. Corwin and R. E. Segel *Phys. Rev. C*, vol. 15, p. 505, 1977.

[26] W. A. Sterrenburg, G. van Middelkoop, J. A. G. de Raedt, A. Holthuizen, and A. J. Rutten *Nuc Phys. A*, vol. 306, no. 1-2, 14-21, 1978.

[27] J. Keinonen, K. P. Lieb, H. P. Hellmeister, and F. J. Bergmeister *Z. Phys.*, vol. A282, p. 227, 1977.

[28] D. M. Drake, J. D. Moses, J. C. Peng, N. Stein, and J. W. Sunier *Phys. Rev. Lett.*, vol. 45, p. 1765, 1980.

[29] D. Shapira, J. L. C. Ford, Jr, R. Novotny, B. Shivakumar, R. L. Parks, and S. T. Thornton *Nucl. Instrum. Methods*, vol. 228, p. 259, 1985.

[30] G. Wang, E. K. Warburton, and D. E. Alburger *Phys. Rev C*, vol. 35, p. 5, 1987.

[31] R. W. Ibbotson, T. Glasmacher, P. F. Mantica, and H. Scheit *Phys. Rev. C*, vol. 59, p. 642, 1999.

[32] O. Sorlin, Z. Dombrádi, D. Sohler, F. Azaiez, J. Timár, and Y. E. t. Penionzhkevich *Eur. Phys. J. A*, vol. 22, no. 2, pp. 173–178, 2004.

[33] J. M. Vonmoss, S. L. Tabor, V. Tripathi, and A. t. Volya *Phys. Rev. C*, vol. 92, p. 03430, 2015.

[34] Mirion Technologies: Clover Detectors. `http://www.canberra.com/products/detectors/pdf/Clover-Detector-C39840.pdf`.

[35] XIA DGF Pixie-16. `http://www.xia.com/DGF_Pixie16.html`.

[36] G. F. Knoll, *Radiation Detection and Measurement.* John Wiley and Sons, Inc., 2017.

[37] P. C. Bender, C. R. Hoffman, M. Wiedeking, and *et al. Phys. Rev. C*, vol. 80, p. 014302, 2009.

[38] M. Bouhelal, F. Haas, E. Caurier, F. Nowacki, and A. Bouldjedri *Nuclear Phys. A*, vol. 864, pp. 113–127, 2011.

[39] R. S. P. C. Lubna.

[40] N. Larson, S. N. Liddick, and *et al. Nucl. Instrum. Methods Phys. Res. Sect. A*, vol. 727, pp. 59–64, 2013.

[41] D. J. Morrissey, B. M. Sherrill, M. Steiner, A. Stolz, and I. Wiedenhoever *Nucl. Instrum. Methods Phys. Res. Sect. B*, vol. 204, pp. 90–96, 2003.

[42] S. Grévy and *et al. Phys. Lett. B*, vol. 594, no. 3-4, 2004.

BIOGRAPHICAL SKETCH

Born and raised in Colorado, Brittany's love for the stars was fueled by the dark nights, clear skies, and high altitude. After tragically learning that she would ultimately be too short to be a fighter pilot, ultimately leading to her life-long dream of becoming an Astronaut, Brittany went out searching for a new way to bring her closer to the heavens. In high school, she decided that she would continue her education in Astrophysics, eventually leading up to obtaining her PhD so that one day she would be known as Dr.[Pause] BrittanyLynnAbromeit.

Her journey to the stars brought her to Michigan State University in 2009. During her second semester of chemistry she was introduced to Dr. Sean Liddick, a physical chemist working at the National Super Conducting Cyclotron Laboratory, who would be the start of her nuclear astrophysics journey. The very next year, Brittany started heavily working with Dr. Liddick at the NSCL conducting research focused on the simulation of beta decay using two different detector systems for the Beta Counting System. She would continue to work with Dr. Liddick until graduation.

2013, Brittany graduated with her B.S in Astrophysics and continued her nuclear physics journey in warmer climates down at Florida State University. The year prior, Brittany met Dr. Samuel Tabor during a DNP meeting and decided she would like to try and join his group after starting her graduate career at FSU. The following summer after starting, Brittany was lucky enough to be able to join Sam's group where she happily spent the remaining years working on thesis projects and hearing many, many fantastic stories.

In Fall of 2018, Brittany graduated with her PhD in physics, with a specialty in nuclear physics. She will continue her nuclear adventure as a PostDoc up at Pacific Northwest National Laboratory. Although Brittany has strayed from astrophysics, her love for the heavens is still as strong as ever, but her desire to contribute to humanity has overcome her desire to reach the stars. During her time at PNNL, Brittany will use this desire to focus on non-proliferation actions and treaty monitoring, in hopes to keep the Earth that she loves safe so that the heavens above may continue to be adored.